

Method for Single-Cell Mass and Electrophoretic Mobility Measurement

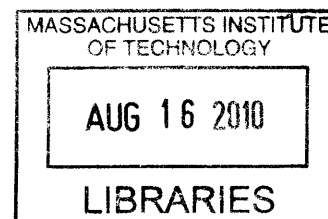
by

Philip Dextras

B.A.Sc., Engineering Physics
University of British Columbia, 2002

Submitted to the Department of Biological Engineering
in Partial Fulfillment of the Requirements for the Degree of
Doctor of Philosophy
at the
Massachusetts Institute of Technology

February 2010



ARCHIVES

© 2010 Massachusetts Institute of Technology. All rights reserved

The author hereby grants to MIT permission to reproduce and to distribute publicly paper and electronic copies of this thesis document in whole or in part in any medium now known or hereafter created.

Signature of Author
Department of Biological Engineering
December 18, 2009

Certified by
Scott R. Manalis
Associate Professor of Biological and Mechanical Engineering
Thesis Co-Supervisor

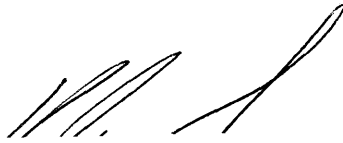
Certified by
Jongyoon Han
Associate Professor of Biological and Electrical Engineering
Thesis Co-Supervisor

Accepted by
Darrell Irvine
Co-Chair, Department Committee for Graduate Students

Report Documentation Page		Form Approved OMB No. 0704-0188
Public reporting burden for the collection of information is estimated to average 1 hour per response, including the time for reviewing instructions, searching existing data sources, gathering and maintaining the data needed, and completing and reviewing the collection of information. Send comments regarding this burden estimate or any other aspect of this collection of information, including suggestions for reducing this burden, to Washington Headquarters Services, Directorate for Information Operations and Reports, 1215 Jefferson Davis Highway, Suite 1204, Arlington VA 22202-4302. Respondents should be aware that notwithstanding any other provision of law, no person shall be subject to a penalty for failing to comply with a collection of information if it does not display a currently valid OMB control number.		
1. REPORT DATE FEB 2010	2. REPORT TYPE	3. DATES COVERED 00-00-2010 to 00-00-2010
4. TITLE AND SUBTITLE Method for Single-Cell Mass and Electrophoretic Mobility Measurement	5a. CONTRACT NUMBER	
	5b. GRANT NUMBER	
	5c. PROGRAM ELEMENT NUMBER	
6. AUTHOR(S)	5d. PROJECT NUMBER	
	5e. TASK NUMBER	
	5f. WORK UNIT NUMBER	
7. PERFORMING ORGANIZATION NAME(S) AND ADDRESS(ES) Massachusetts Institute of Technology, 77 Massachusetts Avenue, Cambridge, MA, 02139		8. PERFORMING ORGANIZATION REPORT NUMBER
9. SPONSORING/MONITORING AGENCY NAME(S) AND ADDRESS(ES)		10. SPONSOR/MONITOR'S ACRONYM(S)
		11. SPONSOR/MONITOR'S REPORT NUMBER(S)
12. DISTRIBUTION/AVAILABILITY STATEMENT Approved for public release; distribution unlimited		
13. SUPPLEMENTARY NOTES		
14. ABSTRACT Analysis of single cells using flow cytometry techniques has created a wealth of knowledge about cellular phenomena that could not be obtained by population average measurements. As these techniques are integrated with others to increase the number of parameters that can be measured on single cells and these measurements are made more quantitative, their ability to discriminate between sub-populations of cells increases. Microfabricated sensors offer unique advantages in this area because their internal geometries can be engineered at a size scale comparable to the cell's, making them naturally well-suited for single-cell measurements. The suspended microchannel resonator (SMR) is a versatile flow cytometry platform which is capable measuring the mass of single cells with femtogram resolution. The net frequency shift of a resonant cantilever as the cell transits the fluid-filled microchannel running through it is proportional to the buoyant mass of the cell. The resonance frequency of the SMR is also highly sensitive to a cell's position along the cantilever's length. This thesis presents a new method which makes use of this property to accurately quantify the electrophoretic mobility (EPM) of cells transiting the SMR while subjected to oscillatory electric fields. Recorded resonance frequency time courses can be analyzed to extract both the buoyant mass and EPM of individual cells. This instrument has been used to simultaneously measure the EPM and buoyant masses of discrete polystyrene microspheres and Escherichia coli bacteria. As it has been applied to microspheres of known density, the integrated measurement makes it possible to compute the absolute mass and surface charge of individual microspheres. It has been shown that integrated single-microsphere mass and surface charge measurement enables differentiation of complex aqueous suspensions which is not possible by either measurement alone.		
15. SUBJECT TERMS		

16. SECURITY CLASSIFICATION OF:			17. LIMITATION OF ABSTRACT Same as Report (SAR)	18. NUMBER OF PAGES 146	19a. NAME OF RESPONSIBLE PERSON
a. REPORT unclassified	b. ABSTRACT unclassified	c. THIS PAGE unclassified			

This thesis has been examined by a committee of the Biological Engineering Department as follows:



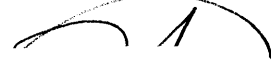
Professor Klavs F. Jenison

Department Head, Warren K. Lewis Professor of Chemical Engineering,
Professor of Materials Science and Engineering
Thesis Committee Chairman



Professor Scott R. Manalis

Associate Professor of Biological and Mechanical Engineering
Thesis Co-Supervisor



Professor Jongyoon Han

Associate Professor of Biological and Electrical Engineering
Thesis Co-Supervisor

Method for Single-Cell Mass and Electrophoretic Mobility Measurement

by

Philip Dextras

Submitted to the Department of Biological Engineering
on December 21, 2009 in Partial Fulfillment of the
Requirements for the Degree of
Doctor of Philosophy

Abstract

Analysis of single cells using flow cytometry techniques has created a wealth of knowledge about cellular phenomena that could not be obtained by population average measurements. As these techniques are integrated with others to increase the number of parameters that can be measured on single cells and these measurements are made more quantitative, their ability to discriminate between sub-populations of cells increases. Microfabricated sensors offer unique advantages in this area because their internal geometries can be engineered at a size scale comparable to the cell's, making them naturally well-suited for single-cell measurements.

The suspended microchannel resonator (SMR) is a versatile flow cytometry platform which is capable measuring the mass of single cells with femtogram resolution. The net frequency shift of a resonant cantilever as the cell transits the fluid-filled microchannel running through it is proportional to the buoyant mass of the cell. The resonance frequency of the SMR is also highly sensitive to a cell's position along the cantilever's length. This thesis presents a new method which makes use of this property to accurately quantify the electrophoretic mobility (EPM) of cells transiting the SMR while subjected to oscillatory electric fields. Recorded resonance frequency time courses can be analyzed to extract both the buoyant mass and EPM of individual cells.

This instrument has been used to simultaneously measure the EPM and buoyant masses of discrete polystyrene microspheres and *Escherichia coli* bacteria. As it has been applied to microspheres of known density, the integrated measurement makes it possible to compute the absolute mass and surface charge of individual microspheres. It has been shown that integrated single-microsphere mass and surface charge measurement enables differentiation of complex aqueous suspensions which is not possible by either measurement alone.

Thesis Co-Supervisor: Scott R. Manalis

Title: Associate Professor of Biological and Mechanical Engineering

Thesis Co-Supervisor: Jongyoon Han

Title: Associate Professor of Biological and Electrical Engineering

Acknowledgements

During the course of my studies, I have received support from many colleagues, friends and family. I am extremely fortunate to have been surrounded by such excellent people during this time, and without their contributions, this thesis would not have been possible.

Above all, I would like to thank my primary advisor, Scott Manalis, for giving me the opportunity to work in his research group. Because of this, I was able to access a diverse set of resources which are highly unique to his group and opened up many interesting possibilities for my research. Scott has also been a great source of advice and encouragement over the years, both of which have been instrumental in my scientific and professional development.

I am very thankful for the guidance provided by my second advisor, Jay Han. Our interactions were highly educational for me, especially in the areas of nanofabrication and electrokinetic transport. I would also like to thank the chair of my thesis committee, Klavs Jensen, for his insightful contributions to our meetings.

I have learned a great deal from working together with many members of both the Manalis and Han research groups. Thomas Burg and Michel Godin were both invaluable for their knowledge and experience with experimental techniques related to the SMR. Ying-Chih Wang and Vincent Liu helped me to learn experimental techniques related to nanofluidic preconcentration. I was very fortunate to have the opportunity to collaborate with Francisco Delgado on the bacterial studies. I thank Scott Knudsen for answering my questions about anything related to biochemistry, microbiology and molecular biology techniques. Kris Payer from the Manalis group and Wenjiang Shen from Innovative Micro Technology contributed their vast experience in microfabrication to the process development.

I also owe a great deal to Vicky Diadiuk and the staff of the MIT Microsystems Technology Laboratories for introducing me to the field of MEMS process engineering and for my practical training in this field. Eric Lim, Bob Bicchieri, Paul Tierney, Dave Terry, and Bernard Alamariu were especially helpful in this respect.

I am grateful to Professor Robert Langer and Professor Sangeeta Bhatia for providing me with access to instruments in their laboratories, and to Omar Fisher from the Langer research group for his assistance. Mark Belanger from the Edgerton Machine Shop was a great source of advice related to machining of the many custom components that were needed to conduct the research described in this thesis.

This work has been funded by the National Cancer Institute Platform Partnership Grant (R01-CA119402) and the Institute for Collaborative Biotechnologies from the U.S. Army Research Office.

Most importantly, I would like to thank my family, especially my parents Susan and Ken and my sister Jenn for their love and support over the years. I am deeply grateful to my fiancée Miwako for her constant care and affection. I would also like to thank Miwa's parents Hiromasa-san and Mikiko-san, and her brother Shinichiro for their kindness and generosity.

Table of Contents

1. Introduction.....	8
1.1 Physical Characterization of Colloids.....	8
1.2 Cell Electrophoresis	9
1.3 Single-Particle Mass and EPM Measurement Using the SMR.....	13
2. Theory of Operation.....	16
2.1 SMR Resonant Frequency Sensitivity to Point Mass Loading	16
2.2 Particle Motion in the SMR	19
2.3 Measurement of Electrophoretic Mobility and Surface Charge.....	23
3. Instrument Design.....	28
3.1 Electrophoresis Integration	28
3.2 Channel Wall Zeta Potential Measurement.....	31
3.3 Integrated Particle Measurement.....	34
3.4 Signal Processing	35
4. Instrument Characterization.....	42
4.1 Passivation Oxide Breakdown	42
4.2 Electric Field Measurement	46
4.3 Device Actuation.....	47
4.4 Computational Error Analysis.....	49
4.5 Coupling.....	53
4.5.1 OSMR	53
4.5.2 OLSMR.....	58
4.6 Differentiation of Polystyrene Microspheres by Mass and Surface Charge	59

4.6.1 Material Preparation.....	59
4.6.2 Microsphere Mass and Charge Measurement.....	60
4.6.3 Signal to Noise Ratio and Throughput.....	63
5. Characterization of Bacteria by Buoyant Mass and Electrophoretic Mobility	65
5.1 Introduction	65
5.2 Materials and Methods	70
5.2.1 Integrated Buoyant Mass and EPM	70
5.2.2 Standalone Buoyant Mass and Volume	72
5.2.3 Membrane Permeability.....	73
5.2.4 Bactericidal Activity	75
5.3 Results and Discussion.....	75
5.3.1 Integrated Buoyant Mass and EPM	75
5.3.2 Standalone Buoyant Mass and Volume	79
5.3.3 Membrane Permeability and Bactericidal Activity.....	82
5.3.4 Discussion	83
6. Integrated Preconcentration and Sensing of Protein Biomarkers	85
6.1 Introduction	85
6.1.1 Nanofluidic Concentrator.....	87
6.1.2 Integrated Device Concept.....	90
6.1.3 Theory of Operation.....	94
6.2 Device Design	99
6.2.1 First Generation	100
6.2.2 Second Generation	102
6.2.3 Third Generation.....	105
6.2.4 Fourth Generation	110
6.3 Device Characterization	112
6.3.1 Type 1 Integrated Device.....	112
6.3.2 Type 2 Integrated Device.....	114
A.1: Fabrication Processes.....	121
A.1.1 OSMR Process	121
A.1.2 First Generation Integrated Device	123
A.1.4 Third Generation Integrated Device	129
A.1.5 Fourth Generation Integrated Device.....	132
A.2 Circuit Schematics	135
A.3 Fluidic Manifold Drawings.....	136
Bibliography	138

Chapter 1

Introduction

1.1 Physical Characterization of Colloids

Colloidal dispersions have a broad range of technological applications, including paints, pharmaceuticals, foods, photographic emulsions, ceramics, drilling muds, inks, and photonic crystals. [1-5] Many of these applications require very precise control over colloidal stability and hence inter-particle interactions which are dependent on the physico-chemical properties of the particles themselves. Quantitative measures of particle properties such as the size, mass and surface charge are therefore often of value in designing systems and manufacturing processes for these applications. Measurements of particle size and surface charge are routinely performed using light scattering techniques such as phase analysis light scattering (PALS). [6] This technique estimates the size and electrophoretic mobility (EPM) of particles by measuring Doppler shift of laser light scattered by the particles due to their average Brownian motion and their motion in an applied electric field, respectively. While applicable to a wide variety of colloidal systems, PALS reports size and EPM values which represent averages over

multiple particles. Hence accuracy in estimating the particle's charge, which is dependent on both the size and the EPM, can suffer from errors made in ensemble average measurements of these two parameters, both of which may be multi-modal for a complex population. Various approaches for measuring size and electrical properties of single particles have been explored, such as the Coulter principle and mass spectrometry. Carbon nanotube-based Coulter counters are able to measure discrete-particle EPM and size, but compromises must be made between the signal-to-noise ratio (SNR) of the EPM measurement and that of the size measurement since they have inherently different optimum orifice lengths. [7] Measurement of particle charge-to-mass ratio by time-of-flight mass spectrometry has been integrated with direct charge measurement using a Faraday disc, but because the sample must be dried, the measured charge may not accurately reflect that experienced in the desired dispersion medium for a given application. [8]

1.2 Cell Electrophoresis

A wide variety of interactions between the cell and its environment are determined by the physical and chemical properties of the outer membrane. The importance of these interactions in determining cell behavior is indicated by the finding that approximately a third of yeast genes encode a membrane protein, and that this fraction is even higher for multi-cellular organisms. The fact that many of the forces that govern these interactions are fundamentally electrical in nature has motivated the development of cell

electrophoresis [9-11] as a means of quantitatively characterizing the cell membrane on the basis of its EPM in parallel with traditional biochemical analyses. [12, 13] Cell functions which are influenced by surface charge include ion transport, [14] cell-macromolecule interactions, [15] cell-cell interactions, [16, 17] shape, and motility. [18] As a result, cellular EPM has provided a means of experimentally testing theories which describe some of the fundamental behaviors of cells. For example, cellular EPM measurement has played a role in elucidating the relationship between microbial surface charge and adhesion, [19, 20] which has many important implications for human health [21-23], the environment, [24-26] and a variety of industries. [27-29] In multi-cellular organisms, EPM has been shown to vary between different cell types [30-37] and physiological states of the cell, [38-40] making cellular EPM measurement a useful tool for fractionation, isolation, and characterization of subsets of mammalian cell populations. As they are applied to more mammalian cell systems, these techniques could eventually find important applications as non-invasive tools in the development of new cell-based technologies such as gene therapy, immunotherapy and regenerative medicine. [41, 42]

Instrumentation for quantitative cellular EPM measurement *in vitro* generally consists of an electrically insulating chamber filled with a cell suspension across which an electric potential is applied. Observation of the velocity of cell migration due to an electric field of known magnitude makes it possible to compute the EPM of the observed cells. Quantitative measurement of cellular EPM can be accomplished by light scattering, image transduction, or by direct microscopic imaging. Light scattering measurements such as PALS suffer from the inherent limitation that the reported EPM is an average

over multiple cells, which obscures the dispersity in EPM that is observed when measurements are made at the single-cell level. [43] When EPM is averaged over many cells, the reported variance of the measurement is often computed using repeated population average measurements, which results in deceptively small variances. In contrast, single-cell EPM measurements have been shown to produce distributions which are multi-modal and have significantly larger variances. Outliers in the population are ignored by averaging, which inhibits the application of EPM measurement techniques such as PALS to systems where rare cells are of importance. Image transduction and direct imaging are both methods which are capable of single cell measurements. In image transduction, the transmitted light from a particle's image projected onto a rotating grating is compared to a reference light source transmitted through the same grating. [44] If a particle moves in the same direction as the grating, it crosses fewer line pairs per unit time, so that the transmitted light from the particle will fluctuate at a lower frequency than the transmitted light from the reference source. Although this technique was not originally designed for single-particle measurements, it has more recently been modified for this purpose. [45] Perhaps the most widely practiced method for single-cell EPM measurement is direct microscopic observation of the electrophoretic drift velocity [46], which can be automated using image analysis algorithms to track the velocity of individual cells. [47, 48] With both of these single-cell measurement techniques, the need for bulky and expensive imaging equipment is an obstacle which must be overcome in order for them to be widely adopted in research settings and adapted to clinical applications.

As it is integrated with other quantitative cytometry techniques, the measurement of cellular EPM can further expand our ability to differentiate physiologically meaningful cell subpopulations. Certain cell phenotypes which are degenerate in EPM may not be in another parameter; therefore, multi-parameter measurements can potentially increase the number of resolvable species. One way to carry out multi-parameter measurements on the same cell population is to prefractionate the population based on one parameter before measuring the second parameter in each of the fractions. However, serial prefractionation using established methods such as fluorescence-activated cell-sorting requires samples to be transferred between instruments, which makes it possible for cells to change states during transfer or for the number of viable cells in some states to become insufficient for EPM measurement. For these reasons, simultaneous multi-parameter measurements are preferred over serial ones in general; however, in some cases, a hybrid approach can be highly effective. For example, simultaneous measurements of cellular EPM and sedimentation velocity (SV) have been carried out on single mouse lymphoma cells, and the two parameters were found to correlate. [49] In parallel with these measurements, different sedimentation column fractions of the same tissue sample showed differences in DNA content, clonogenic capacity, survival after x-ray irradiation, and sensitivity to natural killer cells, which allowed some fractions to be qualitatively associated with phenotypes. The phenotypic differences between fractions could then be compared to the integrated two-parameter measurements to infer correlations between EPM and phenotype. Because the correlation between EPM and SV was much more subtle than the one between SV and phenotype in this study, it exemplifies how an integrated two-parameter measurement has been able to elucidate relationships between

EPM and phenotype that could have been missed if carried out strictly using serial prefractionation.

1.3 Single-Particle Mass and EPM Measurement Using the SMR

It has been shown recently that the mass of single particles can be measured with high precision using a suspended microchannel resonator (SMR). [50] With this method, particle mass is measured as the change in resonance frequency of a hollow cantilever as a suspended particle transits the fluid-filled microchannel running through it (Fig. 1-1A). The net frequency shift is proportional to the buoyant mass of the particle. In addition, as the particle travels through the cantilever, the resonance frequency of the SMR is highly sensitive to its position along the cantilever's length. This property can be used to accurately quantify the EPM of particles traveling through the SMR while being subjected to oscillatory electric fields (Fig. 1-1B). Recorded resonance frequency time courses that correspond to particles traveling through the SMR while undergoing oscillatory electrophoresis can be analyzed to extract both the particle's buoyant mass and EPM. When applied to rigid microspheres, measurement of these two parameters, combined with the microsphere's density, determines the absolute mass and surface charge of individual microspheres. This thesis demonstrates that the application of the technique to single-particle mass and surface charge measurement of polystyrene microspheres enables differentiation of complex particle mixtures which is not possible

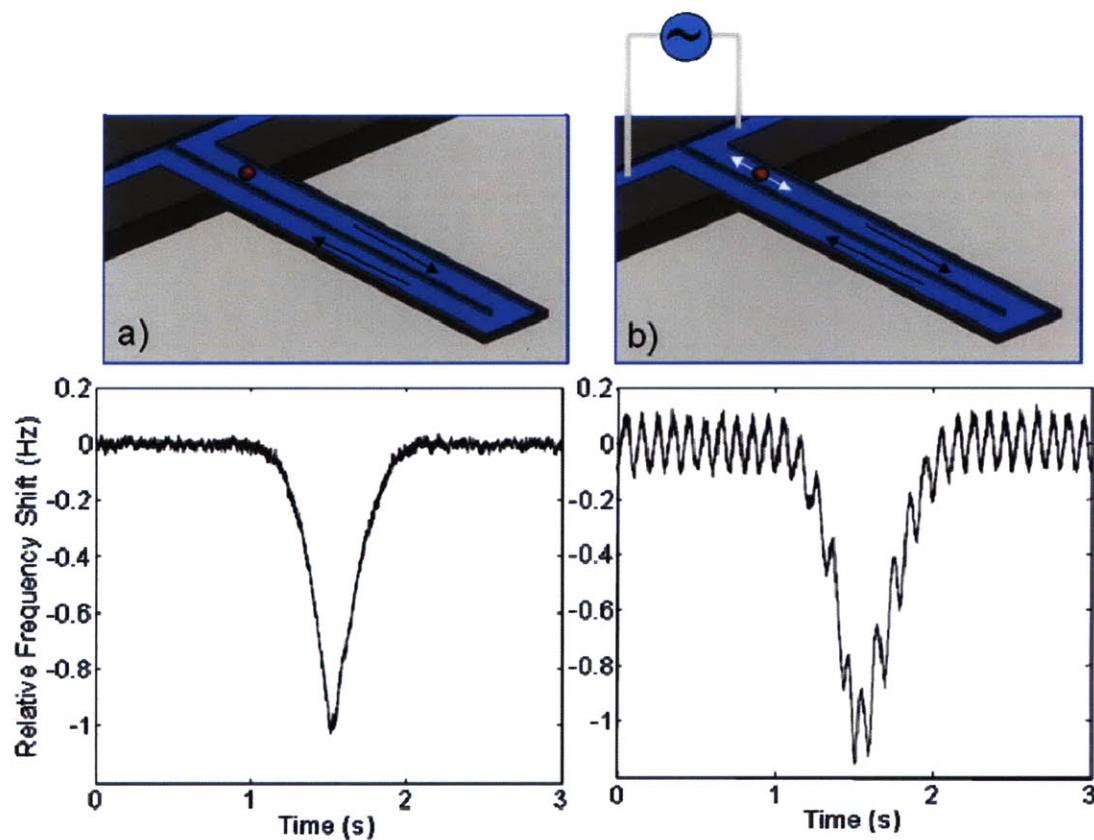


Figure 1-1: (a) A cut-away view of the fluid-filled suspended microchannel through which particles travel (top). This channel is a tunnel through the inside of the resonant cantilever structure. A transient resonance frequency time course is shown (bottom) for a 2.2 μ m polystyrene particle which drifts through the sensor under a small pressure gradient. The height of the peak is proportional to the particle's buoyant mass. (b) If an oscillating electric field is applied longitudinally to the channel, particles will oscillate at the same frequency due to a combination of electrophoresis and electro-osmotic flow. Spectral analysis of the resulting resonance frequency time course can be performed to extract the particle's electrophoretic mobility.

by either measurement alone (Section 4.6). In addition, the technique has been applied to single-cell buoyant mass and EPM measurement of *Escherichia coli* bacteria (Chapter 5). This technique offers several advantages over existing cellular EPM measurement techniques. The integration of EPM measurement with the measurement of cell mass allows individual cells to be clustered in two dimensions which are not simultaneously observable using conventional flow cytometers, potentially allowing more effective discrimination between subpopulations within complex cell suspensions. This feature

creates unique new opportunities to explore the mechanisms underlying the action of antimicrobial peptides on the outer membranes of bacterial cells, as discussed in Section 5.1. Furthermore, the instrument is based on a microdevice which exhibits scaling properties appropriate for measuring a wide range of cell sizes and can be inexpensively mass-produced using batch fabrication processes. The instrument as a whole is amenable to miniaturization for point-of-care applications.

Chapter 2

Theory of Operation

2.1 SMR Resonant Frequency Sensitivity to Point Mass Loading

The Euler-Bernoulli theory of beam bending is accurate for long, thin beams with small total displacements. Presently, we consider flexural vibrations in such a beam with an areal bending moment given by

$$I_y = \int_A y^2 dA \quad \text{Eq. 2.1a}$$

which is constant along the length of the beam (Fig. 2-1). Taking into account only the transverse linear acceleration of the beam and ignoring rotational inertia and shearing effects, the Euler-Bernoulli beam equation is

$$EI_y \frac{\partial^4 W}{\partial x^4} = -\rho A \frac{\partial^2 W}{\partial t^2} \quad \text{Eq. 2.1b}$$

where $W(x,t)$ is the transverse displacement of the vibrating beam along its length, E is the Young's modulus, ρ is the mass density, and A is the cross-sectional area.

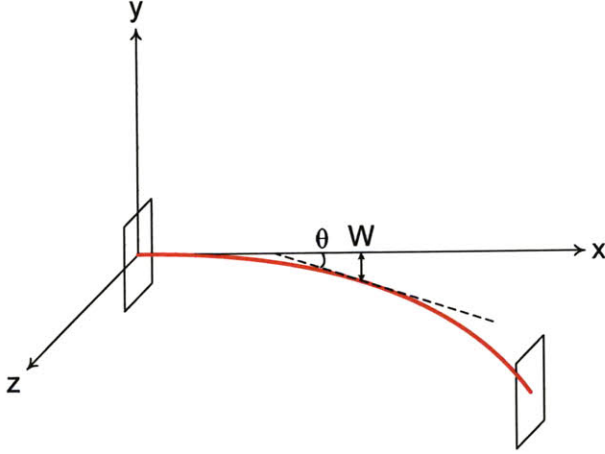


Figure 2-1: Spatial co-ordinates for a prismatic beam undergoing flexural vibrations. The neutral axis is shown in red and the tangent to the neutral axis is indicated by a dashed line. The transverse displacement of the neutral axis is denoted by W . The angle between the local tangent to the neutral axis and the undisplaced beam axis is denoted by θ .

If we assume a harmonic dependence for the displacement,

$$W_n(x,t) = a_n U_n(x) \sin(\omega_n t) \quad \text{Eq. 2.2a}$$

where a_n , $U_n(x)$ and ω_n are the peak amplitude, mode shape, and resonant frequency of the n^{th} mode respectively, then for a clamped-free beam (cantilever), the resonant frequency and the mode shape are given by

$$\omega_n = \lambda_n^2 \sqrt{\frac{EI_y}{\rho AL^4}} \quad \text{Eq. 2.2b}$$

$$U_n(x) = \frac{1}{2} \left[\cos\left(\frac{\lambda_n x}{L}\right) - \cosh\left(\frac{\lambda_n x}{L}\right) - \left(\frac{\cos(\lambda_n) + \cosh(\lambda_n)}{\sin(\lambda_n) + \sinh(\lambda_n)} \right) \left(\sin\left(\frac{\lambda_n x}{L}\right) - \sinh\left(\frac{\lambda_n x}{L}\right) \right) \right] \quad \text{Eq. 2.2c}$$

where λ_n is the eigenvalue for the n^{th} mode satisfying $\cos(\lambda_n) \cosh(\lambda_n) = -1$. [51] In all experiments discussed here, modes other than the fundamental mode are suppressed, so

we expect to observe motion as described by Equations 2.2 with $\lambda = \lambda_1 = 1.875$. The amplitude of the vibration, a_1 , is determined by the initial condition.

If the cantilever is now loaded by a point mass Δm positioned at $x = x_m$, its resonant frequency is shifted as a result. [52] If the point mass is much less than the cantilever's unloaded mass, m_0 , then the change in mode shape due to point mass loading will be negligible, and the resonance frequency can be estimated using the Rayleigh-Ritz theorem, which states that the time averaged strain energy of the cantilever is equal to the total kinetic energy at resonance:

$$E_{strain} = E_k + E_{k,\Delta m} \quad \text{Eq. 2.3}$$

Assuming the mode shapes are normalized so that $\int_0^L \tilde{U}^2(x) dx = L$, where L is the cantilever's length, then the kinetic energy of the cantilever is given by

$$\begin{aligned} E_k &= \int_V \frac{1}{2} \rho \omega_{\Delta m}^2 a^2 \tilde{U}^2(x) dV \\ &= \frac{1}{2} m_0 \omega_{\Delta m}^2 a^2 \end{aligned} \quad \text{Eq. 2.4}$$

and the kinetic energy of the point mass is given by

$$E_{k,\Delta m} = \frac{1}{2} \Delta m \omega_{\Delta m}^2 a^2 \tilde{U}^2(x_m) \quad \text{Eq. 2.5}$$

The strain energy of the loaded cantilever is approximately equal to the kinetic energy of the unloaded cantilever since the mode shape is not affected by point mass loading:

$$E_{strain} \approx \frac{1}{2} m_0 \omega_0^2 a^2 \quad \text{Eq. 2.6}$$

From Equations 2.3-2.6, the shift in resonant frequency relative to the unloaded state as a function of the point mass position is given by

$$\frac{\Delta\omega(x_m)}{\omega_0} = \frac{\omega_{\Delta m}(x_m) - \omega_0}{\omega_0} = -1 + \left[1 + \frac{\Delta m}{m_0} \tilde{U}^2(x_m) \right]^{-1/2} \quad \text{Eq. 2.7}$$

2.2 Particle Motion in the SMR

When no electric field is present in the fluid-filled suspended microchannel, the motion of particles transiting the channel is governed by the Stokes drag of the fluid and the centripetal force due to flexural vibrations of the cantilever. To estimate the centripetal force, we consider a particle at a distance $x = x_m$ from the clamped end of the cantilever, measured along the neutral axis (Fig. 2-1). The bending angle, θ , is defined as the angle that the local tangent to the displaced neutral axis makes with the original beam axis. We can approximate the bending angle as

$$\begin{aligned} \theta(x_m) &\cong \tan(\theta(x_m)) = \left. \frac{\partial W}{\partial x} \right|_{x=x_m} \\ &\cong a_1 \sin(\omega_1 t) \left. \frac{dU_1}{dx} \right|_{x=x_m} \end{aligned}$$

where the mode shape is described by Equation 2.2c, and we can estimate the centripetal acceleration as:

$$a_f(x_m) = x_m \dot{\theta}_{rms}^2 \cong \frac{x_m}{2} \left(\omega_1 a_1 \left. \frac{dU_1}{dx} \right|_{x=x_m} \right)^2 \quad \text{Eq. 2.8}$$

The equation of motion for the particle's longitudinal position, $x(t)$, is

$$m_p(\ddot{x} - a_f) = -(m_p - m_f)a_f - 6\pi\eta R(\dot{x} - v_f) - \frac{1}{2}m_f(\ddot{x} - a_f)$$

where m_p and m_f are the masses of the particle and the fluid displaced by the particle, respectively, v_f is the velocity of the fluid, η is the fluid viscosity and R is the particle's radius. The three force terms on the right-hand side are due to, respectively, the centripetal acceleration of the fluid, the quasi-steady Stokes drag, and the added mass. To compute the particle's position as a function of time in the suspended microchannel, we break the transit into two parts, the first being the portion where the particle is traveling from the base of the cantilever to the tip (forward segment), and the second being the portion where the particle returns from the tip to the base (return segment). Since the particle only spends a brief time turning the corner at the end of the cantilever, motion during this portion of the transit is ignored. During the forward segment of the transit, the particle's position relative to the starting point, x , is equivalent to x_m , so we can exchange these two quantities in Equation 2.8. The equation of motion for the forward segment then becomes

$$\left(m_p + \frac{1}{2}m_f\right)\ddot{x} + 6\pi\eta R\dot{x} - \frac{3}{4}m_f\left(\omega_1 a_1 \frac{dU_1}{dx}\bigg|_{x=x_m}\right)^2 x = 6\pi\eta R v_f \quad \text{Eq. 2.9a}$$

subject to the initial conditions $x(0) = 0$ and $\dot{x}(0) = v_f$. During the reverse segment, the particle's position relative to the new starting point is defined as $x = L - x_m$, and the centripetal force is now in the negative x -direction. The equation of motion for the reverse segment is then

$$\left(m_p + \frac{1}{2} m_f \right) \ddot{x} + 6\pi\eta R \dot{x} + \frac{3}{4} m_f \left(\omega_1 a_1 \frac{dU_1}{dx} \bigg|_{x=x_m} \right)^2 (L - x) = 6\pi\eta R v_f \quad \text{Eq. 2.9b}$$

where $x(0) = 0$ as before, but now the initial condition for \dot{x} is determined by the final condition from the forward segment's solution.

The validity of this model was established by passing polystyrene microspheres with a nominal diameter of $8.6\mu\text{m}$ through a cantilever with a $15\mu\text{m} \times 20\mu\text{m} \times 322\mu\text{m}$ suspended microchannel and measuring the resulting resonance frequency time courses. The model, consisting of Equations 2.7 and 2.9, was fit to the data from 37 such transits by iteratively adjusting the particle diameter, fluid velocity and tip amplitude for each transit to determine the mode shape which best fit the data. A typical fit, along with histograms of the fitting parameters, is shown in Figure 2-2. An important feature of these results is that in spite of the fairly large range of extracted fluid velocities, the extracted tip amplitudes form a much narrower distribution, which is expected for the present experimental conditions. The well-defined tip amplitude of $148 \pm 22\text{ nm}$ from this simulation is also a useful starting point in making predictions for the motion of smaller particles such as bacteria in smaller cantilevers, which is the focus of this thesis.

The model was used to determine the theoretical transit times of $2.2\mu\text{m}$ diameter polystyrene microspheres through a cantilever with a $3\mu\text{m} \times 8\mu\text{m} \times 200\mu\text{m}$ suspended microchannel. These device dimensions are representative of the ones employed in all of the experiments presented here involving measurement of EPM. This simulation involved repeatedly solving Equations 2.9 for a fixed particle radius and different

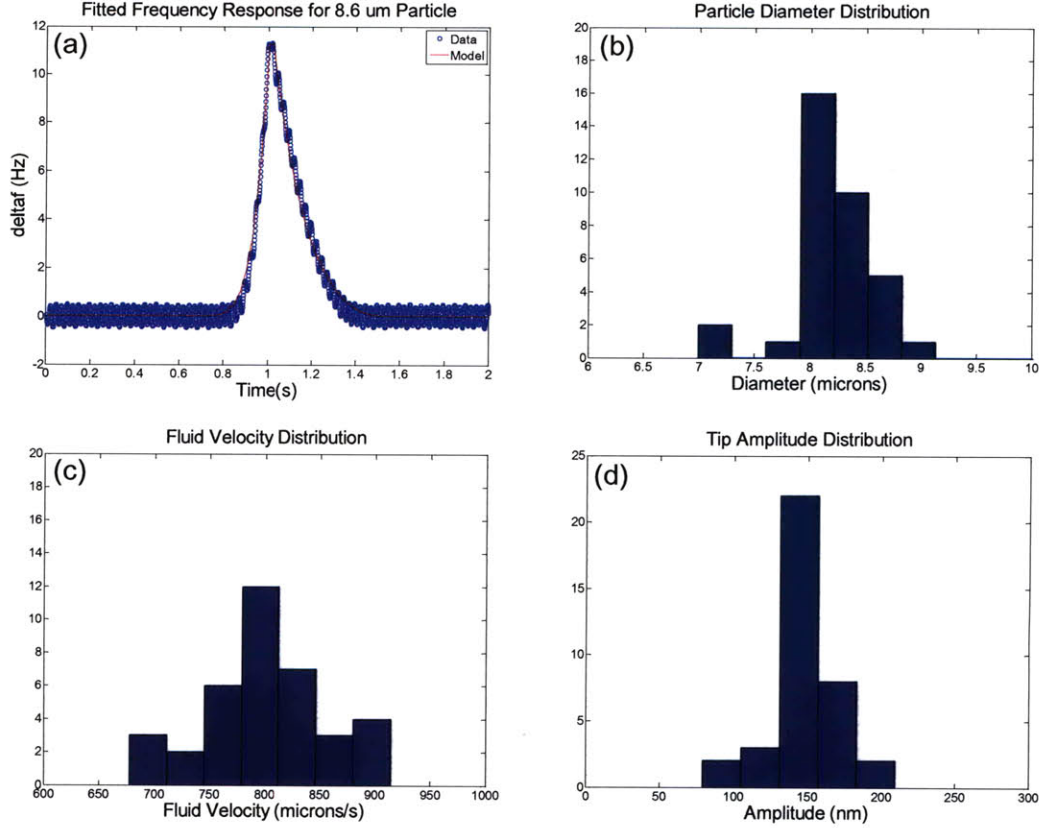


Figure 2-2: Multi-parameter fit of a model consisting of Equations 7 and 9 to experimental data from passing polystyrene microspheres with a nominal diameter of 8.6 μm through a through a cantilever with a 15 μm x 20 μm x 322 μm suspended microchannel. (a) A typical resonance frequency time course with the model superposed. (b)-(d) Best-fit parameters extracted from the fit for 37 particle transits.

combinations of the tip amplitude and fluid velocity. In Figure 2-3, the particle transit time is normalized by the transit time of the fluid and plotted against the entire set of flow rates and amplitudes simulated. As described in Chapter 3, successful measurement of particle or bacterial EPM in this system typically requires flow rates ranging from 400 to 800 $\mu\text{m/s}$. The simulation suggests that at the slowest flow rate employed, tip amplitudes approaching 500 nm will be needed before inertial effects become significant. Since this is over three times the extracted tip amplitude for the larger cantilever, the analyses

which follow will ignore the inertia of the particle and assume that all particles travel at the velocity of the fluid.

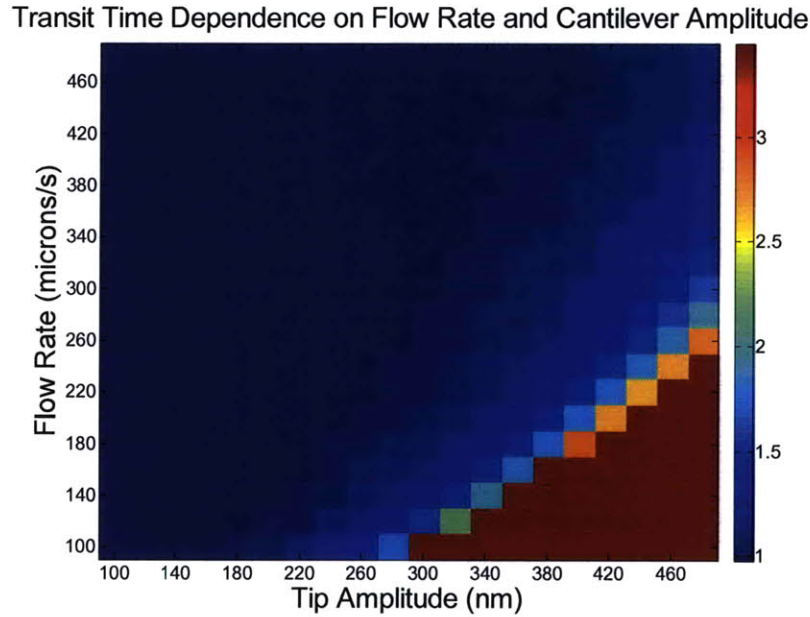


Figure 2-3 Simulated particle transit time normalized to the fluid transit time for 2.2 μm diameter polystyrene microspheres transiting a cantilever with a 3 μm x 8 μm x 200 μm suspended microchannel.

2.3 Measurement of Electrophoretic Mobility and Surface Charge

The electrophoretic mobility, μ_{EP} , is defined as the ratio of a particle's electrophoretic migration velocity to the electric field strength. The presence of an electric field in the suspended microchannel also causes electro-osmotic flow in the channel, and this flow has a similarly-defined mobility.

$$\mu_{EP} = \frac{v_{EP}}{E} \quad \text{Eq. 2.10a}$$

$$\mu_{EOF} = \frac{v_{EOF}}{E} \quad \text{Eq. 2.10b}$$

Because all particles under consideration and the silicon dioxide channel surfaces are negatively charged under the chosen buffer conditions, the electrophoretic and electro-osmotic forces on a particle oppose each other. Particles that are subjected to a sinusoidal electric field, $E = E_0 \sin(\omega t)$, will oscillate with a spatial amplitude that is proportional to the sum of their mobilities:

$$A = (\mu_{EP} + \mu_{EOF}) \frac{E_0}{\omega} \quad \text{Eq. 2.11}$$

where the sign of the spatial amplitude, A , indicates whether the motion is aligned with the field (positive sign) or opposed to it (negative sign). If the electro-osmotic mobility of the channel and the electric field strength are known, then one can determine the particle's mobility from Equation 2.11 by measuring the spatial amplitude.

The electro-osmotic mobility of the suspended microchannel and the electrophoretic mobilities of rigid particles such as polymer microspheres are well-described using the Helmholtz-Smoluchowski formula, because of their large sizes relative to the double layer thickness, which is estimated to be 2.6 nm for the buffer conditions of all experiments presented here. In this approximation, the microsphere mobility and electro-osmotic mobility are given by

$$\mu_{EP} = \frac{\varepsilon \zeta_p}{\eta} \quad \text{Eq. 2.12a}$$

$$\mu_{EOF} = -\frac{\varepsilon \zeta_w}{\eta} \quad \text{Eq. 2.12b}$$

where ε is the permittivity of the buffer, η the buffer viscosity, ζ_p the zeta potential of the microsphere, and ζ_w the zeta potential of the channel wall. [53] From the microsphere's measured zeta potential and volume, the surface charge can be estimated using the Loeb formula for a monovalent binary ionic solution:

$$Q = \pi \varepsilon \kappa d^2 \frac{kT}{e_0} \left(2 \sinh \left(\frac{e_0 \zeta_p}{2kT} \right) + \frac{8}{\kappa d} \tanh \left(\frac{e_0 \zeta_p}{4kT} \right) \right) \quad \text{Eq. 2.13}$$

where d is the particle's diameter, κ the Debye-Hückel parameter, e_0 the electron charge, kT the thermal energy, and ζ_p the zeta potential of the microsphere. [54]

To determine the spatial amplitude, A , which is described in Equation 2.11, we model the resonance frequency of the SMR, $f(t)$, in response to an oscillating particle that drifts through the channel at a constant velocity v_d , as determined by the pressure gradient. Thus, the longitudinal position of the particle along the channel, x , is given by

$$x = v_d t + A \sin(\omega t)$$

As the particle passes through the channel, the induced frequency shift is described by a nonlinear function, $f(x)$, which is zero at the base and has a maximum at the apex. Although this function could be determined using the fitting algorithm described in Section 2.2, we can avoid the errors inherent in a multi-parameter fit by instead estimating the rate of change of the resonance frequency, which is given by

$$\frac{df}{dt} = \frac{df}{dx} \frac{dx}{dt} \quad \text{Eq. 2.14}$$

The first term in this chain-rule expansion corresponds to the local sensitivity of the resonance frequency to changes in particle position, whereas the second term represents the instantaneous particle velocity. Because the spatial amplitude, which is typically on the order of 10 μm , is small, compared to the cantilever length of 200 μm , we can approximate the first term by the value it would have in the absence of oscillation. Practically, this approximation is made by band-stop filtering the frequency time course data, $\tilde{f}(t)$, at the oscillation frequency. Because the position of the particle is not known, we estimate the spatial derivative by dividing the time derivative by the drift velocity:

$$\frac{df}{dx} \approx \frac{1}{v_d} \frac{d}{dt} F_{BS}[\tilde{f}]$$

The drift velocity is approximated by the baseline width of the peak in the band-stop filtered frequency signal, and the height of the peak is used to compute the particle's buoyant mass. The calibration of the device, in terms of the proportionality between resonance frequency and added mass, has been reported elsewhere. [55] The second term in the expansion, the particle's instantaneous velocity, is given by

$$\frac{dx}{dt} = v_d + \omega A \cos(\omega t)$$

Substituting these expressions into Equation 2.14 yields

$$\frac{df}{dt} \approx \left(1 + \frac{\omega A}{v_d} \cos(\omega t) \right) \frac{d}{dt} \left(F_{BS}[\tilde{f}] \right)$$

A band-pass filter centered at the oscillation frequency is applied to both sides of this approximation, eliminating the low frequency first term on the right-hand side. The order of differentiation and filtering on the left-hand side can be reversed because both operations are linear and time-invariant, which facilitates evaluation of the numerical derivative. Rearranging this relationship in terms of the spatial amplitude, yields the following expression:

$$A = \frac{\left(\frac{v_d}{\omega}\right) \frac{d}{dt} F_{BP}[\tilde{f}]}{F_{BP}\left[\cos(\omega t) \frac{d}{dt} (F_{BS}[\tilde{f}])\right]} \quad \text{Eq. 2.15}$$

These operations provide a practical means by which to estimate the spatial amplitude of oscillation, $A(t)$, from the raw resonance frequency data, $\tilde{f}(t)$.

Chapter 3

Instrument Design

3.1 Electrophoresis Integration

In order to integrate electrophoretic mobility measurement capabilities into the SMR, modifications were needed both at the device level and the system level. At the device level (Fig. 3-1), the silicon channel walls were electrically passivated with a thermal oxide layer in order to support electric fields in the fluid for electrophoresis. This was

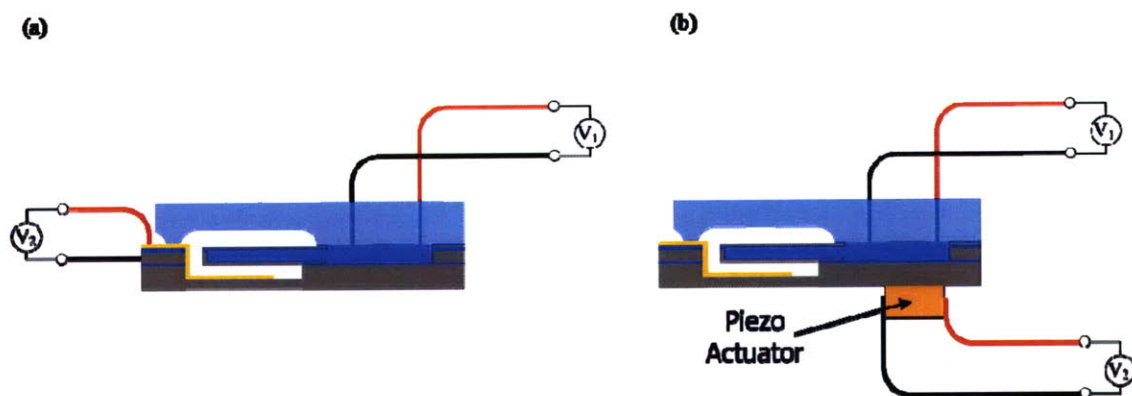


Figure 3-1: Actuation of the SMR (a) electrostatically using a patterned metal electrode, and (b) mechanically using an external piezoelectric crystal. The voltage V_1 represents the time-varying electrophoretic potential and the voltage V_2 the time-varying actuation potential.

accomplished by growing 800Å of thermal oxide on all silicon surfaces contacting the fluid. Dry thermal oxide was grown at 850 °C for 15 minutes, followed by a 42 minute wet oxidation and a 30 minute dry oxidation at the same temperature. For a description of the full fabrication process for the device, see Appendix A.1.1. This passivation oxide can break down, however, if the cantilever is driven into resonance using the electrostatic approach that has been used previously. [50] Because the cantilever contains a microchannel, using the cantilever as an electrode in the drive circuit creates a large ground plane behind the walls of this microchannel which is separated from the fluid by only the passivation oxide thickness. The need for large potential differences in the fluid to drive electrophoresis then results in large voltages being developed directly across the oxide which cause breakdown of the oxide, as observed by electrolysis of the fluid. This situation, described in greater detail in Section 4.1, is avoided if the bulk silicon is allowed to float its potential to match the local fluid voltage. Therefore in the present work, actuation was performed by means of a piezoelectric crystal external to the device. Because the piezoelectric drive transducer employed here for actuating the SMR (PL022, Physik Instrumente GmbH & Co. KG, Karlsruhe/Palmbach, Germany) has a much higher capacitance than the micro-patterned drive electrode used in the electrostatic scheme, a power amplifier stage was added to the feedback loop (Fig. 3-2). A limiter truncates the optical lever output signal for input to an Apex PA-94 amplifier (Cirrus Logic Inc., Austin, TX), the output of which is voltage divided between a current-limiting potentiometer and the piezoelectric crystal load. This circuit allows the highly capacitive load to be driven with sufficient current to actuate the device at the resonance frequency of 183 kHz with minimal distortion of the phase. For detailed schematics of the

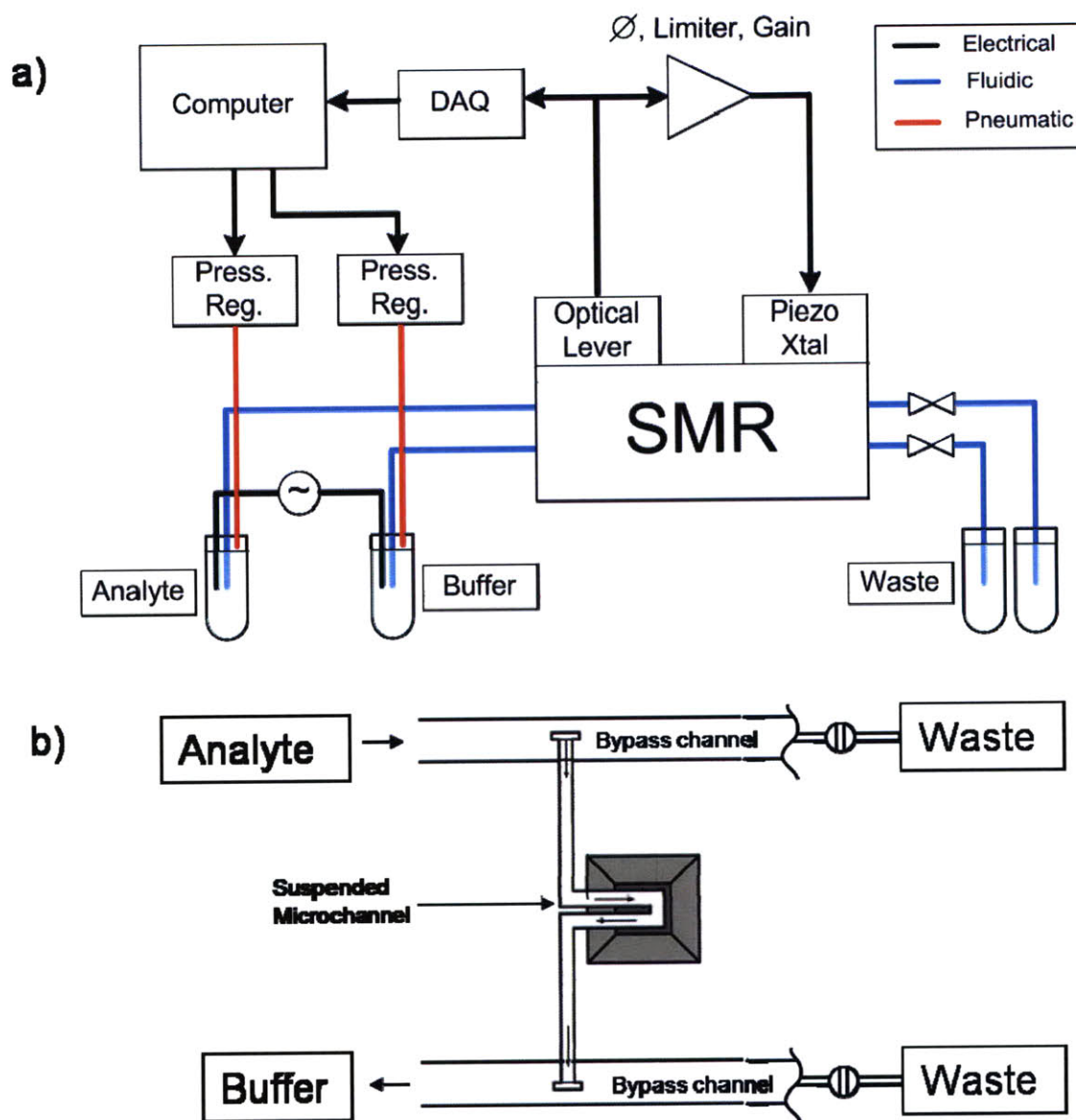


Figure 3-2: (a) Schematic diagram of the instrument. The SMR resonance frequency is measured in a feedback loop using optical lever readout and piezoelectric actuation. The rate and direction of fluid flow through the sensor is controlled electronically via a pair of air pressure regulators connected to two reservoirs which supply the sensor's two bypass channels and manually using valves at the bypass outlets. (b) Detailed schematic of the sensor. In the normal mode of operation, outlets of the bypasses are valved closed and reservoir pressures adjusted to determine the particle drift velocity.

piezoelectric drive circuit, see Appendix A.2. Electrodes for electrophoresis were integrated using a custom manifold incorporating both platinum wire electrodes and air pressure control elements (for technical drawings, see Appendix A.3). This design

allows fluid pressure to be controlled with a resolution of 10 Pa, which is needed to achieve small enough particle drift velocities for EPM measurement, while simultaneously maintaining reliable electrical contact with the fluid. Designs integrating electrodes on a smaller scale were also evaluated and found to produce unreliable electrical contact, most likely due to electrolytic gas bubbles which created small-volume interruptions in the fluid path. Electrophoretic potentials are produced by amplifying a 10 Hz sine wave from a function generator using an Apex PA-90 amplifier, the output of which directly drives the manifold electrodes.

3.2 Channel Wall Zeta Potential Measurement

The zeta potential of the channel wall was determined prior to each particle EPM measurement using a bi-directional buffer exchange technique (Fig. 3-3). The running buffer used to make particle EPM measurements was loaded into one reservoir, and the same buffer diluted by 10% with de-ionized water was loaded into the other reservoir. Both buffers were mixed with trace amounts of 500 nm-diameter dyed polystyrene microspheres (Thermo Fisher Scientific Inc., Waltham, MA) which are too small to cause a significant resonance frequency shift but large enough to provide a visible measure of fluid flow using a fluorescence microscope. Pressure regulators connected to the two reservoirs were adjusted to give the smallest pressure driven flow rate possible. This was accomplished by closing the output valves of both bypasses and observing the time needed for a tracer particle to transit the suspended microchannel. Once the bypass

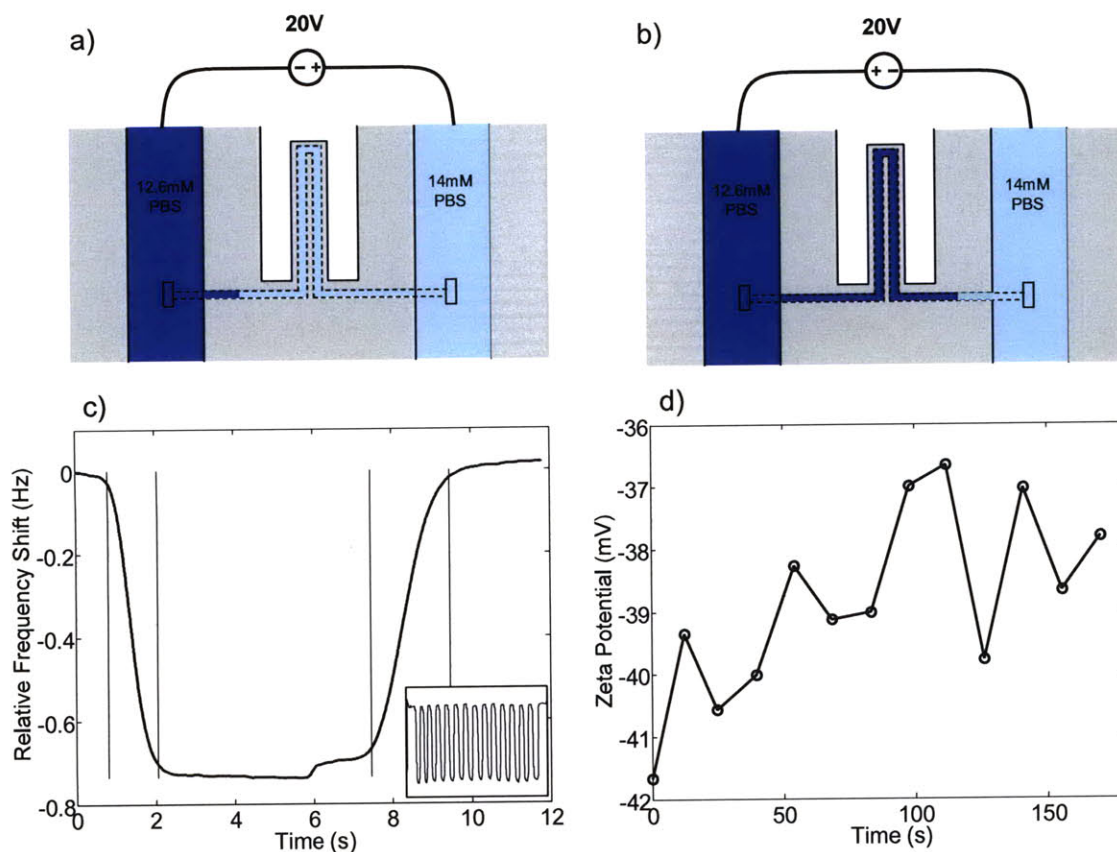


Figure 3-3: Channel wall zeta potential is measured using a bi-directional buffer exchange technique. Experimental setup for forward (a) and reverse (b) buffer exchanges. (c) Resonance frequency time course for a single cycle in which the more dense buffer first replaces the less dense one by forward EOF followed by the opposite buffer exchange due to reversal of the EOF voltage. The vertical lines indicate the times at which the interface between the two buffers enters/leaves the suspended microchannel. The overall time course for the experiment (13 cycles) is inset. (d) The wall zeta determined from the measured electro-osmotic velocities is plotted vs. the approximate time of measurement in the overall time course.

pressures were balanced, the output valves were opened to allow flow in the bypasses again and create a clean boundary between the two buffers. The output valves were then closed once more and 20V was applied between electrodes in the two reservoirs for long enough to exchange the two buffers by electro-osmotic flow. The time needed for the interface between the two buffers to travel the length of the suspended microchannel was measured as the time needed for the resonance frequency of the SMR to shift between two values corresponding to the densities of the two buffers. The length of the channel

divided by this transition time then provided an estimate of the electro-osmotic velocity. However, because this velocity contains a small pressure-driven component, the voltage applied to the electrodes was immediately reversed following the first buffer exchange so that a second measurement could be made in the opposite direction. Averaging the two net velocity measurements then cancels out the effect of the pressure gradient and leaves only the electro-osmotic component. The electro-osmotic mobility of the channel and its zeta potential were computed from the average velocity using Equations 2.10 and 2.12. This procedure was repeated at least four times and the results averaged to provide estimates of mobility and zeta potential. For the example shown in Figure 3-3, thirteen exchanges were performed, and the average mobility and zeta potential were $-2.75 \pm 0.11 \mu\text{m}\cdot\text{cm}/\text{V}\cdot\text{s}$ and $-39 \pm 1.5 \text{ mV}$ respectively. The trend towards smaller zeta potentials is believed to be caused by diffusive mixing of the two buffers at their interface, which tends to increase the time needed to register a density shift and hence reduces the measured electro-osmotic velocity. The channel's zeta potential was also found to vary significantly between devices, and from one day to the next. For example, the buffer exchange measurement was performed on a different device on two separate days, and the resulting zeta potential measurements were $-55.5 \pm 1.3 \text{ mV}$ ($n=9$) and $-51.1 \pm 2.2 \text{ mV}$ ($n=4$) respectively, where n is the number of exchanges performed. For this reason, the electro-osmotic mobility of a device is measured using the buffer exchange technique at least once immediately before every EPM measurement presented here.

3.3 Integrated Particle Measurement

As reported previously, the mean particle density for a population can be inferred by measuring the mean particle buoyant mass in at least two media having different densities. [55] Knowledge of the mean density then allows the buoyant mass measurement to be converted into either a volume or an absolute mass. In this work, cell mass is always reported as buoyant mass, and microsphere absolute masses were computed from the measured buoyant masses using the microsphere density of 1.05 g/cm^3 specified by the manufacturer. However, the instrumentation used to make the integrated measurements described here has all the capabilities needed to measure particle density as well. The particle suspension was loaded into a pressurized reservoir connected to one bypass channel of the SMR while a reservoir supplying the other bypass channel was filled with the same buffer without particles (Fig. 3-2). Air pressure regulators connected to the two reservoirs and valves at the outlets of the bypass channels determined the direction and rate of flow through the sensor. For EPM measurements, both outlet valves were closed, and the regulators were adjusted to produce a flow rate of $\sim 10\text{-}20 \text{ pL/s}$ through the suspended microchannel, which corresponded to a linear particle velocity between 400 and $800 \text{ }\mu\text{m/s}$. Significantly larger velocities were found to yield insufficient data for particle mobility determination while smaller velocities produced more frequent interactions between particles and the channel walls, which interfered with EPM measurement. Electrophoresis was induced by applying a sinusoidal potential with a frequency of 10 Hz between electrodes contained in the two reservoirs. The amplitude was chosen according to the calibration described in Section 4.1 to produce an electric

field in the suspended microchannel with a typical magnitude of 585 V/cm for most experiments.

3.4 Signal Processing

To predict the functional form of the resonance frequency response from oscillating particle transits, and as a preliminary test of the theory described in Section 2.3, simulations were carried out in MATLAB for a system where a 2.2 μm polystyrene microsphere transits the 210 μm -long suspended microchannel with a drift velocity of $v_d = 420 \mu\text{m/s}$. Three scenarios were simulated in which the particles had either no spatial amplitude or a spatial amplitude of 6.7 μm or 13.4 μm (Fig. 3-4). The position of the particle in each case is a linear superposition of a drift component (black curve in Fig. 3-4A) and a 10Hz oscillatory component of the appropriate amplitude. In the simulations with non-zero spatial amplitude, the position at the tip was approximated by making the maximum allowable position equal to the cantilever length. The resonance frequency response, $f(t)$, for each particle as shown in Figure 3-4B was computed by applying Equation 2.7 to the simulated position time courses. The frequency responses of the oscillating particles are intended to simulate exact values of the sampled frequency data ($f(t)$ in Equation 2.14), while the frequency response of the particle with zero spatial amplitude is intended to simulate the exact form of the band-stop filtered time course, $F_{BS}[\tilde{f}(t)]$. A band-pass filter, implemented as a finite impulse response filter with a 202 ms window and cutoff frequencies of 5 and 15 Hz, was applied to the frequency

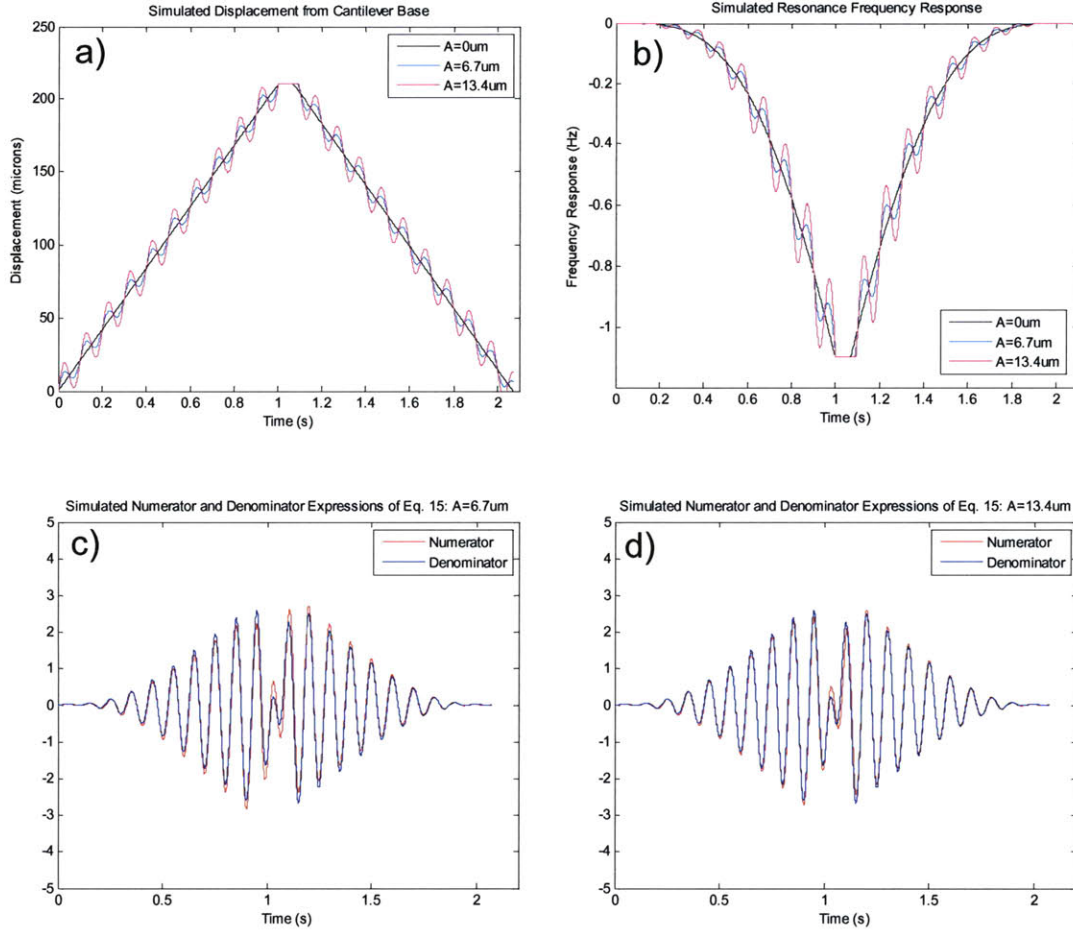


Figure 3-4: Simulation of the transit of a $2.2\ \mu\text{m}$ polystyrene microsphere transiting a cantilever with a $3\ \mu\text{m} \times 8\ \mu\text{m} \times 200\ \mu\text{m}$ suspended microchannel oscillating with three different spatial amplitudes. Position (a) and resonance frequency (b) time courses are computed for each spatial amplitude. (c-d) Following the analysis of Section 2.3, the numerator expression of Eq. 15 (red line, normalized here by $v_d/(\omega A)$) is compared with the denominator expression for the two non-zero spatial amplitudes.

responses of each of the oscillating particles, and the resulting filtered time courses were differentiated with respect to time. Numerical derivatives were carried out using 3-point forward/reverse finite differences for the first and last two points, respectively, and a 5-point stencil finite difference for all other points. The differentiated band-pass filtered time courses were then multiplied by the drift velocity and divided by both the angular frequency and the spatial amplitude. Note that this differs from the numerator expression in Equation 2.15 by a factor of the inverse spatial amplitude. This was done intentionally

so that the numerator and denominator expressions could be compared directly. The simulated band-stop filtered time courses were first modulated with a 10 Hz sinusoid of unit amplitude, differentiated in the same way as was the band-pass filtered time course, and finally filtered with the same band-pass filter. The normalized numerator and denominator expressions are overlaid for the two spatial amplitudes that were simulated in Figures 3-4C and 3-4D. These simulations were performed primarily to establish that the numerical signal processing algorithms employed do not bias or distort signals in a way that would prevent their comparison in the computation of spatial amplitude. The high degree of similarity between the numerator and denominator time courses indicates that this was successful. Furthermore, these simulations give accurate predictions for the responses that are observed in actual SMR experiments, which indicates that the phenomena observed in experiments are consistent with the model.

When applied to resonance frequency time courses recorded from the SMR during the transit of actual 2.2 μm polystyrene microspheres, the analysis described in Section 2.3 produced results which are typified by those shown in Figure 3-5 for one such particle. This analysis generally consists of computing time courses representing the numerator and denominator expressions of Equation 2.15 and comparing them to estimate the spatial amplitude. Some practical issues must be considered in the application of Equation 2.15 to real particle data. Firstly, to eliminate high-frequency noise arising from digitization of the optical lever signal for fast acquisition of the resonance frequency, the raw data are low-pass filtered using a 3rd-order Savitzky-Golay smoothing filter with a width of 31 samples. The optical lever signal is typically sampled at $\sim 1\text{kHz}$, so the

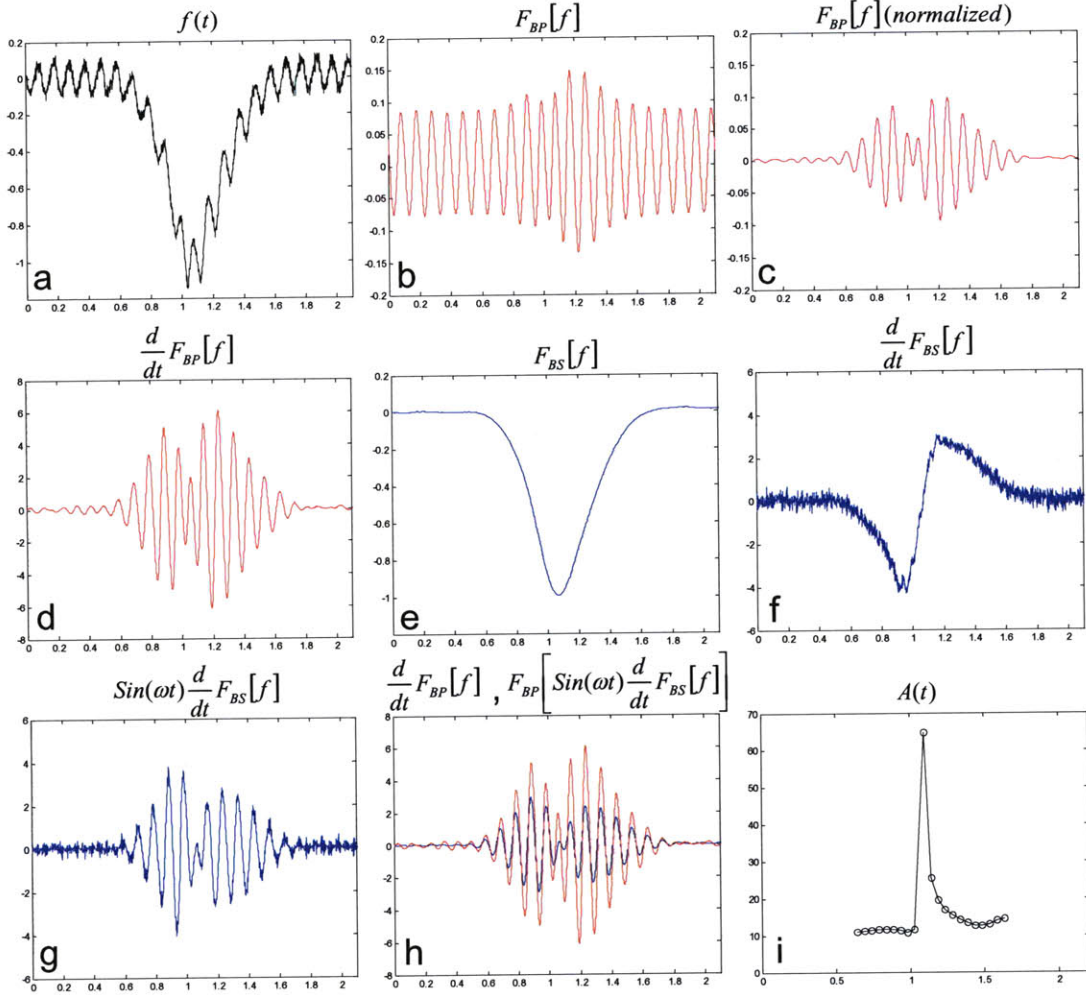


Figure 3-5: Analysis of a resonance frequency time course for the transit of a 2.2 μ m polystyrene microsphere transit subject to a 10 Hz electric field with a peak field strength of 585 V/cm. Raw data (a) are filtered to separate the components of the signal due to drift and oscillatory motion of the microsphere. Band-pass filtered data are shown before (b) and after (c) subtraction of the oscillatory background, and time-derivative of the normalized signal (d). Band-stop filtered data (e) and its time derivative before (f) and after (g) 10 Hz modulation. The spatial amplitude of oscillation of the microsphere is estimated using Eq. 15. (h) Peak values of the time courses corresponding to the numerator expression (red line, shown here before scaling by v_d/ω) and denominator (blue line) are divided to produce the spatial amplitude time course (i).

filter window is ~ 30 ms. Secondly, the resonance frequency signal exhibits a steady 10 Hz oscillation even when the cantilever contains no particle (see Fig. 3-5A and Section 4.5). To eliminate this coupling, a band-pass filter is applied to the smoothed frequency data as in the simulations described above, then a sinusoid is fit to a baseline segment of

the band-pass filtered signal, and the resulting fit is subtracted from the entire time course (Fig. 3-5B,C). The band-pass filter used is a finite impulse response filter with a 404-point window and cutoff frequencies of 9 and 11 Hz. The phase from the fit is reserved in order to construct the modulating sinusoid used in the denominator expression. The final step in constructing the numerator expression is numerical differentiation of the band-pass filtered signal with respect to time, which is carried out using the same algorithm as the one used in the simulations described earlier in this section (Fig. 3-5D). The first step in constructing the denominator expression is band-stop filtering of the raw frequency data (Fig. 3-5E). This is performed using a finite impulse response filter with a 404-point window and cutoff frequencies of 5 and 15 Hz. Two important parameters are determined from the band-stop filtered signal. Firstly, the drift velocity is computed by dividing the length of the suspended microchannel by the baseline width of the peak. Secondly, the buoyant mass of the particle is determined by multiplying the height of the peak by the mass sensitivity of the cantilever, which has been empirically determined to be -268 fg/Hz. [55] The band-stop filtered signal is then numerically differentiated with respect to time (Fig. 3-5F). Because the differentiation step amplifies high-frequency noise present in the smoothed frequency signal, a 3rd-order Savitzky-Golay filter with a 201-point window is applied after differentiation. This signal is then modulated with a sinusoid with unit amplitude and whose phase is matched with that of the function which was fit to the oscillatory background signal (Fig. 3-5G). The final denominator expression is produced by applying the same band-pass filter as was used in the numerator expression to the modulated derivative of the band-stop filtered signal. An example of the final numerator and denominator time courses is shown in Figure 3-5H.

The spatial amplitude has been computed in two different ways: by simple division of local extrema of the numerator and denominator time courses, and using amplitude demodulation. The result of the first scheme is shown in Figure 3-5I. This scheme produced the most accurate results when compared with particle zeta potential measurements made on commercial instruments, as discussed in Section 4.6, and has therefore been employed in all subsequent analyses. The drawback of this approach is the loss of temporal resolution since a peak only occurs every 50 ms. In addition, because the resonance frequency is not sensitive to changes in the particle's position near the cantilever's tip, the spatial amplitude exhibits a reduced signal-to-noise ratio during this brief event. As a result, several points must be ignored in the spatial amplitude time course. However, the remaining data are generally found to be adequate for the computation of a particle's spatial amplitude for a typical particle transit which lasts more than a second and produces over 20 measures of spatial amplitude. The second method used to compute spatial amplitude consisted of an amplitude demodulation scheme. In this scheme, both the numerator and denominator time courses are initially multiplied by a 10 Hz sinusoid of unit amplitude and whose phase is matched with that of the function which was fit to the oscillatory background signal. Next, a low pass filter, implemented as a finite impulse response filter with a 404-pt window and a cutoff frequency of 15 Hz, is applied to both modulated signals to recover their envelopes. These two envelope functions can then be divided directly to determine the spatial amplitude. An example of the amplitude modulation scheme as it is applied to the resonance frequency time course from the transit of a 2.2 μm polystyrene microsphere is shown in Figure 3-6. The main drawback of this scheme is that there is very little flexibility in the choice of carrier

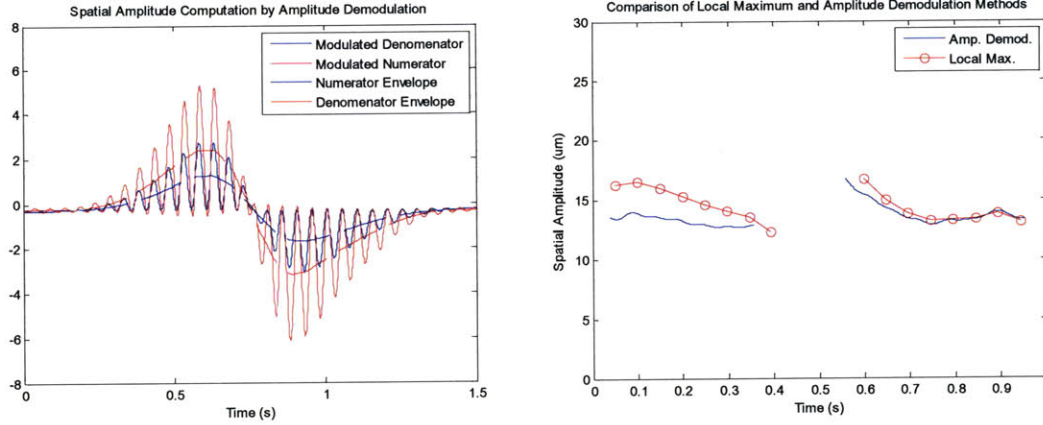


Figure 3-6: (a) Signals used to compute the spatial amplitude of a representative 2.2 μm polystyrene microsphere using an amplitude demodulation scheme. (b) Comparison of the resulting spatial amplitude as computed by amplitude demodulation and by comparison of local maxima.

frequency since it is determined by the electrophoretic oscillation frequency. Higher oscillation frequencies would allow a higher cutoff to be used in the mixdown step, producing less distortion of the envelopes, but since the spatial amplitude is inversely proportional to the oscillation frequency, the SNR of the EPM measurement will decrease accordingly. As seen from Figure 3-6B, the distortion affects the numerator and denominator signals similarly so that it is mostly cancelled out when the two signals are divided to compute the spatial amplitude.

Chapter 4

Instrument Characterization

4.1 Passivation Oxide Breakdown

In order to support electric fields needed for electrophoresis in the suspended microchannel of the SMR, this channel must be passivated with a thermal oxide layer. When electrophoretic voltages are applied to this U-shaped channel, an inherently large voltage difference exists between the two halves of the channel at the cantilever's base (see Figure 3-2B), where the separation between the two halves is only 5 μm . For large enough voltages, this situation can produce dielectric breakdown of the passivation oxide, resulting in conduction of current through the silicon. Because this current is supported by electrolysis of water, the resulting release of gas bubbles interrupts fluid flow in the channel, preventing further measurement.

The breakdown of the passivation oxide has been characterized empirically for three different SMR devices. The first is an SMR with a suspended microchannel having

cross-sectional dimensions of $3 \times 8 \text{ }\mu\text{m}$ with no passivation oxide (referred to from here on as the NSMR or native SMR). The second device has the same physical dimensions as the first, but its channel has been passivated using the protocol described in Section 3.1 (referred to as the OSMR). The third device has cross-sectional dimensions of $15 \times 20 \text{ }\mu\text{m}$, and the same passivation oxide as the second (referred to as OLSMR). One important difference between the fabrication processes for the small-channel and large-channel devices is the etch which opens the ends of the buried suspended microchannel (see Appendix A.1.1) and also defines the cantilever outline. This etch was performed by means of a standard reactive ion etch (RIE) for the small-channel devices. In the case of the large-channel SMR, the cantilever outline would be adversely affected by the high degree of undercut for a standard RIE process, and hence a deep reactive ion etch (DRIE) which produces a higher aspect ratio for the channel sidewall was used instead. A side-effect of the DRIE recipe selected is that it produces greater roughness than the RIE recipes used on small-channel devices.

Breakdown voltages were determined by measuring the current-voltage response of the suspended microchannel while filled with 15 mM phosphate-buffered saline (PBS) using a Keithley 237 source-measure unit (Keithley Instruments Inc., Cleveland, OH). The devices were simultaneously observed using a white light microscope connected to a CCD camera to record the voltage at which electrolytic gases were produced. All devices had reservoirs made from plastic pipette tips attached directly to their surfaces using UV epoxy. The reservoirs were connected electrically to the source-measure unit via platinum wire electrodes (0.5mm, Sigma Aldrich). Current measurements were made for a series

of increasing voltages and plotted against the voltage across the suspended microchannel to produce the I-V curves shown in Figure 4-1. The voltage across the suspended microchannel is determined from the voltage applied to the electrodes by treating the bypasses and suspended microchannel each as linear resistors with a constant resistivity whose resistance is proportional to cross-sectional area and inversely proportional to length. This is possible because the dimensions of these channels are determined by well-characterized microfabrication processes. The oxide breakdown voltage is defined as the largest voltage measured which did not result in either a deviation from the linear I-V response expected for buffer or visible electrolytic gas formation in the CCD image, and is tabulated along with the corresponding electric fields for the three devices in Table 4.1. For the NSMR and OSMR, oxide breakdown was observed by deviation from the linear I-V response before any bubbles were seen in their channels. For these devices,

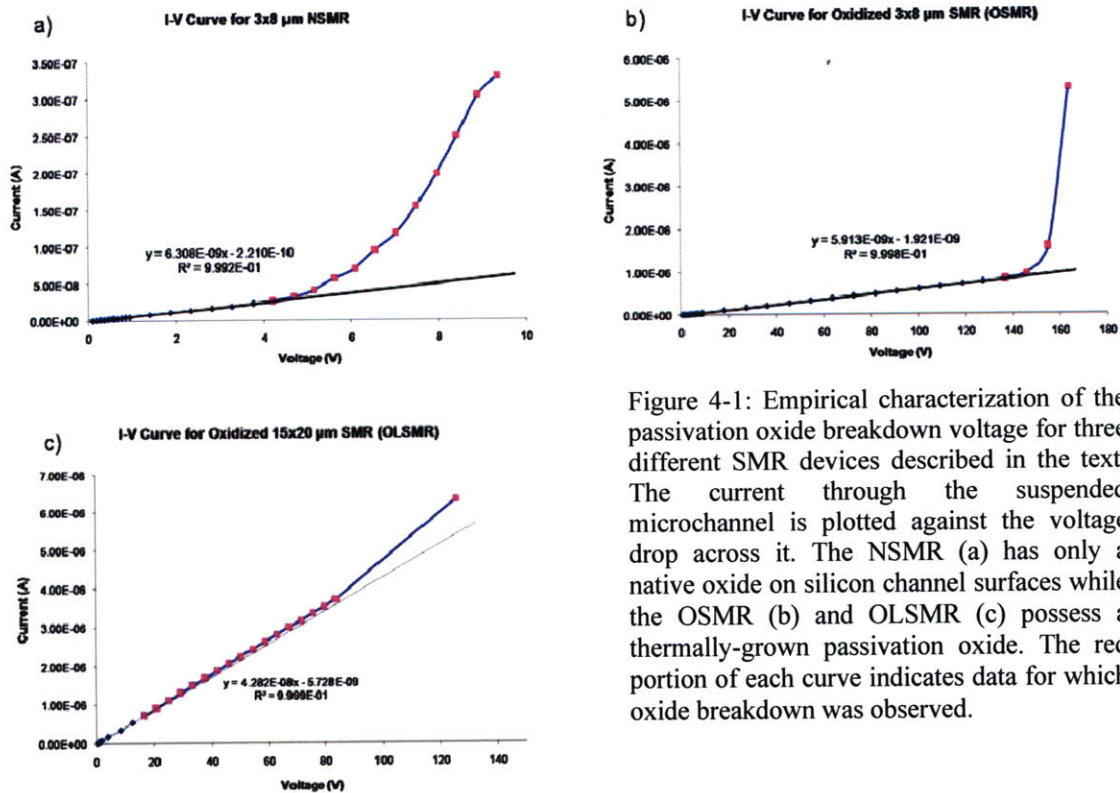


Figure 4-1: Empirical characterization of the passivation oxide breakdown voltage for three different SMR devices described in the text. The current through the suspended microchannel is plotted against the voltage drop across it. The NSMR (a) has only a native oxide on silicon channel surfaces while the OSMR (b) and OLSMR (c) possess a thermally-grown passivation oxide. The red portion of each curve indicates data for which oxide breakdown was observed.

<i>Device</i>	<i>Oxide Thickness, Approx. (nm)</i>	<i>Breakdown Voltage (V)</i>	<i>Breakdown Electric Field (V/cm)</i>
NSMR	0.5	3.7	45
OSMR	80	137	1650
OLSMR	80	13	119

Table 4.1: Breakdown voltages and electric fields of the passivation oxide for the three different devices characterized, as determined from the data shown Figure 4-1.

the magnitude of the electric field at breakdown is comparable to similar measurements in the literature. [56] For the OLSMR, bubbles were observed when the voltage drop was only $\sim 17V$, whereas the I-V response remained linear until the voltage was much larger (Fig. 4-1C). This observation, and the much more gradual deviation from linearity observed for the OLSMR compared to the other two devices, may be due to the fact that it was necessary to induce flow in the channel to make the measurements for the OLSMR. This was necessary only for the OLSMR, because without flow, the electrolysis gases would have filled up the channel, interrupting the flow of current and preventing further measurement. Examples of electrolysis which were captured with the CCD camera for the OLSMR are shown in Figure 4-2. For this particular device, the first gas bubbles appeared to originate from the outer sidewall of one of the openings of the buried channel.

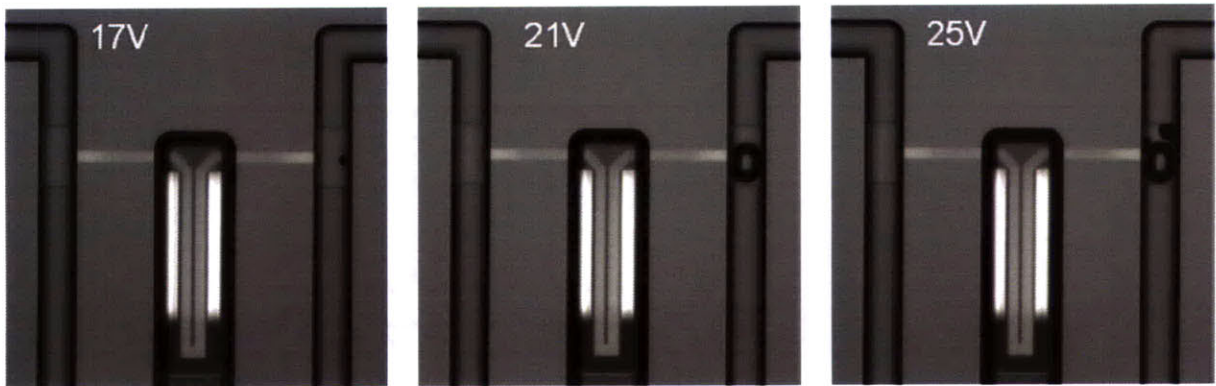


Figure 4-2: Breakdown of the passivation oxide for an OLSMR with different voltages applied to the ends of the suspended microchannel. Nucleation of electrolytic gases appears to come from the right sidewall of the right port of the channel.

For this reason, the low oxide breakdown voltage for the OLSMR is thought to be due to non-uniformity of the thermal oxide which results from the higher degree of sidewall roughness typically associated with the DRIE recipe used to fabricate the OLSMR relative to the RIE recipe used to fabricate the OSMR.

4.2 Electric Field Measurement

Measurement of the electric field in the suspended microchannel during particle measurements required further system characterization because simultaneous pressure and voltage control requires that the two sample reservoirs are connected to the device through tubes and valves having unknown internal geometries (see Fig. 3-2, Section 3.1). First, the electrical conductivity of the device alone was determined using linear regression of the I-V responses shown in Figure 4-1 for voltages below oxide breakdown. Next, the device was mounted in the fluidic manifold used to make particle measurements and the conductance of the entire fluidic circuit was measured by connecting the source-measure unit to the manifold's integrated electrodes, which are used for particle electrophoresis. The two conductances were compared in order to determine how voltages applied to the manifold electrodes are divided between the device itself and tubing external to it. This voltage divider was then multiplied by the one determined previously for division between the suspended microchannel and the bypass channels to give a quantitative figure for the electric field experienced by a particle inside the sensor as a function of the electrophoresis power supply voltage. For

example, it was determined for one device that a sinusoidal voltage of $125 V_p$ applied to the manifold produced a voltage of $48.4 V_p$ across the $828 \mu\text{m}$ -long microchannel connecting the two bypasses, corresponding to a maximum electric field of 585 V/cm .

4.3 Device Actuation

The amplitude of the drive voltage applied to the piezo crystal determines the oscillation amplitude of the cantilever and, hence, the centripetal force applied to particles as they pass through, as described in Section 2.2. Since both particle inertia and SNR increase with tip amplitude, selecting the appropriate drive amplitude is a compromise between the need to minimize particle inertia and maximize SNR. The preferred method for achieving this is to characterize the tip amplitude as a function of drive voltage and determine the maximum drive voltage before the onset of inertial trapping using the model of Section 2.2. However, this was not undertaken for two reasons. Firstly, the SNR of the system was found to be extremely sensitive to small changes in the contact interface between the piezo crystal and the device. Hence it was expected that a characterization would become invalid if, for example, the device was removed from the fluidic manifold to unclog a bypass channel. Secondly, attempts to characterize the tip amplitude using the laser Doppler velocimetry tools at MIT indicated that these tools were unreliable. Therefore, rather than measuring the tip amplitude, the noise characteristics of the system were determined as a function of the drive voltage to determine the minimum acceptable tip amplitude, and this procedure was repeated as

necessary to minimize the occurrence of inertial trapping of particles. As seen in Figure 4-3, the RMS noise level of the resonance frequency signal, when sampled at 1 kHz and filtered with a 3rd-order 31-point Savitzky-Golay filter, typically has a plateau for drive voltages larger than 300 mV_{p-p} and increases rapidly for voltages below 150 mV_{p-p}. The surprising feature of this system is that it consistently has a noise minimum. For this reason, the drive voltage was at first arbitrarily set to the minimum value which reproduces the plateau noise level observed for large drive voltages, a practice which has been found empirically to produce tip amplitudes which do not result in inertial trapping for small particles of the type described here.

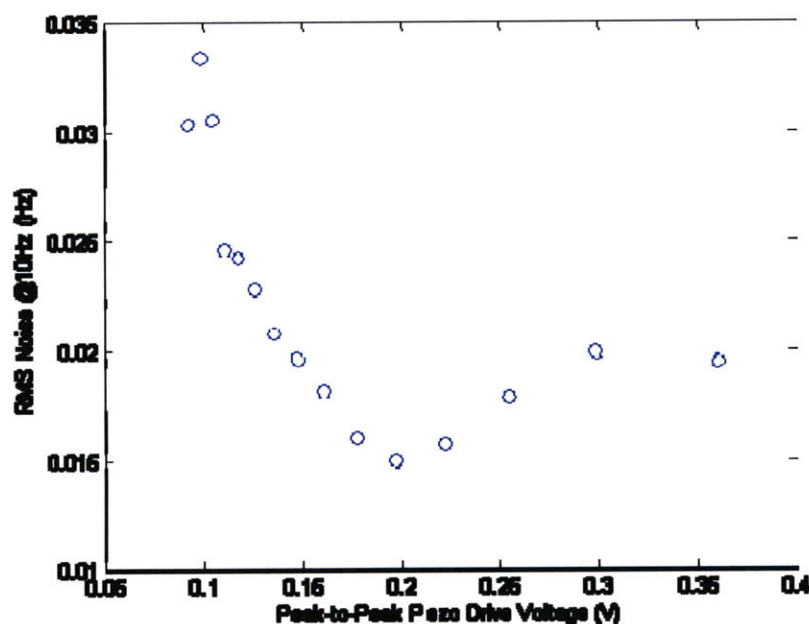


Figure 4-3: Empirical characterization of resonance frequency noise amplitude as a function of the drive voltage applied to the piezo crystal.

4.4 Computational Error Analysis

In order to explore the validity of the approximations made in Section 2.3 to compute the spatial amplitude, we consider the complete Taylor expansion of the resonance frequency as a function of particle position $f(x)$:

$$f(v_d t + A \sin(\omega t)) = f(v_d t) + A \sin(\omega t) f'(v_d t) + \frac{A^2}{2!} \sin^2(\omega t) f''(v_d t) + \dots$$

Presently, we will only keep up to second derivative terms, and we will examine the rest of the series later. The time derivative of the series is then:

$$\frac{df}{dt} = v_d f'(v_d t) + \omega A \cos(\omega t) f'(v_d t) + v_d A \sin(\omega t) f''(v_d t) + \frac{\omega A^2}{2} \sin(2\omega t) f''(v_d t) + \dots$$

As in the Section 2.3, we assume that the spatial amplitude is small compared with the length of the cantilever, which leads to the approximations:

$$f'(v_d t) \approx \frac{1}{v_d} \frac{dF_{BS}[f]}{dt}, \quad f''(v_d t) \approx \frac{1}{v_d^2} \frac{d^2 F_{BS}[f]}{dt^2}$$

When applied to the differentiated series, this yields:

$$\frac{df}{dt} \approx \left(1 + \frac{\omega A}{v_d} \cos(\omega t) \right) \frac{dF_{BS}[f]}{dt} + \frac{A}{v_d} \left(\sin(\omega t) + \frac{\omega A}{2v_d} \sin(2\omega t) \right) \frac{d^2 F_{BS}[f]}{dt^2} + \dots$$

First we consider the relative size of the two first derivative terms after band-pass filtering. A comparison of the magnitude of these two expressions for a typical 2.2 μm -diameter polystyrene microsphere is shown in Figure 4-4B. As described in Section 3.4, the middle four points of the extracted spatial amplitude data (Fig. 4-4A) are thrown out by the software. For the remaining set of time points, the ratio of the standard deviations of these two components is ~ 176 . This justifies dropping the first of the two first

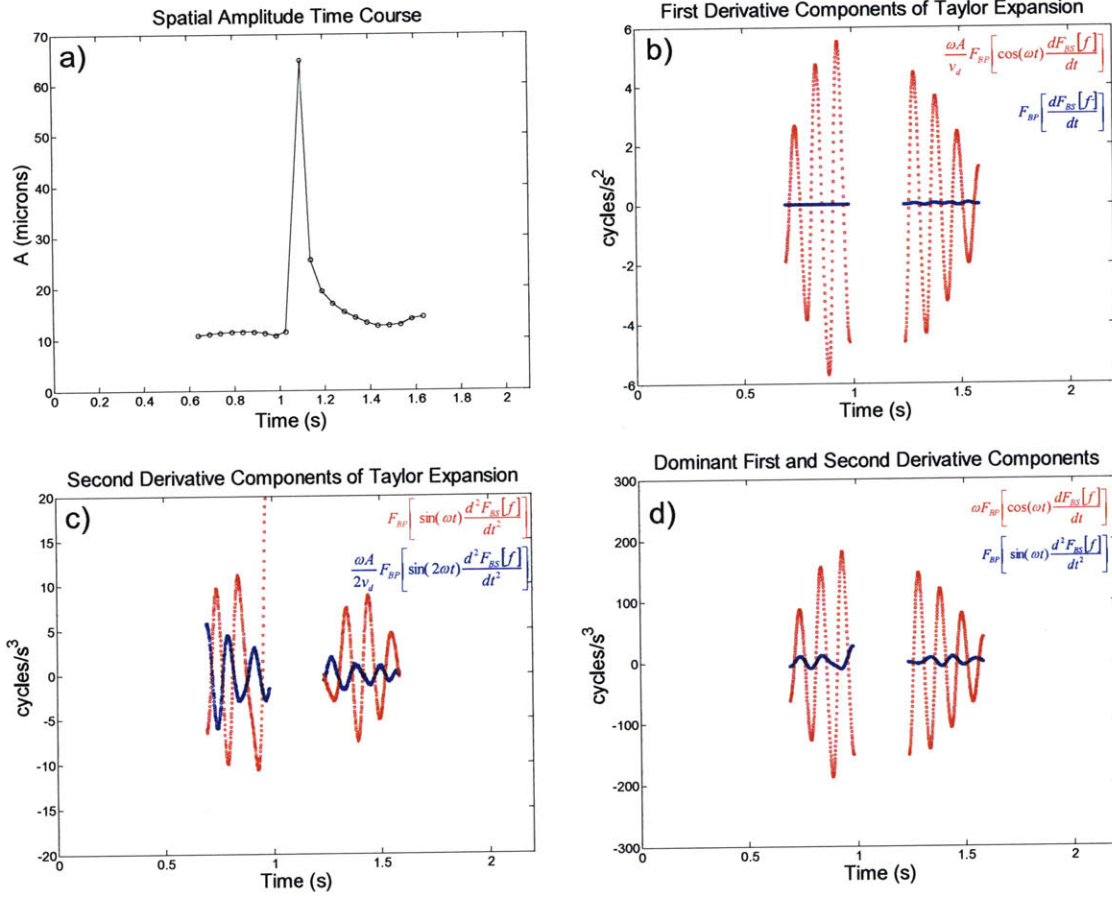


Figure 4-4: Experimental data used to approximate typical errors in the computation of spatial amplitude for a 2.2 μm -diameter polystyrene microsphere. (a) Spatial amplitude time course. (b)-(d) Time courses of low-order terms in the Taylor expansion of the time derivative of $F_{BP}[f]$, with their functional forms inset.

derivative terms, leaving:

$$\frac{d}{dt} F_{BP}[f] \approx \frac{A}{v_d} F_{BP} \left[\omega \cos(\omega t) \frac{dF_{BS}[f]}{dt} + \left(\sin(\omega t) + \frac{\omega A}{2v_d} \sin(2\omega t) \right) \frac{d^2 F_{BS}[f]}{dt^2} + \dots \right]$$

Next we consider the relative contributions of the two second derivative terms after filtering, which are shown in Figure 4-4C. The second of these terms is smaller because its modulation frequency of 2ω lies outside the pass-band of the filter, and the ratio $\omega A/2v_d$ is approximately unity for a typical microsphere. As a result, the first term is approximately three times larger than the second for the microsphere in question. We therefore retain the larger of the two second derivative terms for comparison with the

only remaining first derivative term, which is found to be approximately fourteen times larger (Fig. 4-4D). This result, combined with the result of Fig. 4-4C, justifies dropping both of the second derivative terms. After making this simplification, we find that, in general, for $n \geq 2$, the series will have two terms of n^{th} order of the form:

$$\frac{d}{dt} F_{BP}[f] \approx F_{BP} \left[\dots + \frac{\sin^{n-2}(\omega t)}{(n-1)!} \left(\frac{A}{v_d} \right)^{n-1} \left(\sin(\omega t) + \frac{\omega A}{2v_d} \sin(2\omega t) \right) \frac{d^n F_{BS}[f]}{dt^n} + \dots \right]$$

We expect that the efficiency of the band-pass filter observed in Figure 4-4C will apply to higher-order terms of the series as well, and hence we can throw away all of the terms modulated at a frequency of 2ω and simply consider the series:

$$\frac{d}{dt} F_{BP}[f] \approx \frac{\omega A}{v_d} F_{BP} \left[\cos(\omega t) \frac{dF_{BS}[f]}{dt} + \frac{1}{\omega} \sum_{n=2}^{\infty} \frac{\sin^{n-1}(\omega t)}{(n-1)!} \left(\frac{A}{v_d} \right)^{n-2} \frac{d^n F_{BS}[f]}{dt^n} \right]$$

In addition, since terms corresponding to odd values of n will contain even powers of $\sin(\omega t)$ having a fundamental frequency of 2ω , then using the same reasoning, these terms will also be excluded by the band-pass filter, yielding:

$$\frac{d}{dt} F_{BP}[f] \approx \frac{\omega A}{v_d} F_{BP} \left[\cos(\omega t) \frac{dF_{BS}[f]}{dt} + \frac{1}{\omega} \sum_{i=1}^{\infty} \frac{\sin^{2i-1}(\omega t)}{(2i-1)!} \left(\frac{A}{v_d} \right)^{2i-2} \frac{d^{(2i)} F_{BS}[f]}{dt^{(2i)}} \right]$$

Therefore as long as the magnitude of the $(2i)^{\text{th}}$ derivative of the band-stop filtered data satisfies the growth condition

$$\frac{\left\| F_{BP} \left[\sin^{2i-1}(\omega t) \frac{d^{(2i)} F_{BS}[f]}{dt^{(2i)}} \right] \right\|}{\omega \left\| F_{BP} \left[\cos(\omega t) \frac{dF_{BS}[f]}{dt} \right] \right\|} \ll (2i-1)! \left(\frac{v_d}{A} \right)^{2i-2}, i \geq 1$$

then the corresponding term can be neglected. This has already been demonstrated for the $i = 1$ case, where we found expression on the LHS to be fourteen times smaller than

the RHS. A similar analysis for $i = 2$ reveals that the LHS expression evaluates to only one fifth of the RHS expression. However, this growth behavior is not due to the true functional form of these derivatives, but rather the exponential amplification of small noise components present in the original band-stopped signal produced by repeated differentiation. This artifact can be eliminated by applying a low-pass filter in both the numerator and denominator time courses after the first differentiation step, which increases the ratio between the RHS and the LHS to ~ 129 for the $i = 2$ case. It is then reasonable to expect higher order derivatives to obey this growth condition as well. As long as this condition is met, the overall Taylor series for the resonance frequency response is reduced to the approximate expression used in Equation 2.15:

$$\frac{d}{dt} F_{BP}[f] \approx \frac{\omega A}{v_d} F_{BP} \left[\cos(\omega t) \frac{dF_{BS}[f]}{dt} \right]$$

4.5 Coupling

The observation of a steady 10 Hz oscillation in the resonance frequency signal when there is a 10 Hz electric field but no particle present in the suspended microchannel motivated further analysis, which has been carried out in the form of an empirical characterization. Two devices were examined: an OSMR and an OLSMR (see Section 4.1 for physical dimensions and characterization of the passivation oxide breakdown for these two device designs). Out of these two, the OSMR was characterized more fully because it had a relatively high oxide breakdown field of 1650 V/cm in comparison to the OLSMR, whose oxide was found to break down at a much lower electric field of 119 V/cm.

4.5.1 OSMR

For the OSMR, the shape and magnitude of the oscillatory background signal were found to be dependent both on electric field strength and buffer ionic strength, as illustrated in Figure 4-5. To generate each of the three curves shown, the device was first filled with a PBS solution diluted to either 140mM, 14 mM or 3.5 mM, a 10-Hz sinusoidal voltage was applied to the manifold electrodes to produce an electric field with a specified peak amplitude according to the calibration described in Section 4.2, and the resonance frequency was recorded for one second for each of ten different electric field amplitudes ranging from zero to 585 V/cm. The resulting resonance frequency time courses were

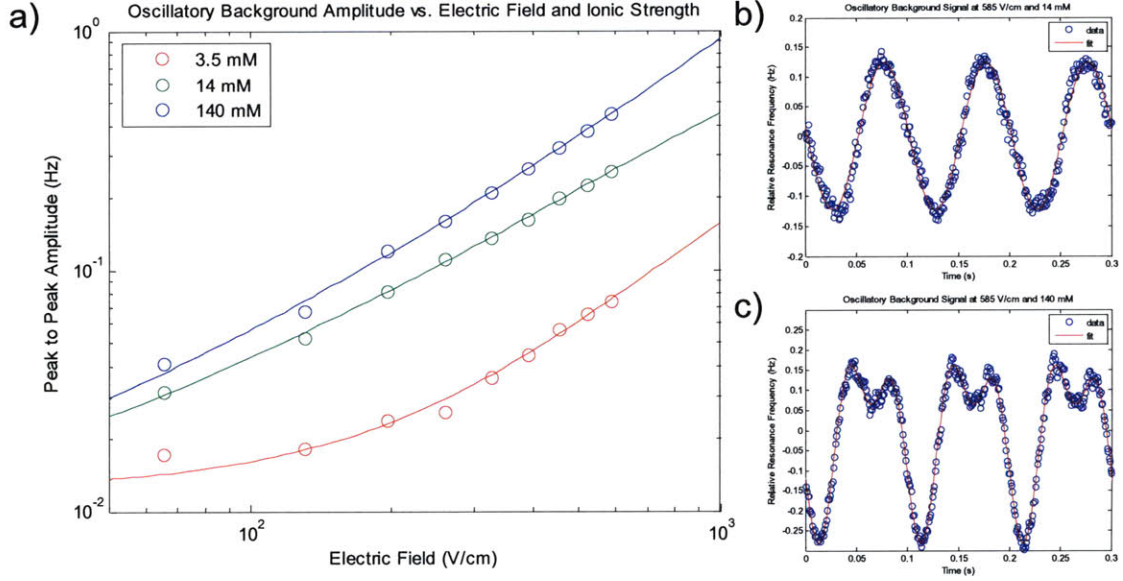


Figure 4-5: (a) For an OSMR filled with 140 mM PBS, the dependence of the peak-to-peak amplitude of the oscillatory background signal on peak amplitude of a 10-Hz sinusoidal electric field and buffer ionic strength is measured (open circles) and fit to a polynomial (lines). Fitting of the frequency time course data at the largest field strength reveals that the background is purely 10 Hz at 14 mM (b) but contains a 20-Hz component at 140 mM (c).

well described by 10-Hz sinusoids for the two lower buffer concentrations, but at 140 mM, there was a distinct 20-Hz component to the signal. The time course data were fit using the following two-frequency model:

$$f(t) = A_0 + A_1 \sin(2\pi f_1 t + \phi_1) + A_2 \sin(4\pi f_1 t + \phi_2)$$

where A_0 , A_1 , A_2 , f_1 , ϕ_1 , and ϕ_2 are fitting parameters. A similar model which superposed two 10-Hz waveforms of variable amplitude and phase was not able to converge, whereas the doubling in frequency of the second waveform produced the highly convergent results seen in Figure 4-5C. The peak-to-peak amplitude of the background signal plotted in Figure 4-5A is computed as the difference between the maximum and minimum values of the fit. For each of the three buffer concentrations measured (3.5, 14 and 140 mM), the background amplitude versus electric field strength data were fit to a generalized polynomial and the resulting best-fit curves were found to have exponents of 0.71 ± 0.41 ,

0.98±0.07 and 1.12±0.12 respectively over the range of electric fields measured. Hence the background amplitude can be considered to vary linearly with electric field strength at the upper two buffer concentrations, but the dependence is poorly defined at 3.5 mM.

Next, the spectral properties of the oscillatory background signal were examined for an OSMR filled with 14 mM pBS. Because the amplitude of the background signal is found to drop off rapidly for increasing frequencies, a relatively large electric field amplitude of 945 V/cm was used in this experiment. The electric field was initially applied at a frequency of 10 Hz for a 10 second period, then increased by 10 Hz every 10 seconds for a total of 50 seconds. Out of each of these periods, one second of data was sampled and its power spectral density computed, as shown in Figure 4-6. The data collected at 50 Hz were omitted because the signal component at the excitation frequency was found to be below the background noise level. For smaller excitation frequencies, the power spectral density at the excitation frequency is found to decrease logarithmically with frequency.

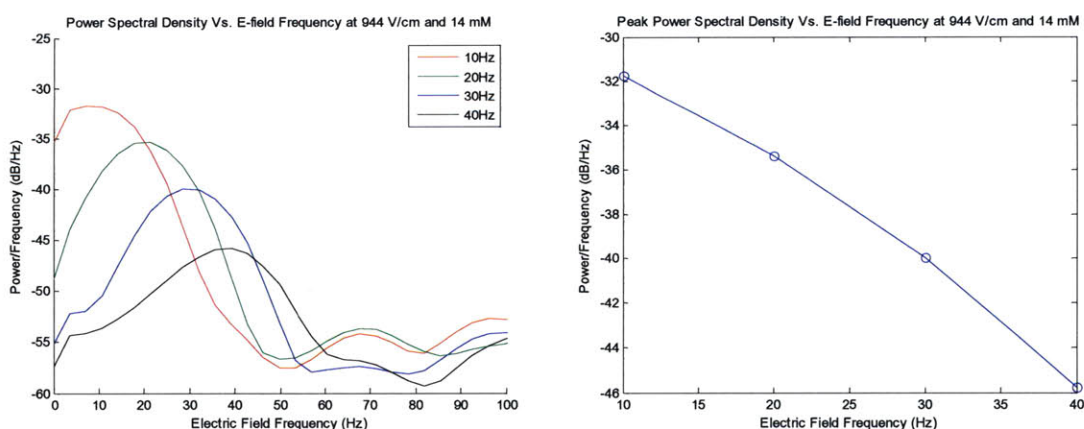


Figure 4-6: (a) For an OSMR filled with 14 mM PBS, the power spectral density of the oscillatory background signal was determined at a peak electric field strength of 944 V/cm and frequencies ranging from 10Hz to 40Hz. (b) The power spectral density at the excitation frequency is found to decrease linearly with frequency.

Finally, the phase of oscillatory background signal for the OSMR was compared to the phase of the electrophoretic drive voltage applied to the manifold electrodes for different magnitudes of the drive voltage. These two signals were acquired simultaneously through the same data acquisition interface, a National Instruments PCI-MIO-16E-1, with the optical lever signal connected to the frequency counter input and the electrophoretic drive signal connected to one of the analog inputs after a resistive voltage division of a hundred-fold. Since the starting times of acquisition for the two signals could not be made exactly the same, the acquired data were assigned time values starting with the end points and counting backwards. Both signal time courses were sampled at time intervals representing integer multiples of the excitation frequency, and each of these samples was fit to a simple 10-Hz sinusoid. The phases of the two fits for each sampling period could then be subtracted to determine the relative phase as a function of time, and the whole procedure was executed for progressively increasing magnitudes of the drive voltage. This is demonstrated for a working OSMR in Figure 4-7, where 61.6 V_p was applied to

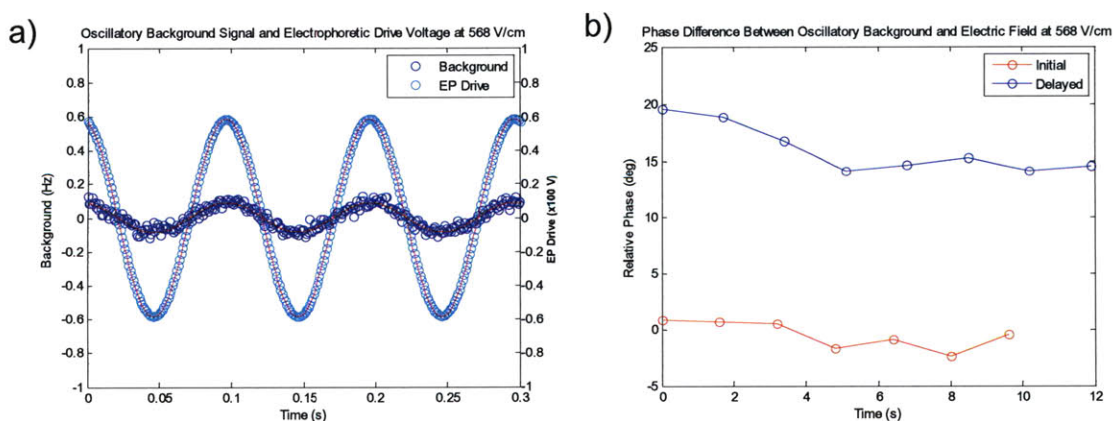


Figure 4-7: For a working OSMR filled with 14 mM PBS, the phase of the oscillatory background signal was compared to that of the electrophoretic drive voltage which is applied to the manifold electrodes. (a) The two signals are shown at a channel electric field amplitude of 568 V/cm. (b) The phase difference was initially found to be stable at a negligible level (red curve), but after the electric field had been applied for several hours, it was found to increase (blue curve).

the manifold electrodes, resulting in a channel electric field of 568 V/cm.

Data were acquired for ~10 seconds and the phase was measured on one-second long samples at ~1.5 second intervals. The first time this test was conducted, analysis of the data showed no difference in phase between the two signals within the uncertainty of the measurement. However, after the electric field had been applied to this device for several hours, a measurable phase difference was observed, and it was found to decrease with time. To study the effects of even higher electric fields on the relative phase of the system, a separate OSMR which had previously shown signs of oxide breakdown was employed. The previously described test at 568 V/cm was repeated, only this time the data were acquired for one hour, and one-second long samples were processed approximately once per minute. As seen in Figure 4-8, phase differences approaching ninety degrees could be observed when the electric field approached 1 kV/cm. Both the initial phase difference and the rate of change in phase (determined by linear regression to the data and summarized in Table 4.2) were found to increase with increasing field.

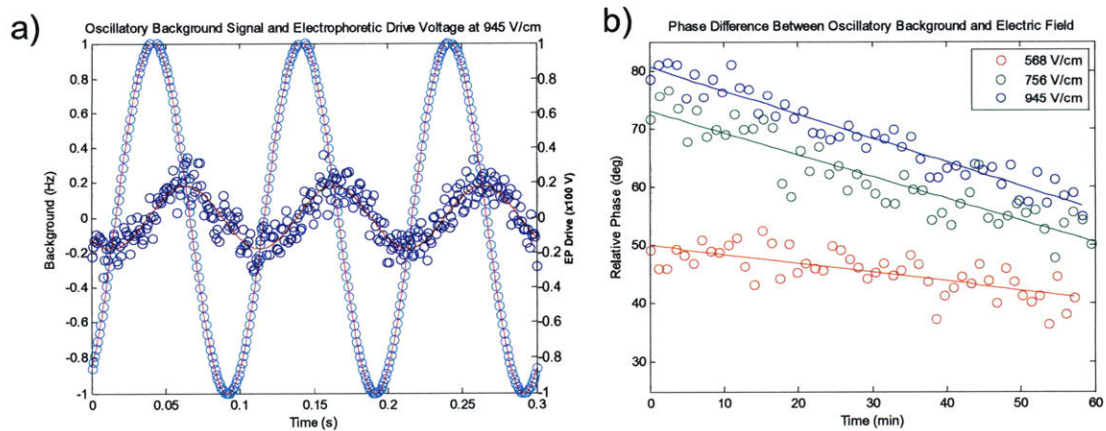


Figure 4-8: For an OSMR of unknown oxide integrity filled with 14 mM PBS, the phase of the oscillatory background signal was compared to that of the electrophoretic drive voltage for increasing drive voltage amplitudes. (a) The two signals are shown at a channel electric field amplitude of 945 V/cm. (b) The initial phase difference and rate of change in phase both increase with electric field amplitude (see Table 2)

<i>Electric Field (V/cm)</i>	<i>Initial Phase Difference (deg)</i>	<i>Rate of Phase Change (deg/hr)</i>
568	49.9	-9.3
756	72.9	-22.5
945	80.6	-24.7

Table 4.2: Linear regression of the data in Fig. 4-8B produced the following values for initial phase differences and time rate of change of the relative phase.

4.5.2 OLSMR

Because the OLSMR was designed to measure EPM of mammalian cells under physiological conditions, the dependence of its oscillatory background signal on electric field strength was characterized only in 140 mM PBS (Fig. 4-9). Otherwise, the characterization followed the one described previously for the OSMR. The background signal for the OLSMR when filled with 140 mM PBS is found to be similar to that of the OSMR under these conditions in that it contained both 10-Hz and 20-Hz components at all electric field strengths. However, the two responses differed both in magnitude and their functional relationship to electric field strength. At an electric field of only 65 V/cm, the amplitude for the OLSMR is comparable to that of the OSMR at an electric field of 585 V/cm (compare Figs. 4-9B and 4-5C). Also, when an 8th order polynomial was fit to the amplitude versus electric field strength data for the OLSMR, it was found to have an exponent of 1.98 ± 0.08 over the range of electric fields measured. Hence the

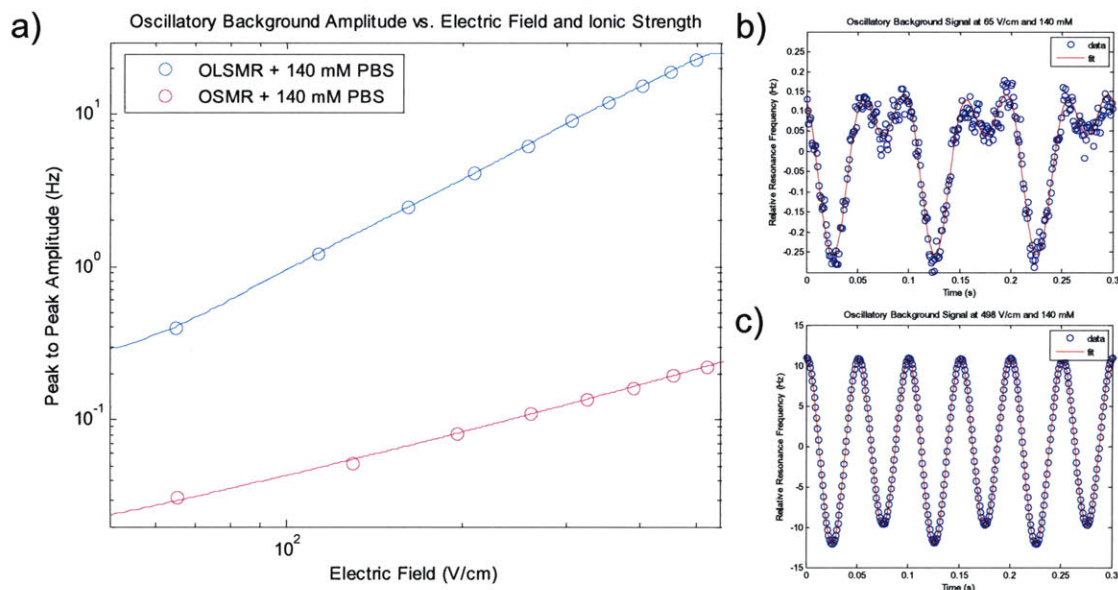


Figure 4-9: (a) Comparison of the dependence of the peak-to-peak amplitude of the oscillatory background signal on peak amplitude of a 10-Hz sinusoidal electric field at a buffer ionic strength of 140 mM is measured (open circles) and fit to a polynomial (lines). Fitting of the frequency time course data at an electric field strength of 65 V/cm (b) and 498 V/cm (c).

OLSMR's background amplitude can be considered to vary quadratically with electric field strength at 140 mM whereas it varies linearly for the OSMR at this ionic strength.

4.6 Differentiation of Polystyrene Microspheres by Mass and Surface Charge

4.6.1 Material Preparation

Dyed polystyrene microspheres suspended in de-ionized water having nominal diameters of 2.20 μm and 1.96 μm obtained from Thermo Fisher Scientific Inc. (Waltham, MA)

and Corpuscular Inc. (Cold Spring, NY) respectively were re-suspended together in 14 mM phosphate-buffered saline, pH 7.8, to concentrations of $6.8 \times 10^6 \text{ mL}^{-1}$ and $2.5 \times 10^7 \text{ mL}^{-1}$ respectively. These concentrations were chosen to compensate for the higher nonspecific binding of the second microsphere type to the silicon oxide surfaces of the device channel walls in order to produce approximate parity in the number of transits for the two microsphere types.

4.6.2 Microsphere Mass and Charge Measurement

In one experiment using the protocol described in Section 3.3, 51 microsphere transits were observed over the course of twenty minutes and the resulting data were analyzed to determine their spatial amplitudes and buoyant masses. These spatial amplitude data, together with the estimates of electric field and wall zeta potential described in Sections 4.2 and 3.2 respectively, were used to compute the zeta potentials of each microsphere according to Equations 2.11 and 2.12, and the resulting histogram is shown in Figure 4-10A. To validate these measurements, suspensions of the same microspheres were measured using two commercial PALS-based zeta potential instruments, the Brookhaven Instruments ZetaPALS and the Malvern Zetasizer Nano ZS90 (Fig. 4-10B). Microspheres were measured at the same concentrations and under the same buffer conditions as with the SMR, the only difference being that the two microsphere types were measured separately on the commercial instruments while they were measured as a mixture using the SMR. For the Brookhaven instrument, the data reported for each

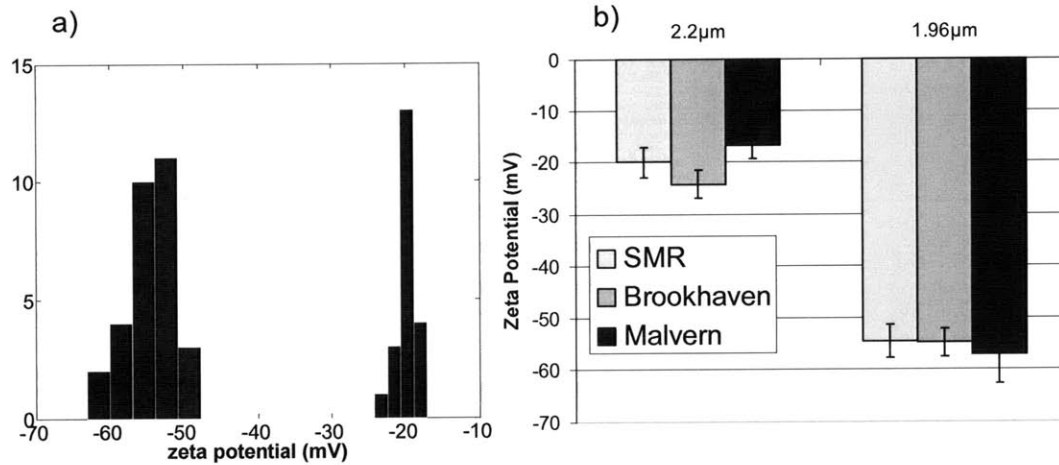


Figure 4-10: (a) Histogram of 51 single-particle zeta potential measurements made on a mixture of 2.20 μm and 1.96 μm polystyrene microspheres using the SMR. (b) Mean zeta potentials measured for the two microsphere types using the SMR and two commercial instruments.

microsphere type represent the average and standard deviation of three consecutive runs, each of which comprises ten PALS measurements. The corresponding data for the Malvern instrument are the result of five runs of fifteen measurements. The error for the SMR measurement reflects the estimated instrument uncertainty, taking into account the standard deviations of the spatial amplitude time courses and the wall zeta potential measurements. In a separate experiment conducted on a different day, 101 microspheres were analyzed, and the difference in mean zeta potentials for the two microsphere types was found to be the same within the instrument uncertainty.

Using Equation 2.13, microsphere surface charge is estimated from the measured zeta potential and size for each microsphere. Although both the size and mass of each microsphere are known, the mass is a more effective parameter for differentiation since it varies as the cube of the size and hence has greater resolution. Plotting the absolute

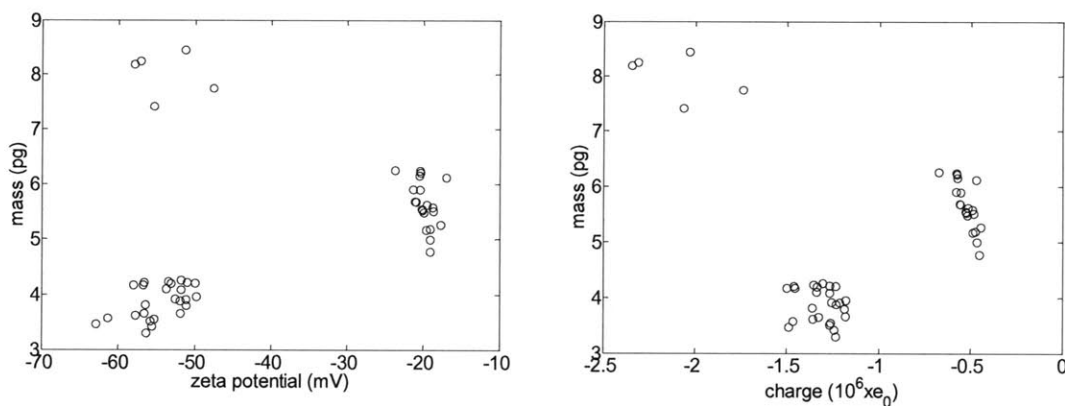


Figure 4-11: Scatter plot of the absolute mass of 51 particles from a mixture of 2.20 μm and 1.96 μm polystyrene particles vs (a) their zeta potential and (b) their electrokinetic surface charge, as computed by Eq. 13.

masses of individual microspheres against their measured zeta potential or charge, as shown in Figure 4-11, reveals additional information about the population. Both scatter plots reveal two sub-populations of the more negative of the two microsphere types which is not evident in the zeta potential data alone. We interpret these to be monomers and dimers of this microsphere type since one sub-population has a mean mass which is roughly double that of the other one at the same zeta potential. The observation that this type of microsphere tends to aggregate more than the other type in the mixture is supported qualitatively by the observation that these microspheres exhibited higher non-specific binding to the channel walls. The mass-charge scatter plot illustrates how these sub-populations are more readily differentiated on the basis of charge. This feature results from the fact that the more massive dimer microspheres also possess a larger net charge, which is consistent with their larger surface area. Although in the case of our two chosen microsphere types there are three distinct sub-populations in the mass data alone, the potential for overlap in this dimension is evident. For example, if the mean mass for the more neutral of the two microsphere types had been roughly double that of the more

negative type, it would have obscured the dimer sub-population for that type. It is therefore expected that integrated measurement of both the surface charge and mass distributions will provide advantages in the differentiation of complex microsphere mixtures.

4.6.3 Signal to Noise Ratio and Throughput

The SNR of the mobility measurement technique described here is inherently dependent on the mass of the particle being measured. This can be seen from Equation 2.14 in that a larger mobility signal, as measured by the total rate of change of the resonance frequency, can be obtained either by increasing the first term in the expansion, which is proportional to particle mass, or the second term, which is proportional to the particle's relative mobility. The uncertainty in position for microspheres of the type examined here, computed as the length of the cantilever divided by the SNR of the net frequency shift, is approximately 2 μm . Since these microspheres have typical spatial oscillation amplitudes of 10 μm , the SNR for the spatial amplitude is on the order of 5. This is the limiting source of error in the measurement of mobility for microspheres since the SNR for the electro-osmotic mobility measurement is an order of magnitude larger. Because mass is proportional to the cube of diameter, the SNR for the mobility measurement falls off rapidly for smaller microspheres if all other parameters are held constant. Furthermore, the system is physically limited by the small dimension of the suspended microchannel, which is 3 μm in the present device. As the size of particles approaches

this value, it is expected that interactions with the channel walls will begin to dominate their trajectory through the sensor, preventing accurate mobility quantitation. On the other hand, the SNR of both mass and mobility improve if particles of greater density are examined.

The throughput of the technique is currently limited by the algorithm used to extract the mobility from the raw data. The curve fit to the oscillatory background signal requires a window of one second just prior to a particle transit during which no particles are present inside the sensor. As a result, particle concentrations were kept low so that this analysis could be performed in an automated fashion without errors. Elimination of this background signal could theoretically increase the particle throughput to its current SNR-limited value of 1 Hz. Another limitation on throughput results from the settling of particles. A certain amount of time is needed to adjust the system to achieve a flow rate through the device suitable for mobility measurement. During this time, the concentration of microspheres in the reservoirs falls considerably due to settling, sometimes reducing the throughput of microspheres below the desired level.

Chapter 5

Characterization of Bacteria by Buoyant Mass and Electrophoretic Mobility

5.1 Introduction

Bacterial biofilms, layers of bacterial cells attached to solid surfaces and embedded in a biologically-formed organic matrix, [57] are ubiquitous in nature and have important consequences for human health [21-23], the environment, [24-26] and a variety of industries. [27-29] Measurement of bacterial EPM has been an important tool in the development of theoretical descriptions of the initial adhesion kinetics of biofilm formation. [19, 20] One approach to this problem is to model the dependence of cellular EPM on ionic strength in order to extract physical parameters describing cell surface electrokinetic properties from experimental data. In one such theory proposed by Ohshima, the bacterial cell is modeled as a hard sphere surrounded by a thin fluid-permeable polyelectrolyte layer. [58, 59] The particle's electrophoretic mobility is described by two parameters: the fixed charge density of the polyelectrolyte and the

“electrophoretic softness”, which is a measure of the hydrodynamic permeability of the polyelectrolyte layer. This model was applied by de Kerchove and Elimelech to experimental EPM data obtained by light scattering experiments performed on *Escherichia Coli* K12 bacteria, and the extracted parameters were used to predict bacterial deposition onto a quartz surface using Derjaguin-Landau-Verwey-Overbeek (DLVO) theory. [60] The failure of the combined soft particle electrophoresis and DLVO models to explain the low attachment efficiencies of these bacteria was attributed to the lack of provisions in Ohshima’s theory for physical and chemical heterogeneity within the polyelectrolyte layer. Although some of these provisions, such as a provision for radial variation in the charge density and electrophoretic softness of the polyelectrolyte layer, have been added in more recent theories, they have not yet been successfully applied to experimental bacterial adhesion data. [61] Another potential oversight of this approach is that it neglects variations in cell surface electrokinetic properties between cells in a population. It is well known that when EPM is measured at the single cell level, distributions with standard deviations comparable to their mean values are common. [43] This heterogeneity is ignored in most studies, where the reported variation in EPM is computed from several repeated population average measurements, and could be responsible for discrepancies when the data are compared to continuum models. For example, in some highly heterogeneous populations, minority subpopulations which are responsible for most of the observed binding may not be significant in determining the mean EPM of the overall population. Therefore statistical models of cellular adhesion kinetics, coupled with single-cell EPM measurements could potentially yield better agreement between theory and experiment than continuum

approaches. This is one motivation for the development of robust, inexpensive and quantitative tools for single-cell bacterial EPM measurement. This chapter presents an alternative to the most commonly used techniques for single-cell EPM measurement which are based on direct microscopic observation and computational image analysis. [47, 46, 48] The SMR-based technique has been demonstrated by measuring EPM distributions of *Escherichia Coli* bacteria from single-cell measurements.

The integration of single-cell EPM and buoyant mass measurements may also be advantageous in understanding the mechanisms underlying the action of antimicrobial peptides on the outer membranes of bacterial cells. These short peptides are an important component of the innate immune response because of their ability to discriminate between bacterial and host cell membranes, a feature which makes them interesting templates in the design of antibiotic drugs. [62] One promising antimicrobial peptide which has been studied considerably is cecropin A, a linear 37-residue peptide which can form α -helices in partially organic solvent. [63-65] Although the exact mechanism of bactericidal activity is not understood, cecropins are known to bind to negatively charged membrane lipids and form a closely packed “carpet” of peptide. [66, 67] They assume a transbilayer orientation in membranes and form partially selective ion channels. [68, 69] Studies of the action of cecropin A on lipid vesicles [70] demonstrated that at high lipid to peptide ratios (L:P), ion channels formed by cecropin A were successful in depolarizing the vesicle membrane but not in releasing calcein molecules from vesicles. At lower L:P, complete leakage of calcein from the vesicles was observed, and observed changes in membrane potential were consistent with lysis. These data suggest that the

size of pores created by cecropin A are concentration-dependent, with small ion-permeable channels being formed at low concentrations and larger channels permeable to macromolecules resulting from higher concentrations. In the same study, measurements of the bactericidal activity of different cecropin A concentrations on *E. coli* K12 were then compared with parallel permeability measurements on *E. coli* ML35 for a ten minute peptide incubation. This comparison showed that killing of the K12 strain occurred at concentrations too low to release cytoplasmic β -galactosidase from the ML35 strain. Taken together, these findings indicate that the mechanism of bactericidal activity is due to the dissipation of transmembrane electrochemical ion gradients rather than leakage of cytoplasmic contents. A later study extended this concept beyond the single incubation time point for a similar peptide, cecropin P1, and *E. Coli* ML35. [71] This study quantified the dependence of both bactericidal activity and membrane permeability on time and peptide concentration. At the minimum inhibitory concentration (MIC) for this system, it was found that the kinetics of membrane permeabilization and bactericidal activity correlated well, both taking place on a time scale of 30 minutes. However, since maximum permeability was also achieved below the MIC, it was concluded that the level of immediate permeability, rather than the time to reach maximum permeability, is the key determinant of bactericidal activity, a finding which is in agreement with a membrane depolarization killing mechanism.

The ability to simultaneously measure the buoyant mass and EPM of bacteria using the SMR could potentially provide a more complete picture of the effects of antimicrobial peptides. The buoyant mass of cells can be compared to their volume, as determined by

Coulter counting, to provide an estimate of cell density. Together, these quantities provide an unequivocal measure of the extent to which the contents of peptide-treated cells are able to escape through pores, whereas previous studies have relied on indirect metrics such as extracellular substrate hydrolysis by cytoplasmic enzymes or penetration of dye molecules through the membrane to quantify permeability. Although binding of cecropins to lipopolysaccharides (LPS) on the surface of *E. Coli* cells has been probed by displacement of Dansyl PMB, which fluoresces intensely when bound to LPS but only weakly in solution, these studies indicate that the rate of accumulation of cecropins is insensitive to changes in peptide concentration. This surprising result indicates that very small quantities of peptide on the membrane can cause enough membrane permeation to produce bactericidal activity. Measurement of cellular EPM, which is directly influenced by the accumulation of cationic peptides on the negatively-charged cell membrane, provides an interesting alternative means by which to test this finding. Integrated measurement of buoyant mass and EPM at the single-cell level provides a unique opportunity to correlate cell permeation with LPS-peptide binding without the obscuring effects of population heterogeneity. Furthermore, direct comparison of bacterial EPM with volume, density, permeability and viability for a range of peptide doses may reveal relationships between physical changes in the membrane and bactericidal peptide action which were not measurable by indirect methods.

5.2 Materials and Methods

To test for a correlation between changes in buoyant mass and EPM at the single-cell level, *E. Coli.* (ATCC #25922) were treated with a 15-residue peptide composed of the first seven amino acids of cecropin A and residues 2 to 9 of melittin, (designated CAM hereafter) and measured using the protocols described in Chapter 3. A peak electric field of 585 V/cm was used to measure EPM. To test for correlations between average cell buoyant mass, volume and density, separate experiments were conducted on a similar SMR apparatus without integrated electrophoresis capabilities (designated standalone SMR) and on a Coulter counter (Beckman-Coulter, Fullerton, CA). In order to relate these buoyant mass and volume measurements to changes in membrane permeability and bactericidal activity, cells from the standalone SMR experiments were also assayed using membrane permeability staining (BacLight™, Life Technologies, Carlsbad, CA) and incubated on LB-agar plates to determine viability.

5.2.1 Integrated Buoyant Mass and EPM

Simultaneous measurements of the buoyant mass and EPM of *E. Coli.* were carried out for cell suspensions which had been incubated with 100 µg/mL CAM for 30 minutes and control suspensions which were not treated with peptide. Because of the time needed to prepare the instrument for measurement, treated and untreated suspensions were typically measured on different days. The treated and untreated measurements were each carried

out three times, and the conditions for each iteration are summarized in Table 5.1. For the first iteration of the untreated measurement, cells were taken from LB-agar plates (L5542-10EA, Sigma-Aldrich, St. Louis, MO) stored at 4 °C and grown in liquid LB medium (L3152-1KG, Sigma-Aldrich) at 37 °C and 250 rpm for at least 12 hours. This saturated liquid culture was then diluted 100-fold into LB, grown for an additional two hours (mid-log phase), and 1.5 mL of culture was centrifuged (3000g, 3 minutes). The supernatant was removed, cells were washed once with 1.5 mL of 15 mM PBS with 0.2% D-glucose added, then re-suspended in 1.5 mL of the same buffer. This suspension was then diluted 17-fold into the same buffer and observed under a white-light microscope to check for contaminant species before running on the integrated SMR. For the first iteration of the treated measurement, cells from the saturated culture used to perform the first untreated measurement were diluted 100-fold into LB and incubated overnight twice. This two day old saturated culture was then used to make the first treated measurement. The protocol for the first treated measurement was the same as the first untreated measurement except that after the cells reached mid-log phase, 150 µL of 1 mg/mL CAM was added to 1350 µL of the cell suspension and incubated at room temperature for 30 minutes before washing and re-suspension. The second iteration followed the protocol used in the first iteration with three exceptions. Firstly, the endpoint in cell growth for both treated and untreated samples was determined by optical density rather than a fixed time period. Cells from a saturated culture were grown to an OD₆₀₀ of 1.5-1.7 before the incubation step. Secondly, CAM was pre-diluted into LB to a concentration of 200 µg/mL and this solution mixed 1:1 with mid-log phase cells rather than adding 1 mg/mL CAM stock directly to cells. Finally, the treated and untreated experiments were

performed only one day apart instead of two days apart, so that only one additional overnight incubation of the saturated culture was needed between treated and untreated measurements. The third iteration followed the protocol used in the second with the only exception being that both untreated and treated measurements were made in the same day, so that no overnight incubations were needed between measurements.

<i>Iteration #</i>	<i>Growth Endpoint</i>	<i>Passages Between Treated & Untreated</i>	<i>Volume Ratio of CAM:Cells</i>
1	2 h	2	1:9
2	OD ₆₀₀ = 1.5	1	1:1
3	OD ₆₀₀ = 1.7	0	1:1

Table 5.1: Differences in the protocol for integrated buoyant mass and EPM measurements between three iterations of the experiment.

5.2.2 Standalone Buoyant Mass and Volume

Six colonies were picked from a refrigerated LB-agar plate (4 °C) and incubated separately in LB (37 °C, 250 rpm) for at least 12 hours. All cultures were then diluted 100-fold in LB and incubated until they reach an OD₆₀₀ of 1.2-1.3. A 1000-fold dilution of each culture was measured on a Coulter counter to determine its cell concentration and volume distribution, and it was observed under a white-light microscope. Individual cultures were scored qualitatively by volume distribution, growth rate and motility to determine which was most phenotypically similar to cultures used in previous measurements. This culture was then diluted to 2×10^8 cells/mL by adding a volume of LB determined by the measured Coulter density. This suspension was diluted 1:1 into

LB containing CAM at concentrations of 0, 20, 30, 40, 50 and 200 $\mu\text{g/mL}$. All samples had a total volume of 4.5 mL. After incubating for 30 minutes at 25 $^{\circ}\text{C}$, each suspension was centrifuged (3000g, 3 minutes), washed twice with 4.5 mL of PBS, then re-suspended in 1.5 mL of PBS and refrigerated at 4 $^{\circ}\text{C}$. These samples were the stock for the standalone SMR buoyant mass, volume, permeability and viability assays. Immediately following refrigeration, a 1000-fold dilution of each stock sample was measured on a Coulter counter to determine its volume distribution and cell density. Following one hour of refrigeration, the first stock sample was diluted to between 5×10^7 and 7.5×10^7 CFU/mL and run on the standalone SMR to determine its buoyant mass distribution. This procedure was then repeated for each of the remaining stock samples. The entire protocol was carried out twice on different days. For the first iteration, the untreated suspension was measured first, then the treated suspensions were measured in order of decreasing peptide concentration, followed by a second measurement of the untreated suspension. For the second iteration, the order of measurement was as follows: untreated, 100 $\mu\text{g/mL}$, 25 $\mu\text{g/mL}$, 20 $\mu\text{g/mL}$, 15 $\mu\text{g/mL}$, 10 $\mu\text{g/mL}$, untreated, 100 $\mu\text{g/mL}$.

5.2.3 Membrane Permeability

Cell permeability is measured using the BacLightTM membrane permeability staining kit (Life Technologies, Carlsbad, CA), which quantifies the percentage of permeabilized cells by measuring the integrated fluorescence ratio of the live stain SYTO9 and the dead

stain Propidium Iodide. SYTO9 is able to penetrate all cells, and fluoresces with a peak emission wavelength of 530 nm when it intercalates DNA. Propidium Iodide penetrates only cells with permeabilized membranes, and its association with DNA causes an increase in its own fluorescence, which has a peak emission wavelength of 630 nm, while quenching the fluorescence of SYTO9. Therefore the ratio of green to red fluorescence decreases as the fraction of permeabilized cells increases. Stock samples were diluted to 2×10^8 CFU/mL by adding a volume of PBS determined by the measured Coulter density (see Section 5.2.2). A stock solution of dye is prepared by adding 6 μ L of each dye (3.34 mM SYTO9 and 20 mM Propidium Iodide, both in DMSO) to 2 mL of de-ionized water. After adding 100 μ L of each of the diluted stock samples to three wells in a clear, flat-bottomed 96-well plate (Nunc Maxisorp Thermo Fisher Scientific, Waltham, MA), 100 μ L of the dye stock solution was added to each of these wells. Following a 15 minute incubation period, the plate was loaded onto a Varioskan Flash fluorescence microplate reader (Thermo Fisher Scientific, Waltham, MA) which measures SYTO9 fluorescence in a 12nm bandwidth centered at 530 nm and Propidium Iodide fluorescence in the same bandwidth centered at 630 nm. The untreated sample was considered to be composed entirely of cells with intact membranes while the sample treated at 100 μ g/mL was considered to be entirely composed of permeabilized cells, so integrated fluorescence ratios of these two samples were assigned permeabilized fractions of 0 and 1, respectively. The permeabilized fractions for other samples were determined by interpolating their integrated fluorescence ratios between these two extremes.

5.2.4 Bactericidal Activity

Stock samples were diluted to 2×10^3 CFU/mL by adding a volume of PBS determined by the measured Coulter density (see Section 5.2.2). One hundred microliters of the diluted stock was dispensed in triplicate on LB-agar plates and incubated for six hours at 37 °C. Viability percentages for each of the peptide-treated samples was determined by manual counting colonies on each of the plates with peptide-treated samples with the aid of a stereo microscope and dividing by the number counted on the plate containing untreated cells.

5.3 Results and Discussion

5.3.1 Integrated Buoyant Mass and EPM

The buoyant mass of individual cells is plotted versus their EPM for the three iterations of this experiment in Figure 5-1, which also shows the corresponding buoyant mass and EPM histograms. A significant decrease in mean buoyant mass between the treated and untreated cell suspensions was observed in all three iterations ($40 \pm 19\%$, with an average p-value of 8×10^{-4}). Although there was an apparent decrease in EPM due to peptide treatment in the first iteration, this is not believed to be significant because of the relatively low channel wall zeta potential (-53.3 mV for the first iteration, compared to

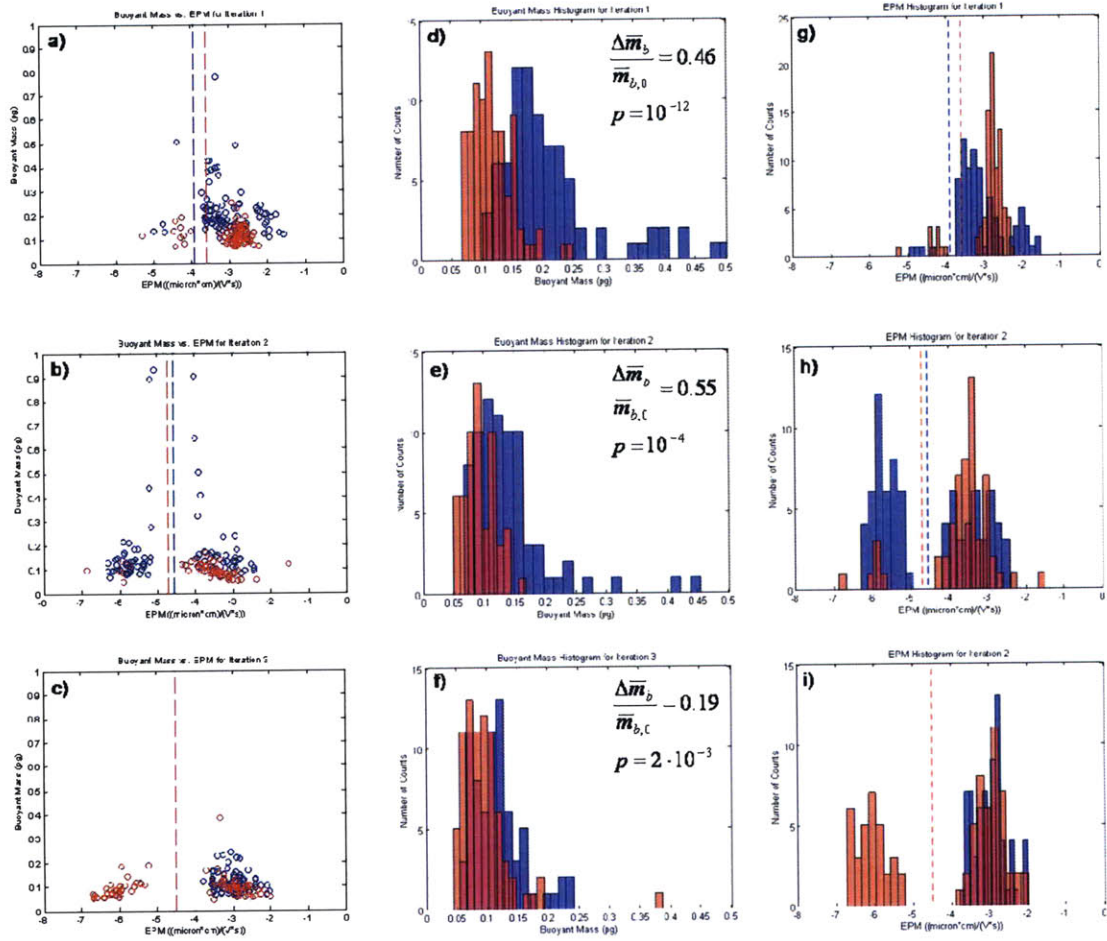


Figure 5-1: Summary of integrated measurements of the buoyant mass and EPM of *E. Coli* (blue data) and *E. Coli* treated with 100μg/mL CAM (red data). (a-c) Scatter plots of buoyant mass vs. EPM for three iterations of the experiment, with corresponding histograms of buoyant mass (d-f) and EPM (g-h). In the mass histograms, $m_{b,0}$ refers to the untreated dataset. Dashed lines indicate electro-osmotic mobility of the channel wall. The uncertainty in EPM for a typical cell is $\sim 0.21 \mu\text{m}\cdot\text{cm}\cdot\text{V}^{-1}\text{s}^{-1}$.

-65.6 mV and -63.7 mV for the second and third iterations, respectively). As a result, many data corresponding to cells with an EPM similar to that of the channel wall exhibited a SNR of less than one, and had to be discarded. In addition, the first treated measurement was made on cells which had been in liquid culture for a total of three days, and they were treated by adding concentrated peptide directly to a cell suspension whose concentration was not exactly known, practices which were corrected for the second and third iterations of this measurement. Hence the data for the first iteration are biased and

should be interpreted with caution. Some interpretation of the EPM data for the last two iterations was also needed. When the signal processing algorithm was applied to some data from these experiments, it produced spatial amplitudes which were similar in magnitude to those of previously measured cells but opposite in sign. It is believed that this was caused by phase lag between the oscillatory background signal and the electric field in the channel after the device had been exposed to the electric field for long periods of time, a phenomenon which was studied in detail and is described in Section 4.5. Because means for measuring both phases did not exist at the time of these integrated measurements, the true spatial amplitudes for these cells cannot be computed. However, the similarity in magnitude between the positive and negative subsets of the spatial amplitude distribution (average p-value = 0.6), and the absence of a phase lag between the numerator and denominator time courses in the spatial amplitude computation are both consistent with an abrupt 180° shift in relative phase. Figure 5-2 shows how the results for the second and third iterations change when the signs of the negative spatial amplitude data are reversed. In this case, no significant change in EPM can be attributed to peptide treatment in either the second or third iterations ($p = 0.5, 0.3$ respectively).

A similar phase-related error was observed in another experiment in which the measured suspension was contaminated with a suspected *Staphylococcus Aureus*. The species of the contaminant was determined by catalase test and visual comparison with cultured *S. Epidermidis*. In this experiment, EPM data were collected at three different electric field strengths for 30 minutes each (Fig. 5-3). While nearly all of the computed spatial amplitudes were negative at the lower two electric field strengths, a significant number

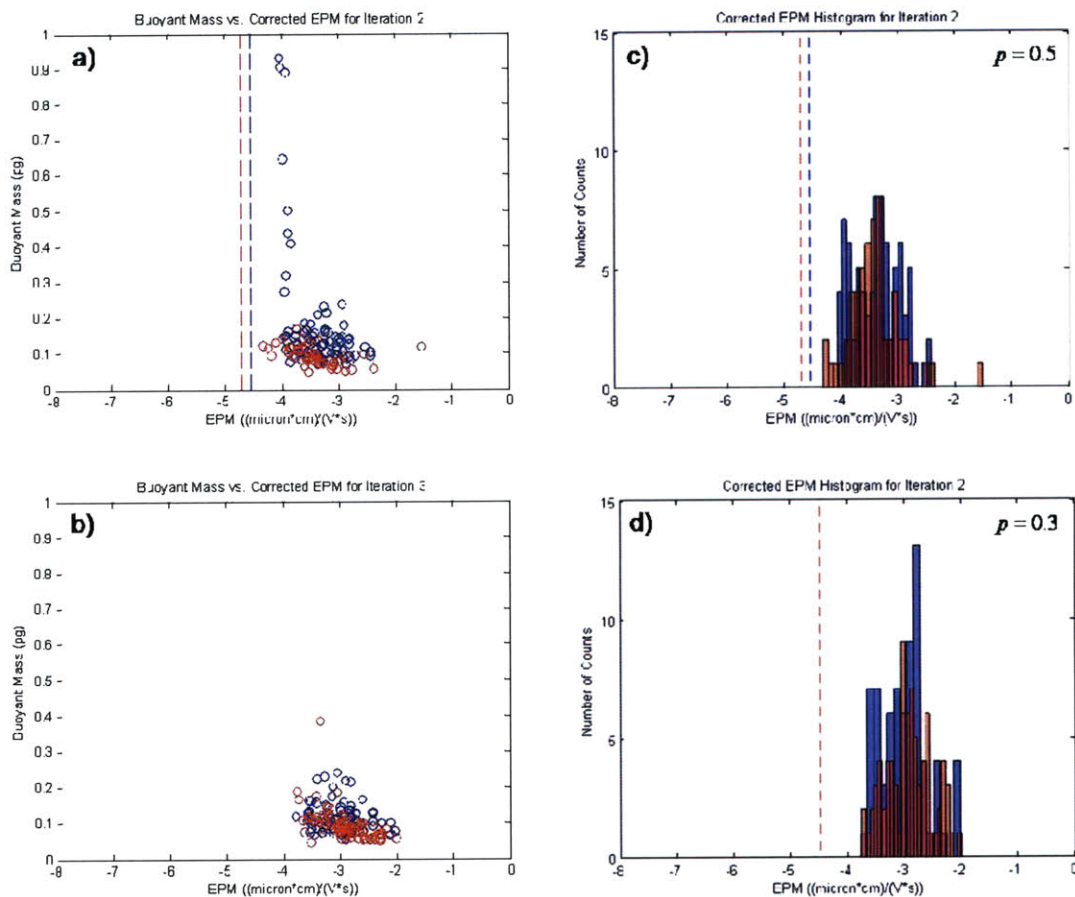


Figure 5-2: Integrated measurements of the buoyant mass and EPM of *E. Coli* (blue data) and *E. Coli* treated with 100 μg/mL CAM (red data) after reversing the signs of negative spatial amplitudes. (a-b) Scatter plots of buoyant mass vs. EPM for second and third iterations of the experiment, with corresponding histograms of EPM (d-e).

were found to be positive at the highest field strength. As with the *E. Coli* measurements presented in this section, the magnitudes of the positive and negative subsets of the spatial amplitude distribution did not have significantly different means ($p = 0.4$).

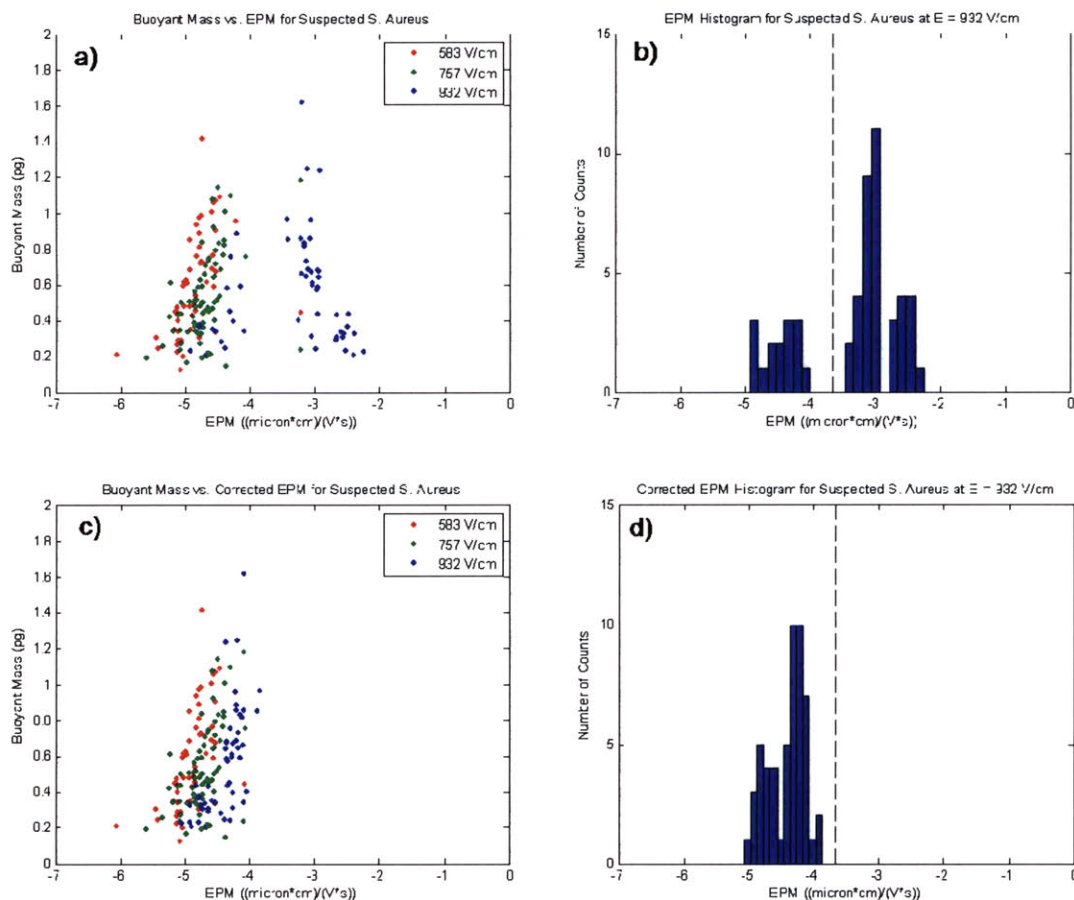


Figure 5-3: Integrated measurements of the buoyant mass and EPM of a suspected *S. Aureus* made at increasing electric field strengths. (a) Scatter plot of buoyant mass vs. EPM and (b) EPM distribution of the 932 V/cm measurement before correction. (c-d) The same data after reversing the signs of negative spatial amplitudes.

5.3.2 Standalone Buoyant Mass and Volume

Histograms of the buoyant mass and cell volume for each of the peptide concentrations are shown for each of the two iterations of the experiment in Figure 5-4. Since log-normal fits to most of these distributions gave poor results, it was assumed that they are

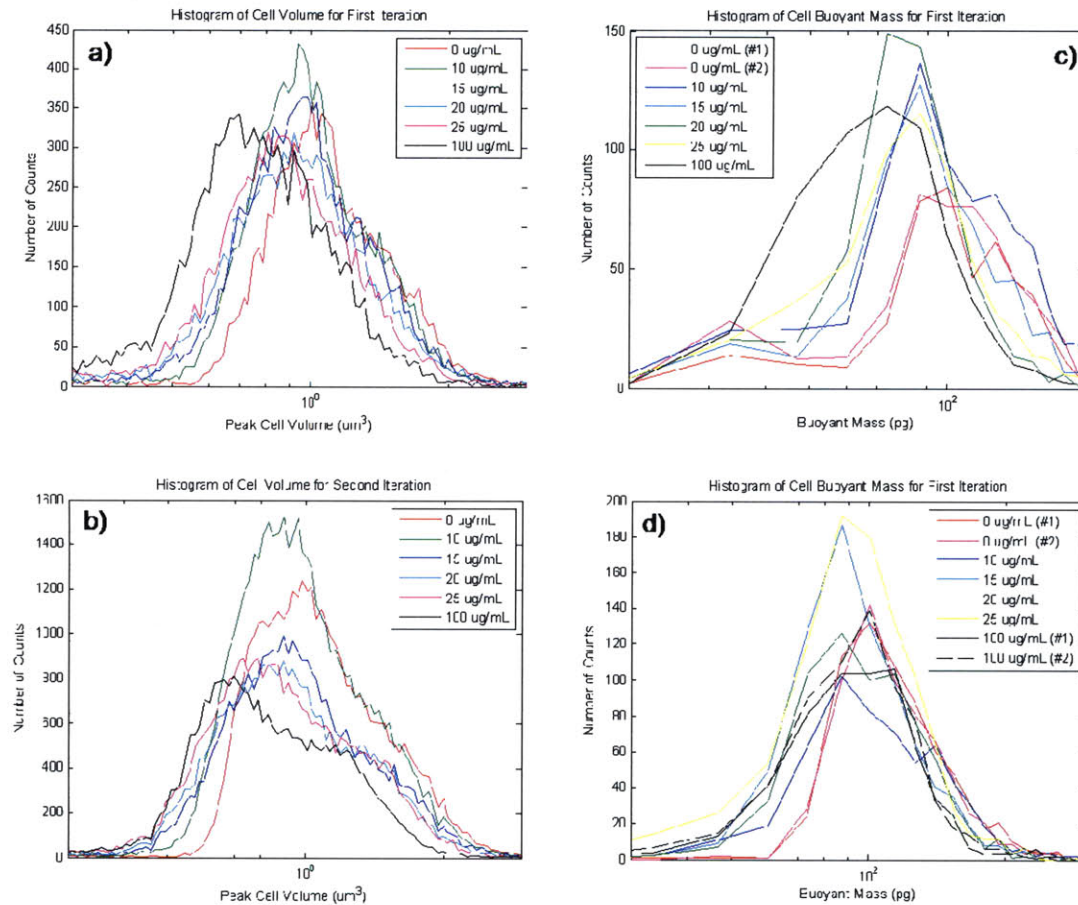


Figure 5-4: Measurements of the volume of *E. Coli*, made on a Coulter counter (a) and its buoyant mass, made on the standalone SMR (c), for different peptide doses. The same measurements were repeated on a different occasion (b,d).

multi-modal, suggesting that the peptide is size-selective in its action on cells. Consequently, mean values, rather than peak values from the log-normal fits, were used to construct the dose responses shown in Figure 5-5. Although both iterations showed a net trend toward smaller buoyant mass and volume with increasing peptide dose, the overall shifts at the highest dose were smaller in the second iteration compared with the first. The net shifts in relative buoyant mass for the two iterations were 30% and 16%, respectively, while the net shifts in relative volume were 28% and 21%. In addition, while the total shift in buoyant mass for the first iteration was smaller than the

corresponding shift in volume, this situation was reversed in the second iteration. Simple division of the net relative buoyant mass shift by the net relative volume shift results in a population-averaged decrease in relative density of 3% for the first iteration, and an increase of 7% for the second iteration. Hence there is no consistent change in density observed due to the action of the peptide.

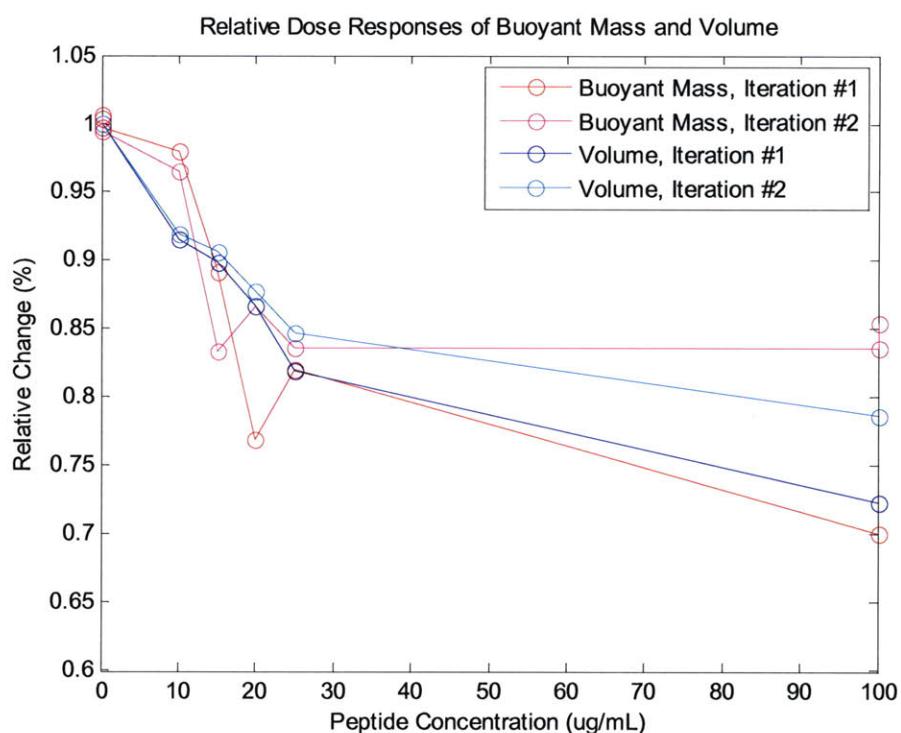


Figure 5-5: Relative dose responses of buoyant mass and volume determined from the mean values of the distributions shown in Fig. 25. The net shifts in relative buoyant mass for the two iterations were 30% and 16%, respectively, while the net shifts in relative volume were 28% and 21%.

5.3.3 Membrane Permeability and Bactericidal Activity

The membrane permeability staining assay produced similar results for both iterations of the experiment, as seen in Figure 5-6, where the fraction of intact cells (the complement of the permeabilized fraction) is plotted versus peptide concentration. A monotonic decrease in the percentage of intact cells is observed in both iterations, with doses of 17 $\mu\text{g/mL}$ and 12 $\mu\text{g/mL}$ corresponding to a 50% permeabilized population for the first and second iterations, respectively. The viability data, which were collected only for the second iteration of the experiment, are also in good agreement with the permeability data from this iteration with an estimated dose of 14 $\mu\text{g/mL}$ killing half of the population. The higher variability in colony counts for the 15 $\mu\text{g/mL}$ and 20 $\mu\text{g/mL}$ samples suggests possible over-counting due to the presence of satellite colonies on these plates.

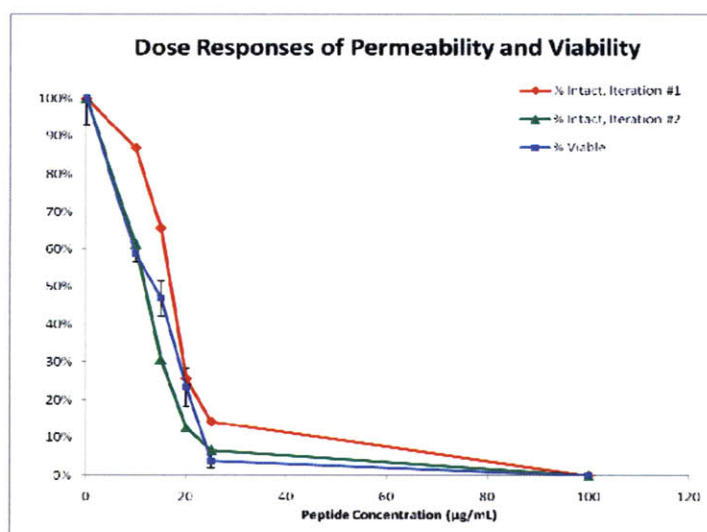


Figure 5-6: Dose responses of cell membrane permeability, determined using SYTO9/Propidium Iodide staining on two separate occasions, and cell viability, determined for the same cells used in the second permeability assay. The suspension was found to be 50% permeable at peptide concentrations of 17 and 12 $\mu\text{g/mL}$, and 50% viable at 14 $\mu\text{g/mL}$.

5.3.4 Discussion

Viability and permeability assays were performed on the same cell suspensions used in the standalone buoyant mass and volume measurements, and monotonic decreases in mass and volume were observed over the same range of peptide doses as both permeabilization and killing. This suggests that after a 30-minute incubation with the peptide, cells both shrink and leak cytoplasmic macromolecules in a dose-dependent manner. Comparison of the standalone buoyant mass and volume data further suggests that shrinkage and leakage are similar in magnitude, so that cell density is maintained constant. However, it is also possible that permeabilized cells possess a smaller electrical resistance than intact cells of the same volume, so that the shift in current measured by a Coulter counter for the transit of a permeabilized cell is consistent with a completely intact cell having a much smaller volume. In order to resolve this ambiguity, more detailed structural characterization of pores formed by CAM in membranes is needed. This, combined with knowledge of the size distribution and number of pores at a given peptide dose will make it possible to model the electrical properties of cells under these conditions, and hence predict the change in apparent volume measured by a Coulter counter.

Buoyant mass shifts observed in the integrated SMR measurements were consistent with the corresponding shifts observed in the standalone SMR. Hence it is reasonable to expect similar degrees of viability and permeability in the suspensions from the integrated measurements, even though these assays were not performed directly on the

same cells. The EPM distributions from the untreated measurement span ranges of EPM which are comparable to values reported in the literature that were made under similar conditions of ionic strength and pH, but such examples are rare because of the scarcity of robust single-cell EPM measurement techniques. [43] Examples of population averaged EPM measurements are much more common in the literature, but comparison is made difficult by the fact that the mean EPM, in addition to being sensitive to ionic strength and pH, is known to vary significantly with medium nutritional components, growth phase and centrifugation conditions. [60, 72-75] While a significant shift in the mean EPM was not observed between the untreated cell suspension and the one treated at a peptide dose of 100 $\mu\text{g/L}$, the viability assay determined that this dose was sufficient to prevent recovery of the culture on LB-agar. Hence the surface density of peptide needed to prevent recovery of the suspension is below the resolution of this EPM measurement technique. This result is in qualitative agreement with a prior study, which showed no change in Dansyl PMB displacement after incubation of *E. Coli* for 30 minutes with cecropin CP1 at twice the MIC. [71] However, more sensitive methods are needed to make a quantitative assessment of the dose dependence of peptide surface density.

Chapter 6

Integrated Preconcentration and Sensing of Protein Biomarkers

6.1 Introduction

Despite great technological advances which have been made in the field of quantitative proteomics, there are still very few molecular biomarkers used for clinical diagnosis of disease. One reason for this is that protein biomarkers must be present in biofluids which are readily available in clinical settings, such as blood or urine, in order to be practical. In some cases, known biomarkers exist in such small quantities in these fluids that they are not detectable by conventional clinical diagnostic methods, which motivates the development of new methods with higher sensitivity. [76] Another reason that some newly discovered biomarkers are not able to enter mainstream clinical use is the need for sensitive and specific probes. Most diagnostic assays for protein biomarkers rely on antibodies as probes, and engineering of antibodies which are both highly sensitive and highly specific for a given protein biomarker is made difficult by the fact

that antibodies are generally produced *in vivo*. In contrast, nucleic acid aptamer probes can be synthesized *in vitro* and systematically evolved to optimize their selectivity for a given protein biomarker target, but few examples exist of aptamer probes with sensitivity and selectivity both comparable to their monoclonal antibody counterparts. [77]

This thesis presents an instrument which takes advantage of the high selectivity of molecular probes while achieving a high sensitivity through preconcentration rather than probe affinity. This concept is illustrated schematically in Figure 6-1 for a conventional immunoassay. Detection of the protein biomarker in its native biofluid is often impractical because the detector is saturated by non-specific binding of highly concentrated background species (e.g. serum albumin in blood), making it necessary to perform separations on the sample to filter these species out. Filtration inevitably reduces the target concentration, which further increases the need for high probe affinity. However, the bound fraction of receptors in equilibrium is proportional to the product of the target and probe concentrations, so the response of a system with a low probe affinity

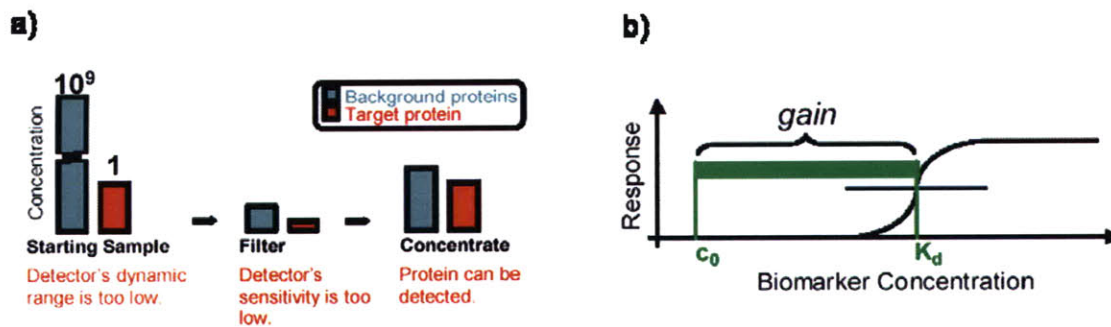


Figure 6-1: (a) In conventional immunoassays, sensing of low abundance proteins is made difficult by non-specific binding of background species. Filtration improves SNR, but also reduces signal, further increasing the system's required sensitivity. (b) For a given probe system, preconcentration of either the target or probe is the only way to improve assay sensitivity.

can be improved either by concentrating the target or the probe. Although techniques for probe preconcentration have been successfully demonstrated [78], integration of target preconcentration has been more elusive. This thesis demonstrates a microdevice which integrates non-selective protein biomarker preconcentration by means of a nanochannel filter with selective mass-based detection using an SMR whose suspended microchannel has been functionalized with capture molecules. This device is able to concentrate protein by up to 10^4 -fold in a volume of several picoliters in less than an hour in order to detect biomarkers using low-affinity probes at concentrations that previously could not be resolved. It is therefore expected that future assays based on this device will be able to sense a wider range of biomarkers than conventional immunoassays which are limited to targets for which high-affinity monoclonal antibodies can be produced.

6.1.1 Nanofluidic Concentrator

Recently, the Han group at MIT developed a device which uses a nanochannel filter to preconcentrate biomolecules by up to 10^4 -fold in less than an hour. [79, 80] The device, shown schematically in Figure 6-2, consists of two microfluidic channels with cross-sectional dimensions of $20\text{ }\mu\text{m} \times 1.5\text{ }\mu\text{m}$ which are connected by a series of 40 nm deep nanochannels. When these nanochannels are filled with media having an ionic strength on the order of 10 mM, the Debye length becomes comparable with the nanochannel depth, which gives the nanochannel perm-selective ion transport properties when a

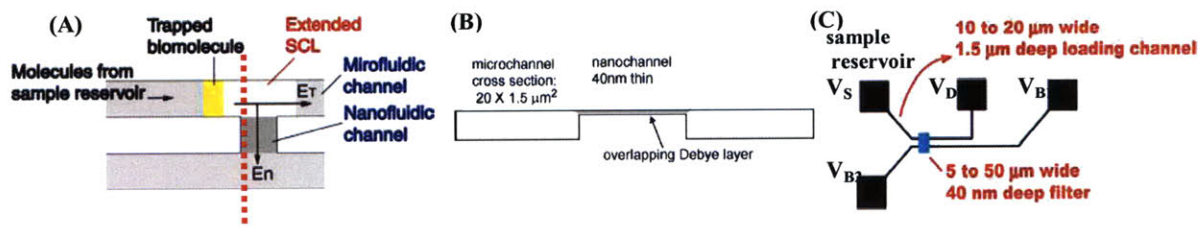


Figure 6-2: Schematic diagram of nanofluidic biomolecule concentrator (a) Top view. An electric field E_n is applied across the nanochannel, to create an extended space charge layer (SCL). The SCL will be an energy barrier for anionic biomolecules, and they will get trapped before the SCL. (b) Cross section diagram along the dotted line (c) Device layout and dimensions. By controlling the potentials (V_S , V_D , V_{B1} & V_{B2}), one can fully control the nanofluidic concentrator (trapping and release of the trapped

longitudinal electric field, E_n , is applied. For the example shown in Figure 6-3, these nanochannels have silicon dioxide surfaces bearing negative fixed surface charges at near-neutral pH, and hence positive counter-ions are transported more readily than negative co-ions. This results in depletion of counter-ions from the anodic end of the nanochannel and enrichment at the cathodic end. To maintain charge neutrality, co-ion concentrations mirror these changes in counter-ion concentration, producing a depletion

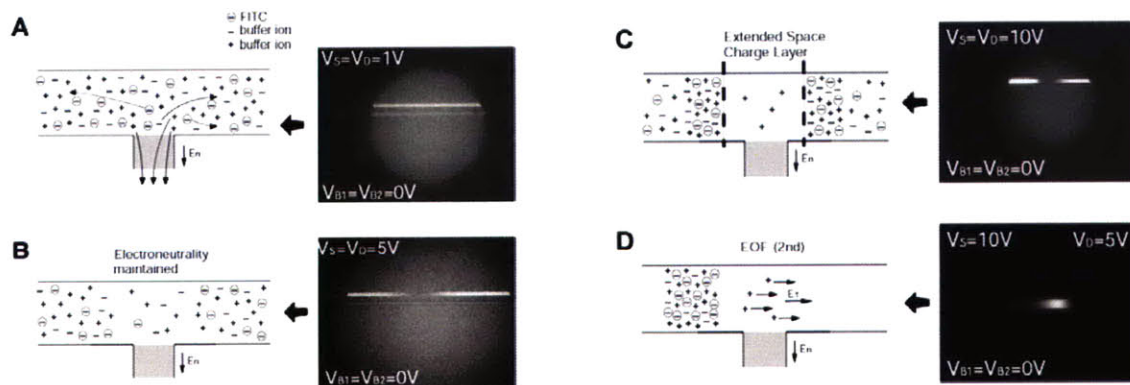


Figure 6-3: Mechanism of Nanofluidic Concentrator. (a,b) As the electric field applied across the nanochannel (E_n) increases, concentration polarization is achieved near the nanochannel. (c) When the E_n is further increased, an extended space charge layer is developed, and charged biomolecules are hindered from entering this region. (d) When another, tangential electric field is applied (E_t), this will bring biomolecules from the reservoir and trap them at the boundary. The fluorescent molecules in this case are FITC dye (negatively charged).

region of reduced ionic strength at the anodic end of the nanochannel, which is referred to as concentration polarization. [81] If E_n is increased further, a situation may arise where the diffusion of counter-ions from the bulk will not be sufficient to maintain charge neutrality in the depletion region, and an extended space-charge layer (SCL) will form at the anodic end of the nanochannel. This layer can be thought of as an extension of the Debye layer of the nanochannel itself, with mobile counter-ions in the SCL screening fixed charges present on the nanochannel walls. The concentration of counter-ions in the SCL, which is linearly dependent on the magnitude of E_n , gives rise to non-linear electrokinetic phenomena when a tangential electric field, E_t , is applied longitudinally to the microchannel at the anodic end of the nanochannel. This electro-osmotic flow of the second kind [82, 83], which is proportional to the product of E_n and E_t , is much stronger than electro-osmotic flow observed ordinarily in microchannels, which scales simply as E_t . [84-86] Macromolecules are rapidly transported through the anodic microchannel by this non-linear EOF, and molecules possessing fixed charges with their own associated Debye layers are repelled from the depletion region, because the low ionic strength of this region makes it energetically unfavorable. This balance between strong EOF of the second kind and repulsion from the depletion region results in preconcentration of macromolecules at the outer boundary of the depletion region.

The Nanofluidic Concentrator (NC) possesses several advantages over other biomolecular preconcentration techniques. Methods such as field-amplified sample stacking [87-90], isotachopheresis [91] and micellar electrokinetic sweeping [92-94] all have buffering requirements which can interfere with downstream sample processing,

making them difficult to integrate with detectors. Electrokinetic trapping techniques [95-97] show promise as an efficient way to concentrate proteins, but the linearity and stability of these methods is a concern. Chromatographic preconcentration techniques [98-101] capture proteins by the hydrophobic interaction, and hence are biased toward large hydrophobic proteins and less sensitive to smaller or more hydrophilic molecules. Membrane filter preconcentration [102, 103] is another example of a method which is biased toward larger molecules. Compared to these alternatives, the NC method of biomolecular preconcentration is the most favorable in terms of general applicability to a wide range of molecular species, ease of integration, and rate of preconcentration.

6.1.2 Integrated Device Concept

Several characteristics of the SMR make it a favorable candidate detector for integration with the NC. Firstly, the SMR is a highly effective immunoassay platform which has demonstrated sensitivity and selectivity comparable to established methods. Secondly, the surfaces of the suspended microchannel are silicon dioxide, and a wide variety of surface attachment chemistries have been developed for this material, which makes the SMR compatible with an equally large variety of probe systems. Most importantly, the internal volume of the SMR, which is approximately 25 pL, is comparable to the typical volume of the concentrated sample plugs which are produced in NC devices, so that detection can be accomplished without significant dilution of the concentrated sample. This feature, combined with the high surface area to volume ratio of the SMR, makes it

well suited to sensing the small numbers of molecules in a typical concentrated sample produced by the NC.

Two approaches were considered for integration of the SMR and NC. In the first approach, which is referred to as the type 1 integrated device and is illustrated in Figure 6-4, protein is preconcentrated in one region and then the concentrated sample plug is re-located to the SMR via pressure driven flow. The channel topologies were made as similar to the original standalone SMR and NC devices as possible. The main design difference between this integrated device and the standalone devices is that a connecting channel was introduced between the base of the SMR's suspended microchannel and the

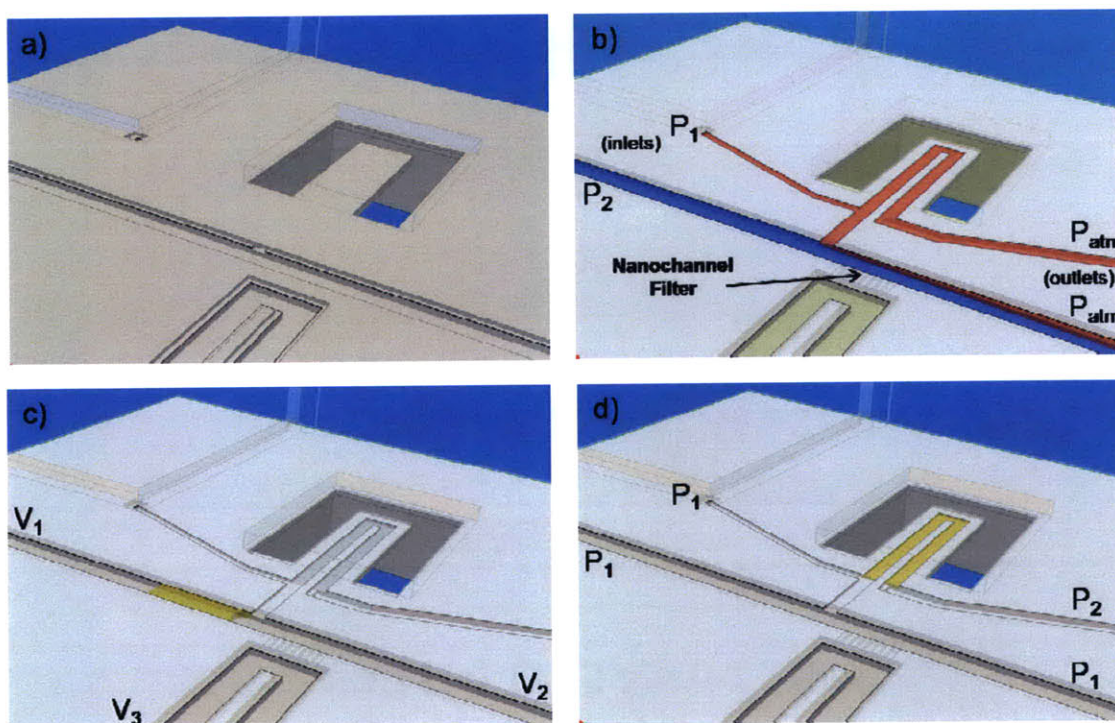


Figure 6-4: Type 1 integrated device concept, in which sample is first preconcentrated outside the SMR and then transferred to the SMR by pressure driven flow. (a) Overview of the device. (b) Cut-away view of the device with capping layer transparent. Site-specific functionalization (red) and passivation (blue) of the SMR and NC, respectively, is accomplished by controlling inlet pressures ($P_1 > P_2 > P_{atm}$). (c) With all pressures balanced, preconcentration is carried out by controlling channel voltages ($V_1 > V_2 > V_3$). (d) Following preconcentration, the sample plug is moved to the SMR by reducing P_2 relative to the rest of the device.

anodic microchannel of the NC to permit transfer of the concentrated sample. The cross-sectional dimensions of the anodic channel of the NC were increased from 20 μm x 1.5 μm to 50 μm x 10 μm in order to increase the total number of molecules present in the concentrated sample after a given period of preconcentration. Similarly, the cross-sectional dimensions of the suspended microchannel of the SMR were increased from 8 μm x 3 μm to 15 μm x 3 μm so that the suspended volume of this channel would roughly approximate the volume of a fully concentrated sample (~ 25 pL). The main advantage of this approach is that there are two separate fluidic paths through the device, which enables site-specific functionalization of the SMR suspended microchannel surfaces and passivation of the NC anodic microchannel (Fig. 6-4B). By maintaining the outlets of these two channels at atmospheric pressure and elevating the pressures at their inputs to appropriate values which are determined empirically beforehand, it is possible to localize reagents for surface activation (shown in red in the figure) to the SMR while localizing reagents for surface passivation (shown in blue) to the anodic microchannel of the NC. After surface treatment, preconcentration can be accomplished by balancing the pressures at all channel termini and applying appropriate voltages (Fig. 6-4C). After sufficient time has passed to achieve the desired sample concentration, the concentrated sample plug (shown in yellow in the figure) is then transferred to the suspended microchannel of the SMR by lowering the pressure of this channels outlet relative to the common pressure at the other channel termini (Fig. 6-4D). The inlet channel to the SMR was designed to be half the width of the rest of the channel in order to minimize dilution of the concentrated sample by fluid entering the SMR from this channel during sample transfer.

The “sample transfer” concept for the type 1 integrated device design was employed in the first and second generations of the microfabrication process, which are described in greater detail in Sections 6.2.1 and 6.2.2. A second concept was also considered in which preconcentration of the sample plug takes place inside the SMR, which is referred to as the type 2 integrated device and is illustrated in Figure 6-5. In this design, which was employed in the second and third generation fabrication processes (Sections 6.2.3 and 6.2.4), the ability to selectively passivate suspended microchannel surfaces upstream of the detection region is sacrificed under the assumption that sample loss due to upstream binding is small compared to losses experienced due to sample transfer in the type 1 device. In addition to removing the need to transfer the sample, the simpler channel topology in the type 2 design is advantageous in that only two pressures need to be balanced in order to achieve stable preconcentration, compared with four in the previous approach. One disadvantage of the type 2 design is that the volume of the concentrated sample plug is limited by the dimensions of the SMR to ~1 pL, only ~5% of the total SMR volume. However, this can be mitigated by locating the sample plug closer to the

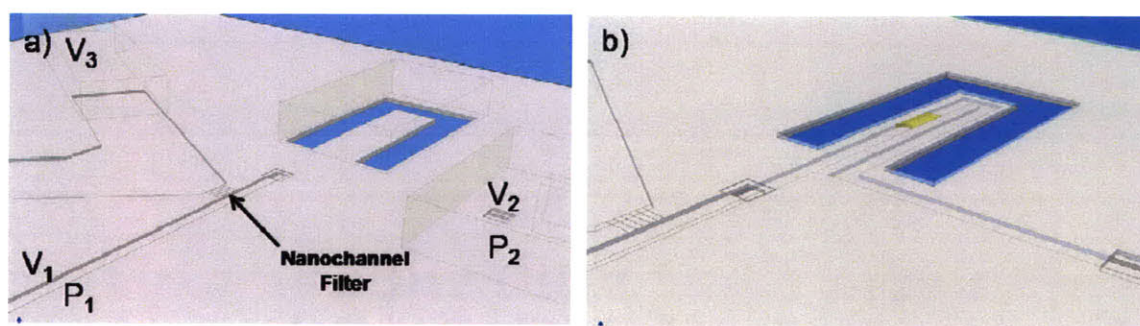


Figure 6-5: Type 2 integrated device concept, in which sample is preconcentrated inside the SMR. (a) Overview of the device with voltage and pressure nodes used for preconcentration. (b) Cut-away view of the device with capping layer transparent. In this scheme, preconcentration requires balancing only two pressures, compared with four in the first concept (Fig. 31).

tip of the SMR, where changes in resonance frequency are more sensitive to mass changes.

6.1.3 Theory of Operation

To determine the detection limit of the integrated system, we consider the dynamic binding of a sample plug containing concentrated ligands to receptor-functionalized SMR surfaces (Fig. 6-6). In this model, the sample has a fixed volume V and concentration c_0 , which represents the end-point concentration after preconcentration. The SMR surface receptors have surface density R_T and are completely unbound at the beginning of the simulation. Ligands have diffusivity D , and receptor-ligand binding is characterized by a forward reaction rate, k , and dissociation constant, K_D . The parameters used in the simulation are summarized in Table 6.1. The differential equations for the free ligand concentration (here normalized by its initial concentration, $\Theta = c/c_0$) and the fraction of

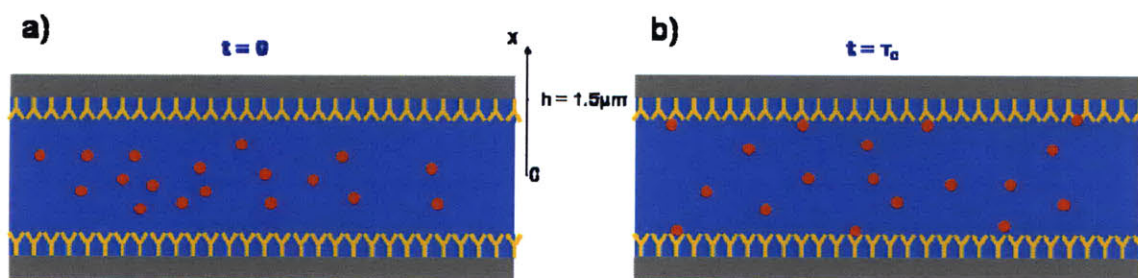


Figure 6-6: Model system for binding of the concentrated sample plug (red) to SMR surface receptors (yellow). A cross-section of the suspended microchannel is shown where the x -direction is vertical and the horizontal dimension spans the width of the channel ($w \gg h$). (a) Receptors are initially unbound at the beginning of the simulation. (b) After a settling time τ_c , which is characteristic of equilibrium, receptor binding has increased, and ligand concentration has decreased due to finite sample size.

<i>Symbol</i>	<i>Definition</i>	<i>Values Simulated</i>
V	Sample Volume	25 pL (type 1) 1.25 pL (type 2)
A	SMR Surface Area	$2 \times 10^{-4} \text{ cm}^2$
k	Forward Reaction Rate	$4 \times 10^4 \text{ M}^{-1} \text{ s}^{-1}$
c₀	Initial Ligand Conc.	0.1 μM -0.1 mM
D	Ligand Diffusivity	$10^{-7} \text{ cm}^2/\text{s}$
K_D	Dissociation Const.	10^{-9} - 10^{-5} M
R_T	Receptor Density	1 pmol/cm^2

Table 6.1: Parameters used in the model of dynamic binding of a sample plug containing concentrated ligands to receptor-functionalized SMR surfaces

bound receptors, R , in terms of normalized time ($\tau = tkc_0$) and space ($\xi = x/h$) are:

$$\Theta_{\tau} = \Theta_{\xi\xi} \quad \text{Eq. 6.1a}$$

$$\dot{R} = \frac{kh^2c_0}{D} \Theta(1, \tau)(1 - R(\tau)) \quad \text{Eq. 6.1b}$$

The boundary conditions for this system are given by

$$\left. \frac{\partial \Theta(\xi, \tau)}{\partial \xi} \right|_{\xi=0} = 0 \quad \text{Eq. 6.1c}$$

$$\left. \frac{\partial \Theta(\xi, \tau)}{\partial \xi} \right|_{\xi=1} = -\frac{khR_T}{D} \Theta(1, \tau)(1 - R(\tau)) \quad \text{Eq. 6.1d}$$

due to symmetry and conservation of ligands at the surface, respectively. The initial conditions are:

$$\Theta(\xi, 0) = 1 \quad \text{Eq. 6.1e}$$

$$R(0) = 0 \quad \text{Eq. 6.1f}$$

The Damkohler number, defined as

$$Da = \frac{khR_T}{D}$$

is a measure of the relative significance of reaction and diffusion. Since the Damkohler number for this system is 6×10^{-2} , it is expected to behave in a reaction-limited manner, so that diffusion rapidly equalizes any concentration gradients, and we can consider the concentration independent of space, except in a very small boundary layer near the wall where the reaction occurs. With this assumption, we can reduce the coupled system of PDE's described by Equations 6.1 to a single differential equation for the bound receptor fraction and a simple conservation of ligands relationship describing the free ligand concentration:

$$\dot{R} = \left(1 - \frac{\phi R_T}{c_0} R\right) (1 - R) - \frac{K_D}{c_0} R \quad \text{Eq. 6.2a}$$

$$\Theta = 1 - \frac{\phi R_T}{c_0} R \quad \text{Eq. 6.2b}$$

where ϕ represents the surface area to volume ratio. For the type 1 integrated system, the volume of the concentrated sample plug was assumed to be equal to the volume of the suspended part of the SMR channel. The temporal response of the bound fraction of receptors for a range of initial concentrations, c_0 , was determined by repeatedly solving Equations 6.2 subject to the initial condition Equation 6.1f. From these simulations, the bound fraction in equilibrium was recorded for each simulated initial concentration, and the settling time was recorded as the time needed for the bound fraction to reach 95% of

its equilibrium value. The resulting equilibrium bound fractions and settling times for the type 1 integrated system are shown in Figure 6-7 for a range of dissociation constants. A fully ligated surface is expected to cause a shift in resonant frequency of ~ 1 Hz, and based on previous experience with standalone SMR systems, a conservative estimate of the minimum resolvable shift is ~ 100 mHz due to baseline drift. Therefore, for the purposes of the simulation, the threshold used to define the detection limit is taken to be one tenth of the full-scale signal, as indicated by the dashed line in Figure 6-7B. The detection limit is determined by dividing the concentration corresponding to the intercept with this threshold by the net preconcentration factor. For the type 1 integrated system, this was taken to be the maximum factor achievable in one hour, or 10^4 . For the type 2 system, maximum preconcentration factor of 500 was assumed because of the 20-fold volume mismatch between the concentrated sample and the SMR. This is a conservative estimate which assumes that the concentrated sample diffusively fills the SMR volume

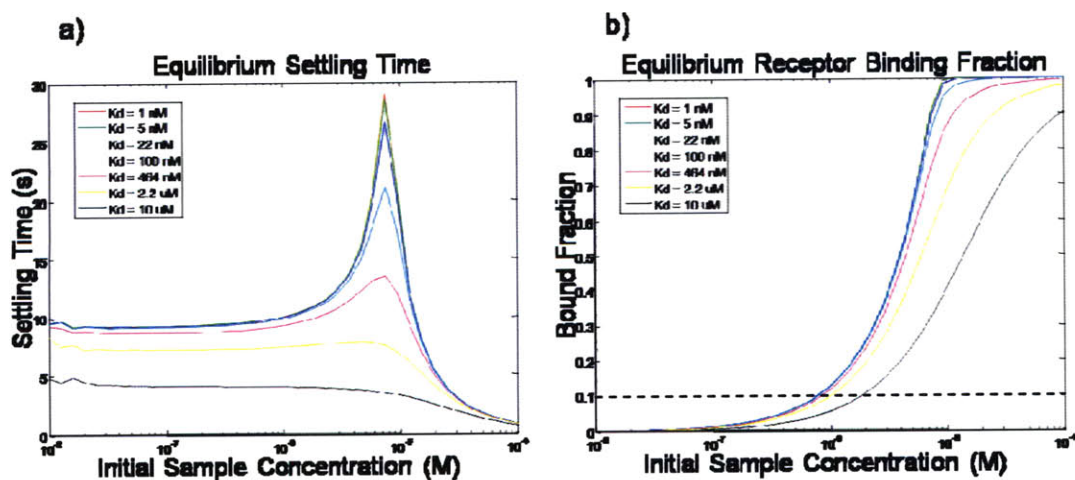


Figure 6-7: Simulated dynamic binding of a sample plug containing concentrated ligands to receptor-functionalized SMR surfaces for different ligand concentrations and dissociation constants in the type 1 integrated system. (a) Time required to reach 95% of the equilibrium bound fraction. (b) The fraction of bound receptors in equilibrium. The dashed line indicates the estimated noise level of the integrated system.

before reacting with the surface when in fact binding will be spatially focused at the tip of the cantilever where the sample plug is located during preconcentration. In Figure 6-8, the detection limits of the type 1 and type 2 integrated systems are compared with that of a conventional immunoassay in which ligand is continuously flowed through the SMR without preconcentration until equilibrium is reached. It is evident from these plots that the detection limit in the integrated system is much less sensitive to the properties of the probe compared with a conventional immunoassay. This arises from the fact that the equilibrium reached in the integrated system is determined by the finite number of molecules in the sample after preconcentration, and this feature is absent from a conventional immunoassay where convective transport of the ligand is sufficiently large that free ligand depletion can be ignored. Because the sample is finite in the concentrated sample plug, significant depletion of the free ligand concentration can occur as it

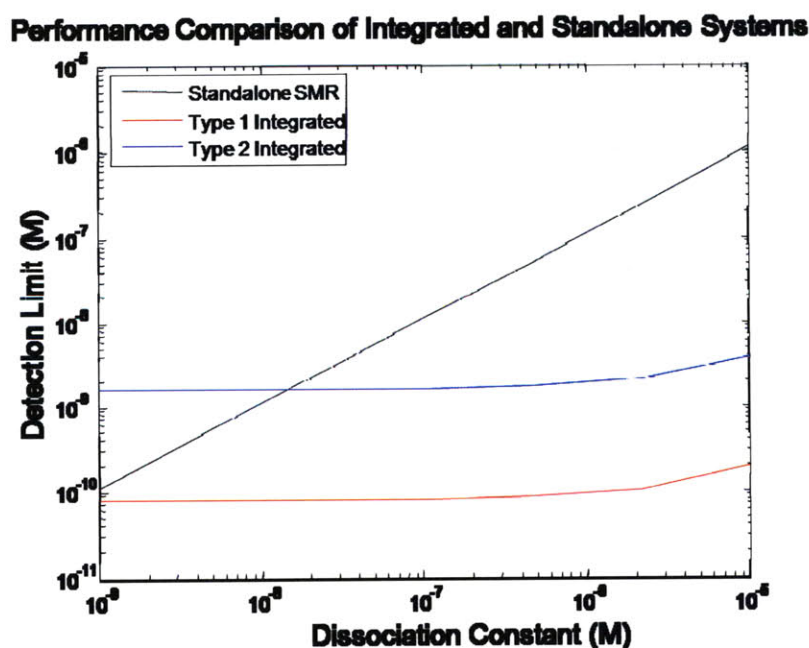


Figure 6-8: Comparison of the detection limits of the type 1 and type 2 integrated systems with a conventional immunoassay in which ligand is flowed continuously without preconcentration through the SMR until equilibrium is reached.

equilibrates with the surface, and this results in a sharp binding response when the concentration of the sample, c_0 , surpasses the concentration of receptors in the SMR ($R_T A/V = 8 \mu\text{M}$ in this simulation), as seen in Fig. 6-7B. Hence for probe systems where the dissociation constant is significantly smaller than the receptor concentration, the detection limit of the integrated system approaches this concentration divided by the preconcentration factor. This illustrates one disadvantage of the integrated system: it is not able to take advantage of highly sensitive probes to achieve a lower detection limit like a conventional assay. The conventional assay's performance exceeds that of the type 1 and type 2 integrated systems for dissociation constants below $\sim 1 \text{ nM}$ and $\sim 10 \text{ nM}$ respectively. For dissociation constants significantly larger than the receptor concentration, free ligand depletion can be ignored even for the integrated system, and the detection limit approaches that of the conventional assay divided by the preconcentration factor. As described in Section 6.1.2, the actual detection limit of the type 2 integrated system is expected to lie somewhere between the simulated values for the two systems shown in Figure 6-8, due to sample transfer inefficiency. It is therefore expected that preconcentration will generally produce an improvement in the detection limit for probe systems having a dissociation constant of at least 10 nM .

6.2 Device Design

Two fabrication processes were developed for the type 1 integrated device. Because both these processes produced very low yields, and also due to the low sample transfer

efficiency observed during testing of these devices, attention was directed toward type 2 device designs. Two fabrication processes were also developed for this device, which are referred to as the third and fourth generations from here on. Devices produced using the third generation process exhibited packaging problems which were corrected in the fourth generation.

6.2.1 First Generation

The fabrication process for the first generation device is shown schematically in Appendix A.1.2. In this text, letters in brackets refer to specific process steps which are labeled in the Appendix. The suspended microchannel (b), the connecting channel and the bottom portion of the NC channels (c) are etched into the device layer of an SOI wafer (6.5 μm device layer, 2 μm insulator) using a reactive ion etch (RIE), and a 5000 Å thermal oxide is grown on the wafer (d). Profilometry of these wafers showed that a ridge forms at the top edges of the channels, possibly due to a bird's beak effect. Ridges as large as 15 nm were measured, and they were found to interfere with a later fusion bonding step. Hence the first thermal oxide is stripped in buffered oxide etchant, producing a more rounded upper channel edge, and the same thermal oxide is re-grown. A second SOI wafer (3.5 μm device layer, 2 μm insulator) is oxidized at the same time (e), both wafers are cleaned using standard RCA reagents (SC1, SC2), and their oxidized device layers are fusion bonded together (f). The SOI wafer without channels is then mechanically ground, leaving a silicon film of $\sim 100\ \mu\text{m}$ above its insulator (g). This film

is then removed using a deep reactive ion etch (DRIE) which stops on the insulator, and a different DRIE recipe is used to etch the insulator, stopping on this SOI wafer's device layer (h). Nanochannels with a depth of 40 nm are etched into this surface using an RIE (i). Next, a DRIE produces the outline of the cantilever, switching first from silicon etchant to oxide etchant to etch through the fusion bond layer, and then back to silicon etchant again, stopping finally on the insulator of the lower SOI wafer (j). An RIE then removes the upper portion of the NC channels, giving them a full depth of 10 μm and exposing them to visual observation from above (k). The entire wafer is then thermally oxidized using the same conditions as before in order to electrically passivate the silicon surfaces exposed by the previous etch (l). An RIE removes this oxide at several positions at the die edge, and metal is deposited over them in order to create electrical access for wire bonds (m,n). A pyrex wafer is then anodically bonded to the patterned side of the SOI stack (o), and this pyrex wafer becomes the handle for a second mechanical grinding step which thins the silicon on the opposite side of the stack to $\sim 100\text{ }\mu\text{m}$ (p). The cantilevers are released using a pair of DRIE etches which remove first the remaining 100 μm of silicon and then the insulator from the SOI stack below the cantilever features (q,r). To hermetically package the cantilevers, a second pyrex wafer containing both electrodes for cantilever actuation and getters for gas sequestration is bonded to the SOI stack using glass frit bonding under high vacuum conditions (s). Finally, the top pyrex wafer is partially diesawed to allow access to the bond pads and the dies are separated by a second full depth diesaw cut (t).

The primary failure mode for this process is illustrated in Figure 6-9. Large-scale delamination of the fusion bond occurred, resulting in inadequate packaging of most cantilevers on the wafer. This had not been observed in earlier shortloop testing of the process steps leading up to fusion bonding because these tests were not carried out with the final masks used in the integrated process, but rather a similar mask which was on hand at the time. The higher channel surface area on the actual mask used to pattern the bottom portion of the NC channels was considered a likely cause for the lower bond strength.

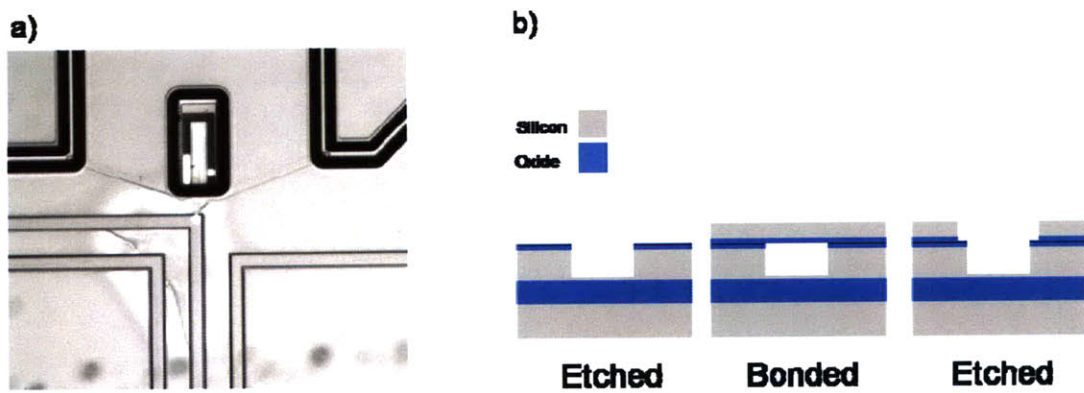


Figure 6-9: Failure mode for first generation fabrication process. (a) Delamination in the fusion bond layer caused cantilevers to leak. (b) NC channels were formed using a two-part etch in this generation.

6.2.2 Second Generation

To make more surface area available for fusion bonding, the first generation process was modified by etching the entire NC channel depth in a single etch after fusion bonding.

This new process step is illustrated in Figure 6-10, and the entire fabrication process is in Appendix A.1.3. This had not been possible at the time of the first generation for two reasons. Firstly, if a standard RIE had been used to etch the full depth, the undercut would have been large enough to significantly alter the cross-sectional geometry of this channel, with unknown consequences for preconcentration phenomena. Secondly, DRIE recipes which would have produced the desired aspect ratio for the channel would not have been able to produce sufficiently small channel sidewall roughness for successful oxide passivation later in the process. This situation was remediated by parallel research carried out in the Han lab which produced a new DRIE recipe able to meet both these requirements.

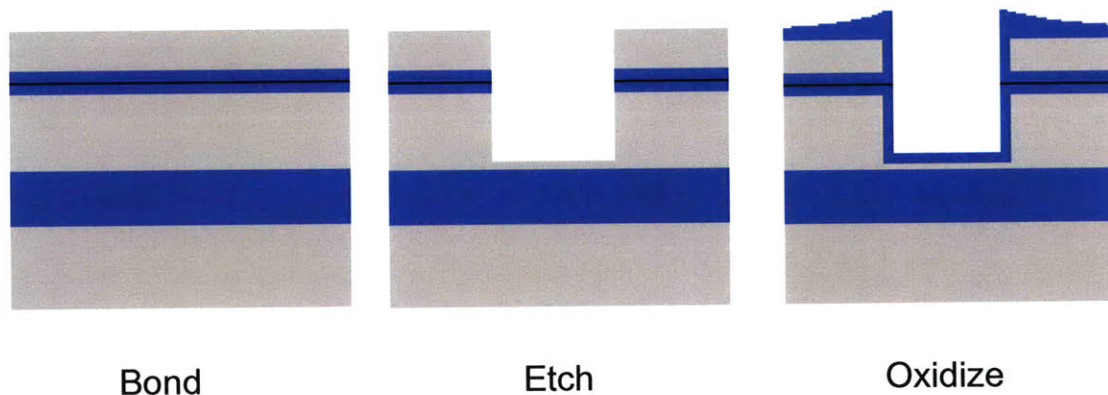


Figure 6-10: The second generation fabrication process increased fusion bond surface area by means of a full-depth DRIE which replaced the two RIE etches used previously to make NC channels. However, oxidation of this structure produced channel edge topography incompatible with nanochannel anodic bonding.

In nearly all devices produced by this process, nanochannels could not be filled with fluid by any means. This was observed visually by the color of the nanochannels under white light microscopy, which normally changes when the channel is filled, and also by ionic current measurements made on the devices using a source-measure unit. Profilometer

measurements indicated that ridge structures were formed at the edges of the channels following oxidation, similar to the ones seen prior to fusion bonding in the first generation process. It was believed that the inability of the anodic bond to conform to these ridges was the cause of the observed nanochannel sealing. Based on this assumption, several alternatives to the process were examined through shortloop testing of only the process steps needed to produce NC features. In one shortloop, a “ledge” was etched into the upper silicon film before etching the full-depth channel using the normal DRIE (Fig. 6-11). Several iterations of this shortloop were carried out in which different “ledge” depths ranging from 1 μm to 3.5 μm were tested. All produced concentrators which were unable to create the concentration polarization phenomena needed for preconcentration. Similar results were obtained for another shortloop in which the NC filter was located in the fusion bond layer by etching nanochannels into the bottom SOI before fusion bonding.

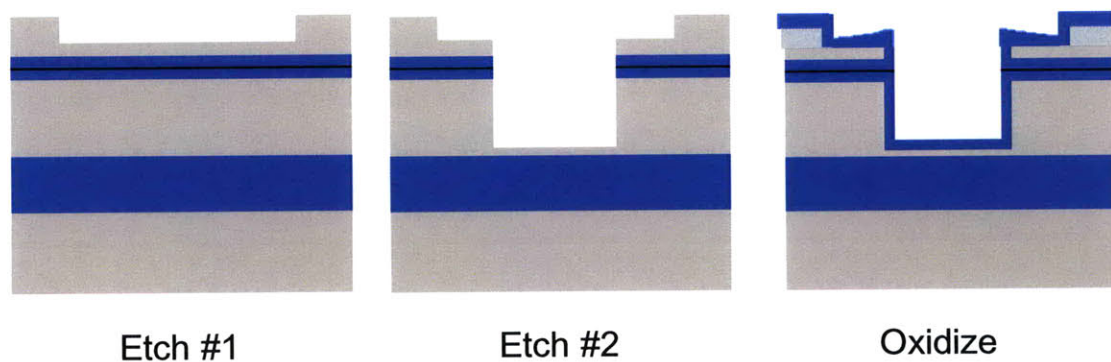


Figure 6-11: Shortloop structure fabricated to mitigate anodic bonding failures observed in the second generation fabrication process. A “ledge” is etched partially into the upper SOI device layer before the normal full-depth DRIE to eliminate interactions between oxidation-related structures and the upper pyrex.

6.2.3 Third Generation

Observations made on the second generation devices showed that no available methods could produce integrated NC structures containing a fusion bond. Therefore the third generation process abandoned this channel structure in favor of a shallower 3 μm deep NC channel contained entirely by the upper SOI device layer. A summary of the process steps which differed significantly from the previous generation's process are illustrated in Figure 6-12, and the entire process is in Appendix A.1.4. Another important difference for this generation was that the layout was changed from the type 1 channel topography to the type 2 topography (see Section 6.1.2).

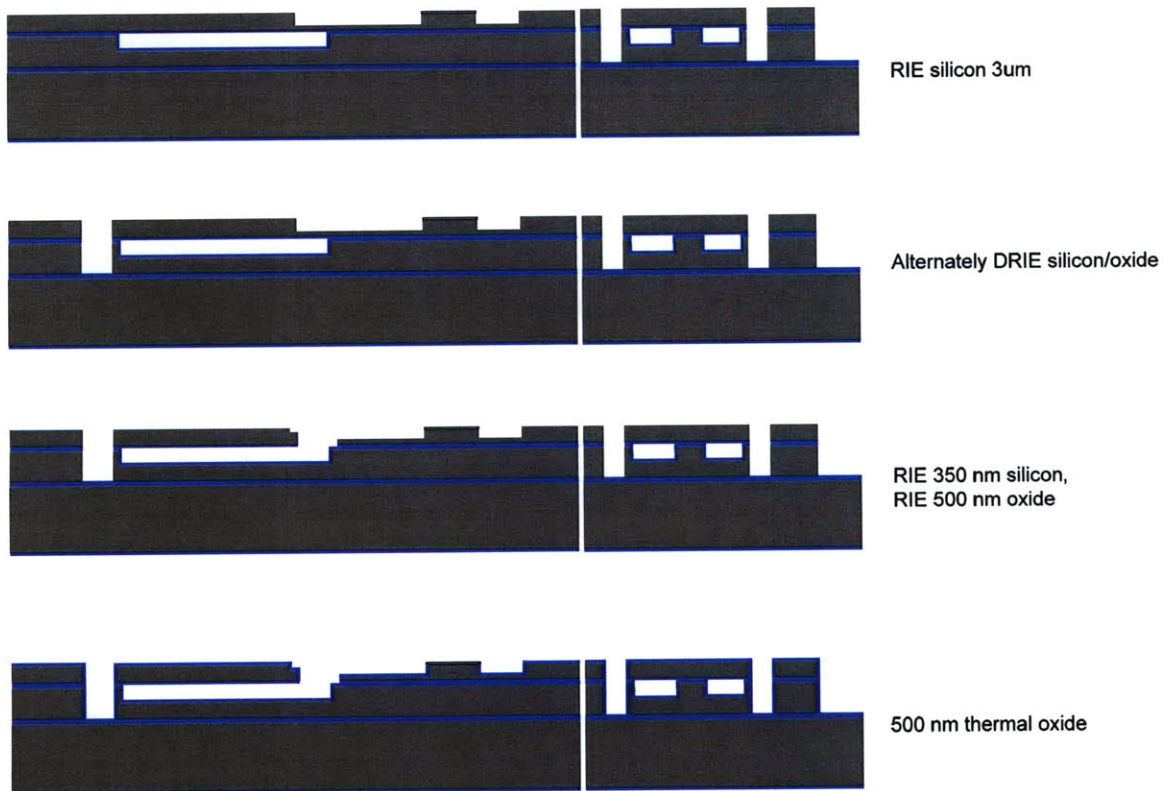


Figure 6-12: Third generation fabrication process steps which differed from the previous generation. NC channels were made shallower to avoid oxidation of multilayer channel structures.

Concentrators produced by the third generation process behaved much more consistently than the previous generation's shortloops, which exhibited drastically different behavior from one device to the next. The behavior of the shallower third generation concentrators is illustrated for a typical device in Figure 6-13. With a relatively small voltage of 10V was applied across the nanochannel filter, the depletion region was self-stabilizing, indicating that a significant EOF was present in the anodic microchannel even though no voltage was applied between the termini of this channel. When the electric field was increased, the depletion region remained stable but gradually shrank in towards the filter. With 70V applied across the nanochannels, the depletion region completely collapsed against the filter. These observations, together with ionic current measurements made on the same devices, suggest that partial delamination of the anodic bond layer in the vicinity of the nanochannel filter results in a higher effective cross section for the filter. This results in sufficient EOF through the filter to stabilize the depletion region without applying an electric field across the anodic microchannel. Although stable, this arrangement is not amenable to efficient preconcentration because the balance between E_n and E_t is fixed by the relative conductivities of the anodic microchannel and the nanochannel filter, and hence preconcentration cannot be optimized. Two studies were



Figure 6-13: Concentration polarization behavior of third generation integrated devices. The voltage applied across the nanochannels is overlaid and the location of the nanochannel filter outlined in red. Although no voltage was applied between the termini of the anodic microchannel, the depletion region was self-stabilizing, indicating EOF through the filter.

conducted to further investigate potential causes of observed failures in the anodic bonding of nanochannels.

In the first study, nanochannels of different dimensions were patterned across six silicon wafers and a 5000 Å thermal oxide was grown on each wafer. Blank pyrex wafers were then anodically bonded to the silicon wafers under a variety of conditions. Three wafers were bonded using a graphite chuck and the other three using a steel chuck. For each set of three wafers, one was bonded at 400°C and 800V, one at 400°C and ~1000V, and one at 450°C and ~1000V (due to power supply current limits, the maximum applicable voltage varied somewhat between experiments). After bonding, wafers were examined using a white light microscope to determine if nanochannels were collapsed, and the results are summarized in Figure 6-14. Based on these results, it was determined that the graphite chuck produced the most uniform bond, and that the most extreme bonding conditions that could be employed without significant nanochannel collapse were 400°C and 1000V. A seventh silicon wafer with the same oxidized nanochannel pattern was then bonded to a pyrex wafer containing through holes, and although nanochannels were still not collapsed, fringes appeared at critical locations in the anodic bond layer, indicating heterogeneities previously associated with non-functional NC devices. It was therefore hypothesized that the presence of holes in the pyrex was the cause of the inhomogeneous anodic bond. However, the absence of anodic and cathodic microchannels on the silicon wafers made it impossible to verify this directly by probing the electrical characteristics of the nanochannels when filled with fluid.

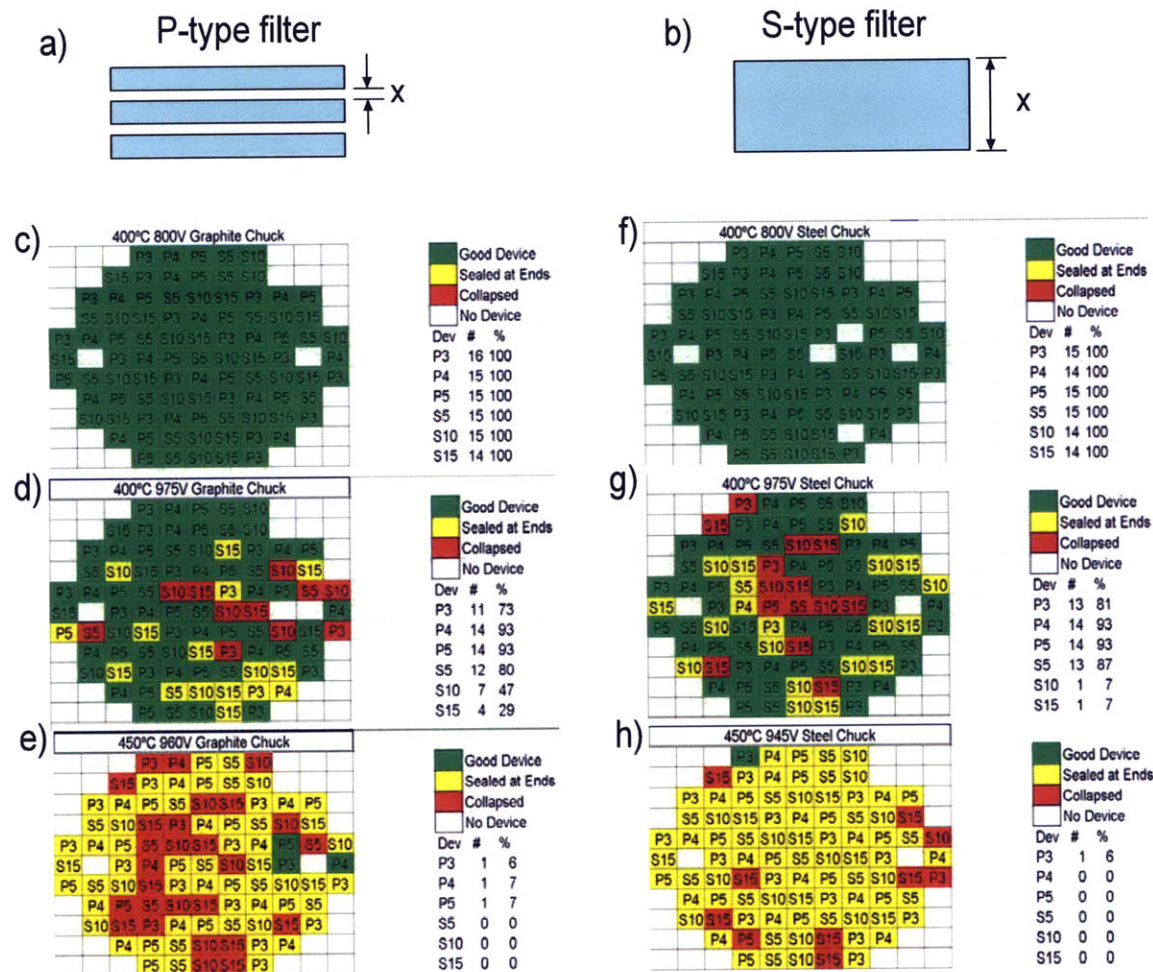


Figure 6-14: Results of nanochannel anodic bonding study. Nanochannel structures of two types were tested. (a) P-type filters are labeled PX where X refers to the width of pillars between three 5 μm x 40 nm nanochannels. (b) S-type filters are labeled SX where X refers to the width of a single 40 nm deep nanochannel. Bonding was performed using either a graphite chuck (c-d) or a steel chuck (f-h) at the temperatures and voltages indicated in the Figure. Following bonding, filters were observed under a white light microscope to determine if nanochannels were intact (green), sealed at the ends (yellow), or completely collapsed (red).

In the second study, NC devices were fabricated by a process which duplicated, as exactly as possible, the one used by the Han group to produce the original NC devices which formed the basis for the present study. The only notable difference between this process and the third generation integrated process is that fluidic ports to the device are made through the silicon rather than through the pyrex which is anodically bonded to it. The test results for this device are summarized in Figure 6-15. When the device was

configured for preconcentration, the pattern of ion depletion, as determined by the pattern of protein fluorescence, showed widespread conduction of ions throughout the anodic bond layer. In order to simulate conditions in the integrated device, the anodic microchannel in this device was made serpentine. As a result, two stable depletion regions were produced at locations where the electric field in the anodic bond layer is greatest. The edge of the first region was at the base of a hairpin-shaped section of the anodic microchannel, and that of the second was at the point where the anodic and cathodic microchannels first come into proximity. Protein accumulated only at the boundary of the first depletion region unless the potential difference $V_1 - V_2$ was increased enough to allow protein to bypass the first depletion region, in which case it accumulated at the second boundary. Comparison of these observations to those made on the third generation integrated devices lead to the conclusion that the presence of holes in the pyrex wafer which is anodically bonded to the nanochannels compromises the integrity of the anodic bond, resulting in delaminated nanochannel structures.

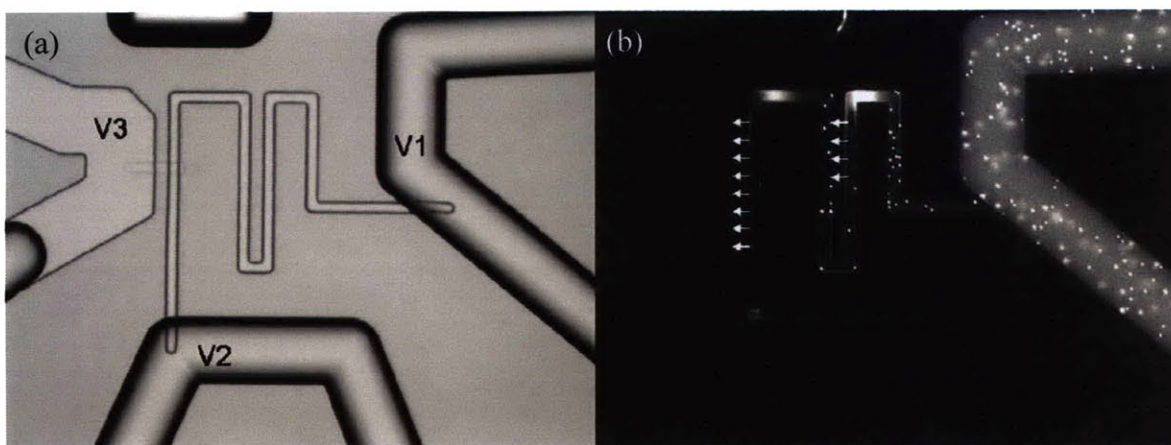


Figure 6-15: Concentration polarization behavior of silicon -ported NC devices. (a) A bright-field image of the device with voltages used to establish preconcentration overlaid. (b) A fluorescence image of the device filled with a mixture of fluorescent bovine serum albumin and fluorescent microspheres to simultaneously visualize ion depletion and fluid flows. Ion currents through the anodic bond layer are indicated with white arrows.

Comparison with observations made by the Han group on their silicon-ported NC devices suggests that ionic current through the anodic bond layer is a general phenomenon affecting all devices made with this process, but the extent to which they affect concentration polarization depends on the precise channel topography of the device. The lack of serpentine channels in devices built by the Han group and the greater silicon surface area available for anodic bonding in their design may explain why these ion leakage phenomena were not observed in their original experiments.

6.2.4 Fourth Generation

In order to achieve optimum conditions for the anodic bonding of nanochannels, the fourth generation process was designed to produce integrated devices with macroscopic fluidic ports in the SOI stack rather than the top pyrex. The important differences between this device and the third generation device are summarized in Figure 6-16, and the entire fabrication process is shown in Appendix A.1.5. In this process, fluid ports were produced by first etching through both device layers of the SOI stack using the same DRIE recipe that was used to etch NC channels in the second generation process. Then an RIE removed oxide from the bottoms of these wells. Front-side processing remained otherwise the same as the third generation except that a partial etch into the cantilever lid was added to provide visual access to the inside of the SMR during preconcentration. Anodic bonding was performed using pyrex wafers with fluidic channels etched into them but no through holes. After backside grinding of the SOI stack,

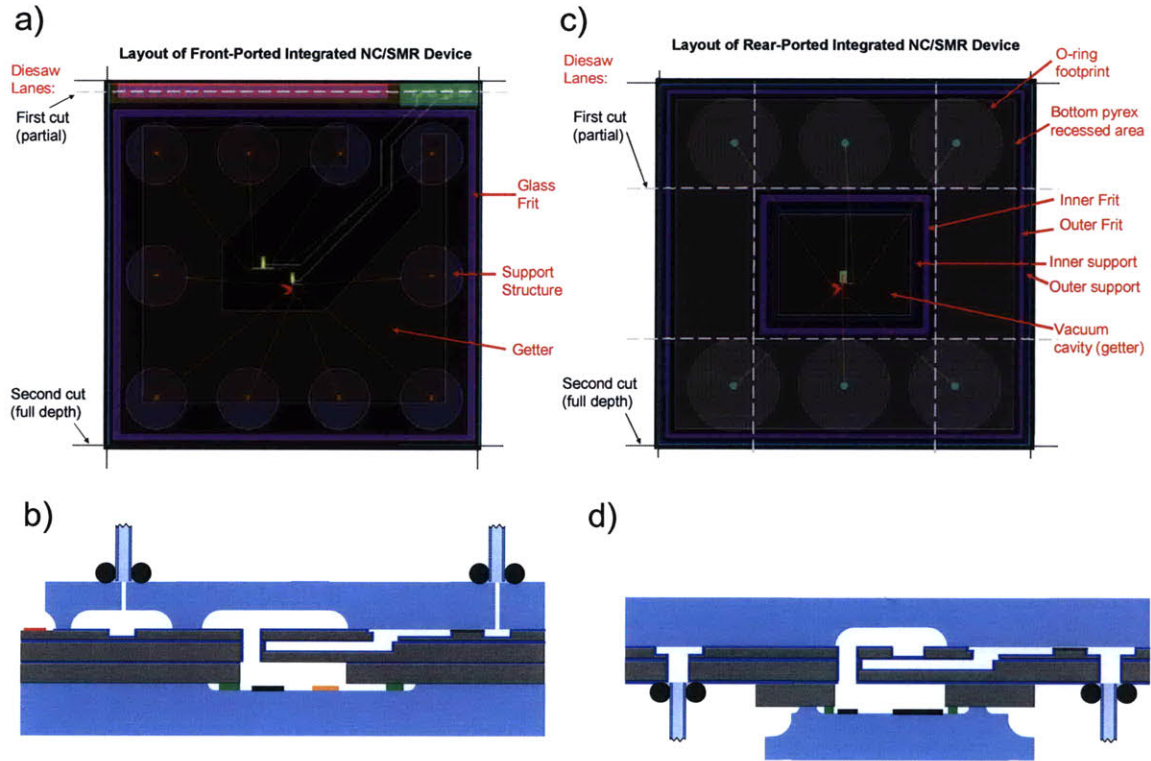


Figure 6-16: Comparison of third and fourth generation fabrication processes. (a) Layout of third generation device showing locations of relevant packaging features. (b) Cross-section of third generation device showing macroscopic fluidic connections to ports in the top pyrex. (c) Layout of fourth generation device. (d) Cross-section of fourth generation device showing macroscopic fluidic connections to ports in the SOI stack.

the DRIE step used to release the cantilevers also etched 3mm-diameter circular wells centered on the fluidic ports in the front side of the stack, stopping on the bottom SOI's insulator. This provided an insulating silicon oxide surface for the fluidic manifold to contact. However, these ports were subsequently obscured by the bottom pyrex after frit bonding. In order to make the ports accessible again, four additional partial diesaw cuts were performed to isolate the section of the bottom pyrex needed for SMR packaging from the sections which obscured fluidic ports. A second frit ring was added to the outer edge of the die so that slurry from the final full-depth diesaw cut would not be able to contaminate the fluidic ports.

6.3 Device Characterization

6.3.1 Type 1 Integrated Device

One device from the second generation fabrication process was found to have both NC and SMR functionalities. The NC from this device was first characterized by preconcentrating quantum dots (QD800, Life Technologies, Carlsbad, CA) with a concentration of 16 nM in 15 mM PBS and monitoring their fluorescent intensity over time (Fig. 6-17). The device was found to preconcentrate these nanoparticles in a stable

Preconcentration of Quantum Dots Using Type 1 Integrated System

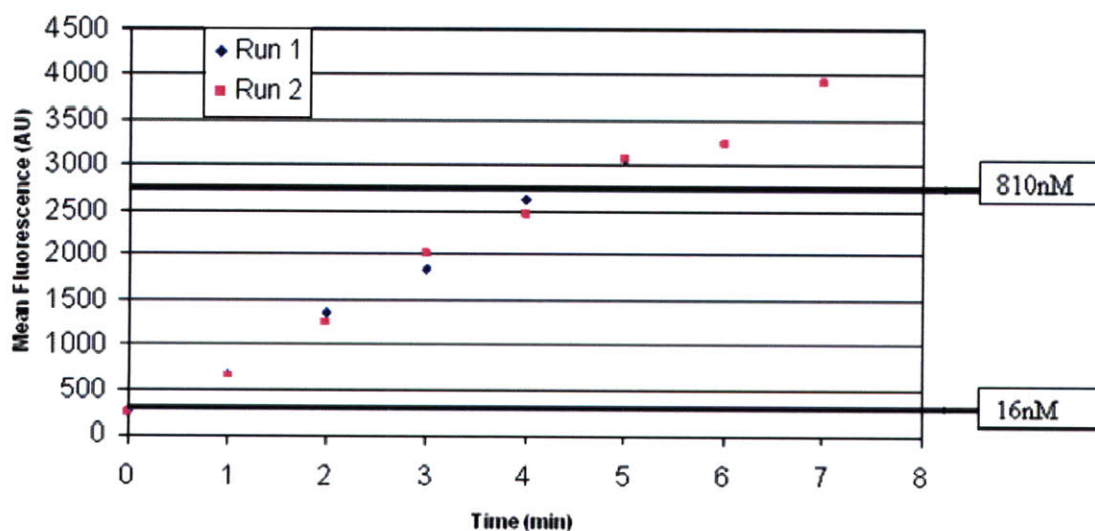


Figure 6-17: Preconcentration of 16 nM quantum dots using the type 1 integrated system produced by the second generation fabrication process. Fluorescent intensity of the concentrated sample plug is measured at 1-minute intervals during preconcentration. Horizontal lines indicate fluorescence of the channel when filled with QD's of known concentration.

and repeatable manner. The fluorescence of the channel was also measured when filled with quantum dots of known concentrations to quantify the rate of preconcentration. The device was found to produce a gain of ~ 100 in a ten minute period.

The same quantum dots used in the NC characterization were preconcentrated for a period of five minutes, resulting in a concentrated sample with a concentration of ~ 800 nM, and then transferred to the SMR by pressure-driven flow. The response of the SMR resonance frequency following sample transfer was found to be qualitatively repeatable (Fig. 6-18). However, the expected decrease in resonant frequency due to the added mass of the quantum dots was masked by a larger increase in resonant frequency apparently due to the localized ion depletion caused by preconcentration. Based on

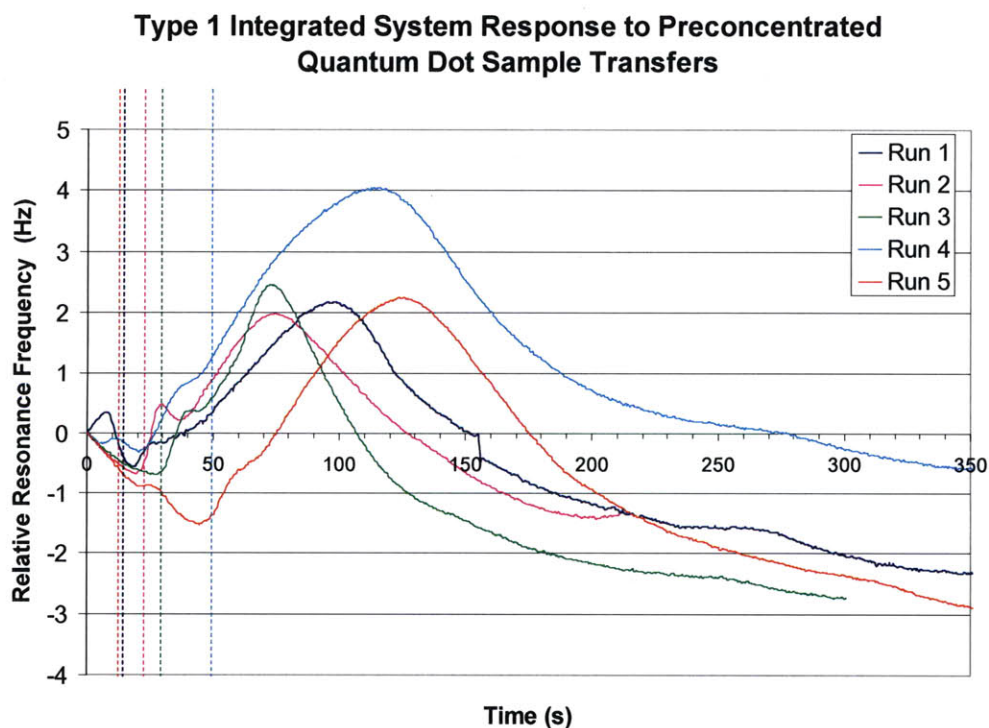


Figure 6-18: Response of the type 1 integrated system resonant frequency following transfer of quantum dots preconcentrated to 800 nM. Vertical lines indicate the approximate time of sample transfer for each run. Sample transfers lasted 10-20 seconds each.

measurements made on a standalone SMR system, the resonant frequency of the integrated system was expected to shift by ~ 10 Hz when completely filled with quantum dots at 800 nM. These experiments demonstrated the practical difficulties associated with maintaining a stable SMR resonant frequency baseline while performing the manipulations of fluid pressure and voltages needed to transfer the sample. Another shortcoming of this system was that the multi-channel topography of the device made it impractical to transfer samples by pressure-driven flow without dilution from adjacent channels. This led to the development of the type 2 integrated device concept.

6.3.2 Type 2 Integrated Device

Devices produced using the fourth generation fabrication process were first characterized in terms of packaging yield. The outer pieces of the bottom pyrex could easily be removed by first swabbing the device with acetone and then applying a razor blade to the glass frit interface. Acetone partially dissolves the outer frit and allows it to break with only a small applied force, which in turn helps maintain the integrity of the inner frit. After removing the outer bottom pyrex from 33 devices, their quality factors were measured by piezoelectric actuation in open loop combined with optical lever readout using a spectrum analyzer (model 4395A, Agilent Technologies, Santa Clara CA). This set of devices had a mean quality factor of ~ 700 with a standard deviation of ~ 200 , indicating that the diesawing scheme was successful (Fig. 6-19).

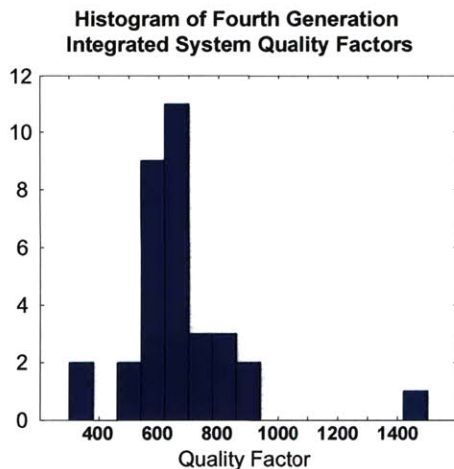


Figure 6-19: Quality factors measured on type 2 integrated devices produced by the fourth generation fabrication process. The mean quality factor was 700, and the standard deviation was 200.

The devices were next characterized in terms of their electrical passivation properties. Devices with two types of channel topography were fabricated in this process in order to facilitate electrical characterization (Fig. 6-20A,B). In one device, referred to here as “connected”, the SMR channel was oriented in the normal way which connects the upper and lower bypass channels. In the other device, referred to here as “disconnected”, the orientation of the SMR channel was mirrored so that no fluid connection could be made between these two bypasses. After filling a device with 15 mM PBS, the ionic current between the fluidic ports was measured using two methodologies (Fig. 6-20C,D). First, the device was mounted using the standard o-ring manifold, and electrical connections were made through electrodes in external reservoirs (for more details, see Fig. 3-2 and Appendix A.3). Second, reservoirs made from pipet tips were attached directly to the device using UV epoxy, and electrodes were mounted inside them. Using either method, when 10V is applied between the ends of a bypass, currents on the order of a few hundred nanoamps are expected. A current of a few tens of nanoamps should be produced when the same voltage is applied across the SMR. Finally, a current on the order of 1 nA is expected when this voltage is applied across a functional nanochannel filter. The observed ionic currents for the pipet tip measurements and those for the o-ring manifold

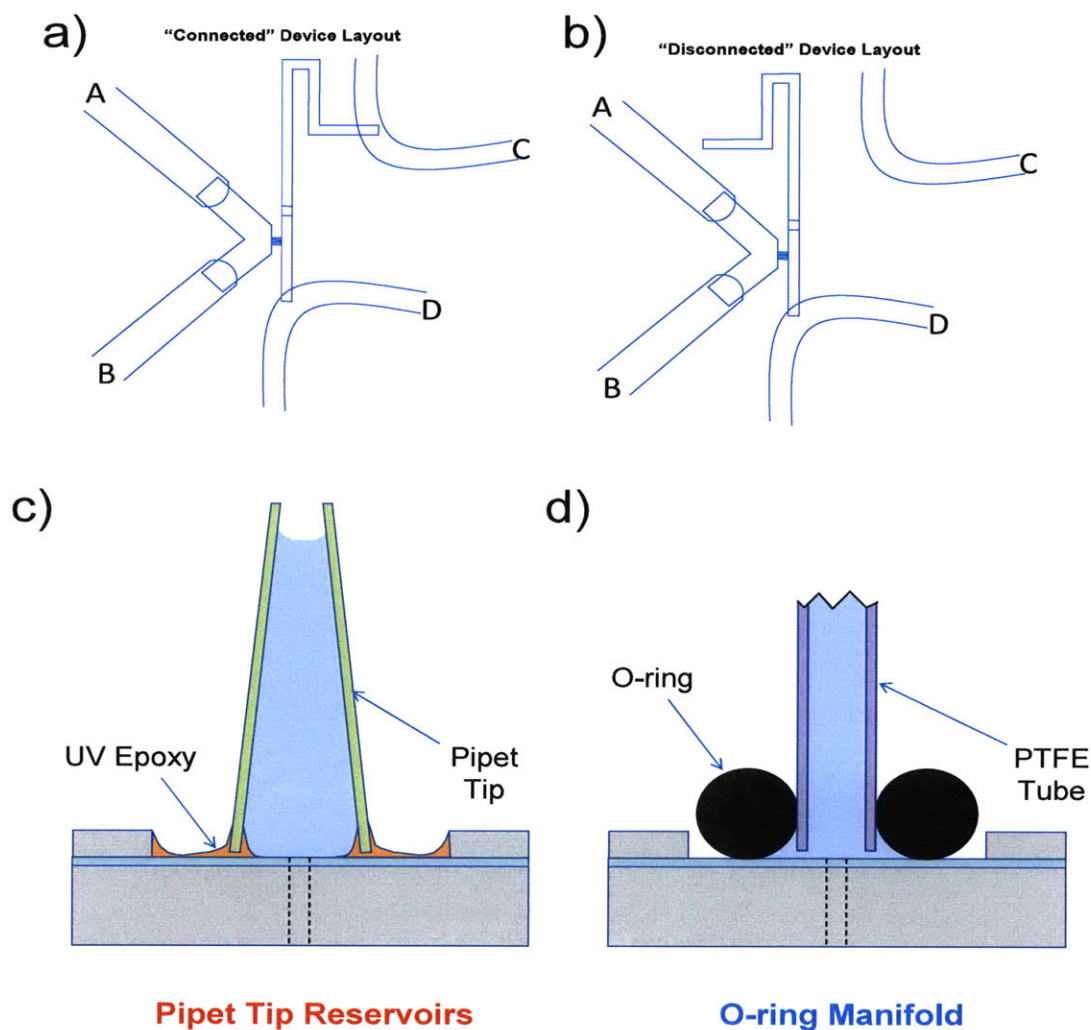


Figure 6-20: Electrical characterization of fourth generation integrated devices. Channel layouts are shown for (a) "connected" devices possessing a continuous fluid path between ports C and D, and (b) "disconnected" devices where no path exists. Ionic currents were measured both with (c) pipet tips epoxied to the device and (d) the o-ring manifold. In this diagram, the manifold is shown as a partial cutaway. For greater details, see Appendix A.3

are listed in Tables 6.2 and 6.3. From the pipet tip data, summarized in Table 6.2, it is evident that some devices of both types possess the desired electrical properties, whereas others do not. The above normal currents seen in devices 1 and 3 are most likely due to ion conduction through the anodic bond layer, based on their magnitudes, but this could not be verified because current measurements did not permit visual access to the devices.

From the o-ring manifold data, summarized in Table 6.3, it is evident that the o-ring is not able to seal against the surface of the device enough to prevent fluid from electrically shorting through the adjacent silicon. The higher fragility of these devices, due to their reduced thickness relative to previous generations, makes it impossible to correct this situation by simply increasing the clamping force of the manifold.

<i>Device #</i>	<i>Device Type</i>	<i>I_{A-B} (nA)</i>	<i>I_{C-D} (nA)</i>	<i>I_{A-C} (nA)</i>	<i>I_{B-D} (nA)</i>
1	Connected	413	56.9	29.9	30.6
2	Connected	465	56.4	1.9	3.5
3	Disconnected	558	11.4	4.1	11
4	Disconnected	493	0.1	0	5.5

Table 6.2: Ionic currents measured in nanoamps with 10V applied using pipet tip method (see Fig. 6-20).

<i>Device #</i>	<i>Device Type</i>	<i>I_{A-B} (nA)</i>	<i>I_{C-D} (nA)</i>	<i>I_{A-C} (nA)</i>	<i>I_{B-D} (nA)</i>
3	Disconnected	128	-	57.9	42
4	Disconnected	149	29.4	44.2	66.5
5	Disconnected	160	-	40	75

Table 6.3: Ionic currents measured in nanoamps with 10V applied using o-ring manifold method (see Fig. 6-20).

Chapter 7: Conclusions

This thesis has demonstrated that the SMR provides a means of quantitatively differentiating mixed aqueous suspensions of polystyrene microspheres on the basis of particle mass and electrokinetic surface charge. Because the technique measures individual particles, it has the potential to provide information that is obscured by other techniques based on ensemble average measurements. Furthermore, knowledge of both the mass and charge of individual particles in a complex mixture can enable more effective differentiation of sub-populations than either parameter by itself.

The technique has also been demonstrated as a quantitative method for simultaneous measurement of the EPM and buoyant mass of single bacterial cells. The unique ability of this instrument to measure both of these quantities at the single-cell level has been used to investigate the action of the antimicrobial peptide cecropin A-melittin on the outer membranes of *E. Coli* cells in a way that would not have been possible otherwise. Although the changes in *E. Coli* surface charge associated with peptide-mediated permeabilization are not resolvable by the current instrument, the methods presented here are general. Further research into fabrication processes which can produce lighter cantilevers having thicker, more uniform passivation oxide films is recommended in order to enable a quantitative test for a correlation between buoyant mass, EPM and permeability. It is evident from Equation 2.14 that a larger mobility signal, as measured by the total rate of change of the resonance frequency, can be obtained either by increasing the first term in the expansion, which is inversely proportional to cantilever

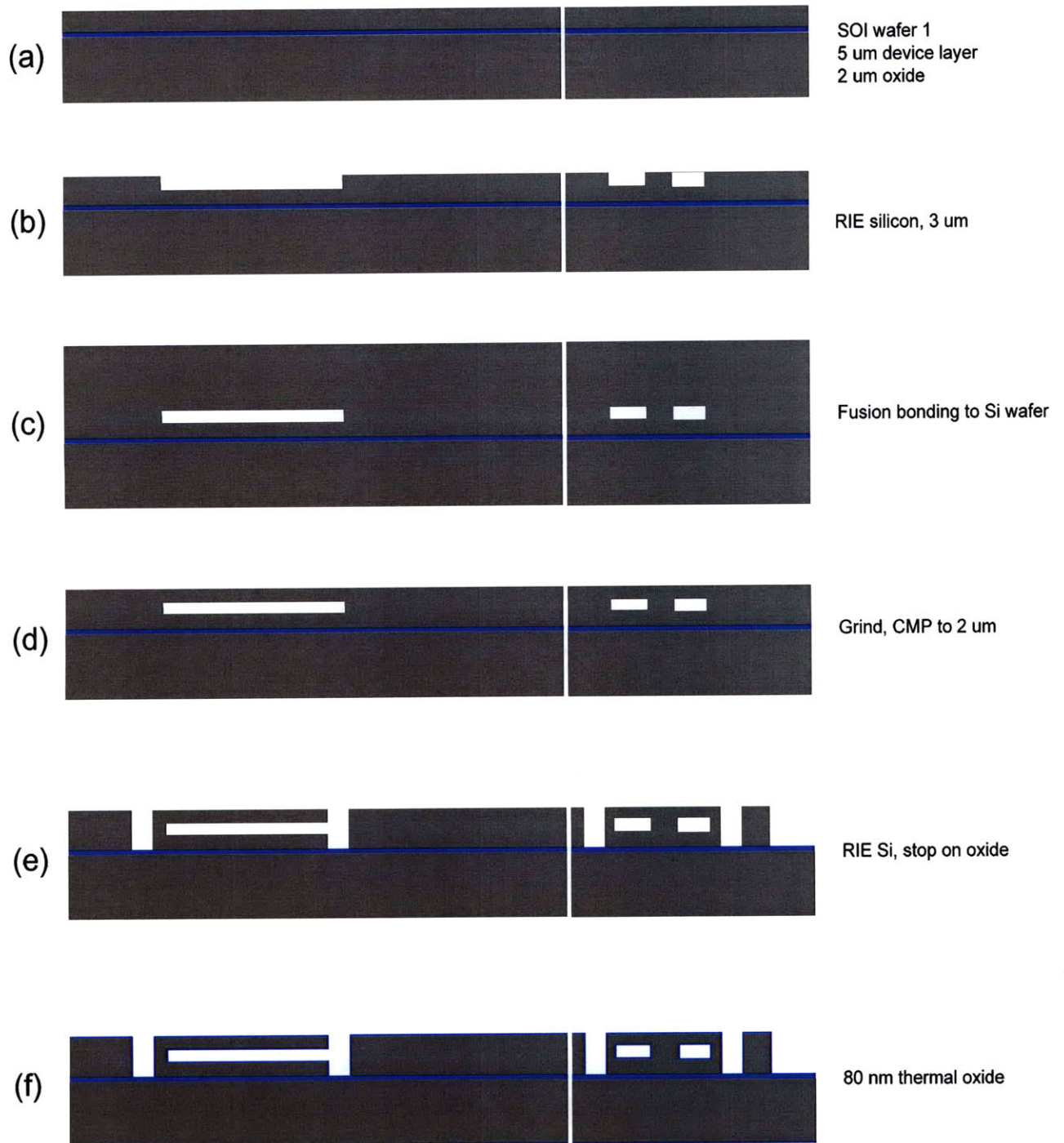
mass, or the second term, which is proportional to the maximum electric field that can be supported by the device. Hence improvements which are made in either of these areas will multiply one another in determining the overall improvement in the SNR of the EPM measurement. Even without these improvements, the current instrument is able to resolve heterogeneity in the EPM distributions of cells which is invisible to the most commonly employed cellular EPM techniques, which are based on population average measurements. It is believed that this additional information will help inform studies of the initial kinetics of bacterial biofilm formation which currently ignore this heterogeneity. The SMR compares favorably with existing single-cell EPM measurement techniques mainly because it does not rely on expensive imaging equipment and shows a greater potential for cost-effective mass production.

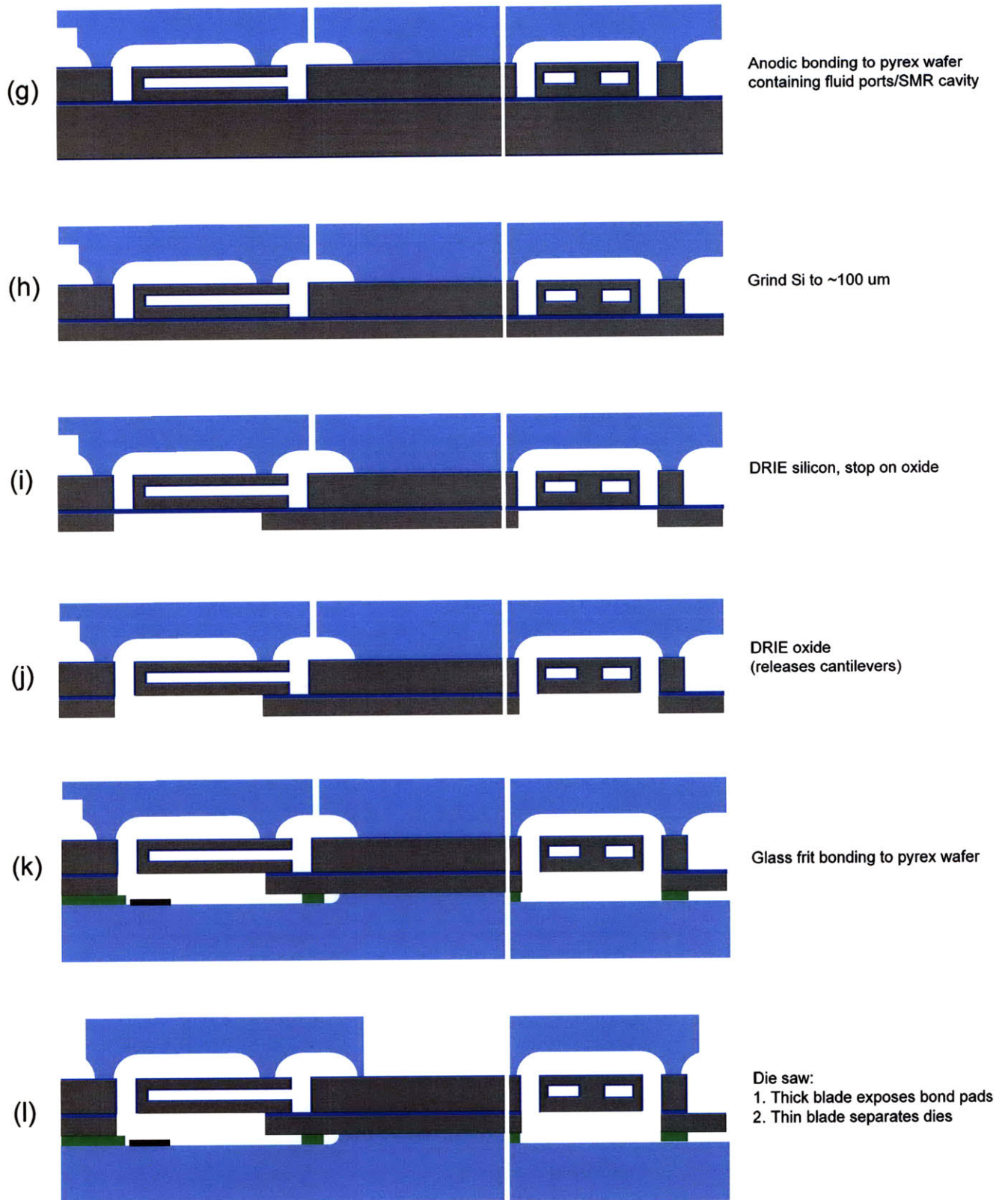
A great number of interesting applications of the instrument involve measurement of cells having diameters on the order of 10 μm . However, due to the low oxide breakdown voltage and large oscillatory background signal observed in the characterization of the OLSMR device, the present instrument is limited to particles having diameters less than 3 μm . For this reason, fabrication processes are currently being investigated to produce OLSMR devices with more robust passivation oxide films. Since electrolytic gases seemed to originate from the sidewalls of the buried channel ports, it is believed that the DRIE recipe used to create both the ports and the cantilever outline is creating surface topography which is not compatible with uniform thermal oxide growth. This DRIE recipe was selected for its high aspect ratio, which is a requirement of the cantilever outline portion of the etch. Therefore, two new masks have been designed in the place of

this one mask, so that the high aspect ratio DRIE recipe can be used to create the cantilever outline while a separate recipe optimized for low surface roughness can be used for the ports. Thicker, more uniform passivation oxide films will allow future OLSMR devices to support electric fields needed for EPM measurement. In addition, it is believed that the large oscillatory background signal observed in the first generation of OLSMR devices can also be attributed to their passivation oxide properties, since breakdown of the oxide in OSMR devices has often been accompanied by a higher sensitivity of the resonance frequency to changes in electric field. Hence these proposed process changes should solve both problems simultaneously. Although larger devices will necessarily suffer from decreased mass sensitivity due to their larger mass, this effect depends only linearly on the height of the channel and will be more than offset by the gain in added mass for larger particles, which depends on the cube of this dimension. For example, the spatial resolution of a mammalian cell with a size similar to the channel height of the OLSMR (15 μm) is expected to be as low as a few tens of nanometers, compared to 2 μm for particles approaching the channel height of the OSMR (3 μm). This, in turn, will reduce the requirements for electric field strength needed to produce a measureable EPM signal. Lower electric fields should increase the longevity of the device, since dielectric breakdown of the OSMR passivation oxide appeared to be dependent on both the magnitude and duration of electric field applied to the channel for the few devices that were tested. Future devices will also be designed with cell trapping structures in order to explore the possibility of monitoring a single cell's EPM as a function of time while varying the medium composition in a controlled manner.

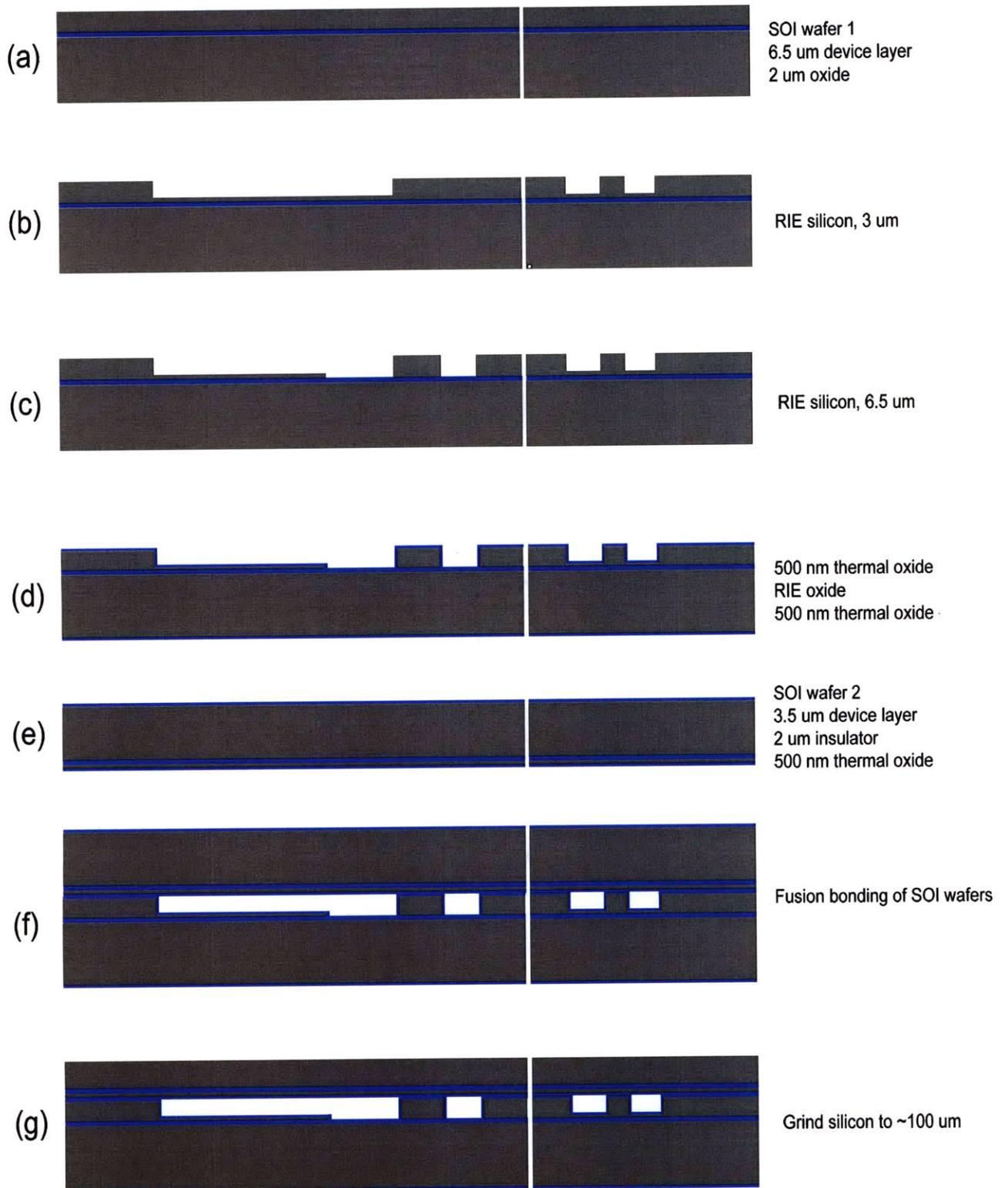
Appendix A.1: Fabrication Processes

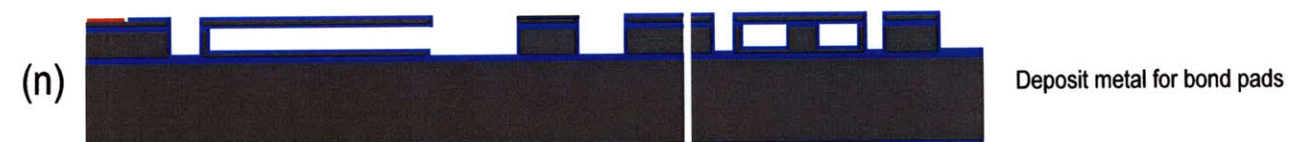
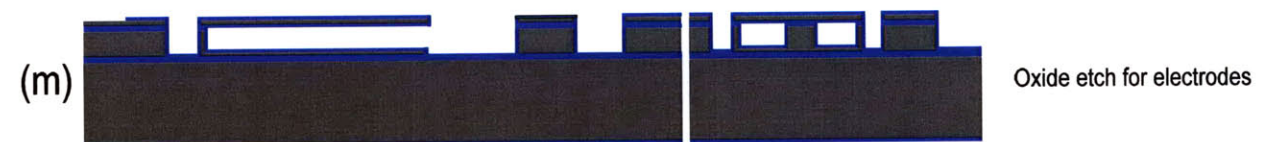
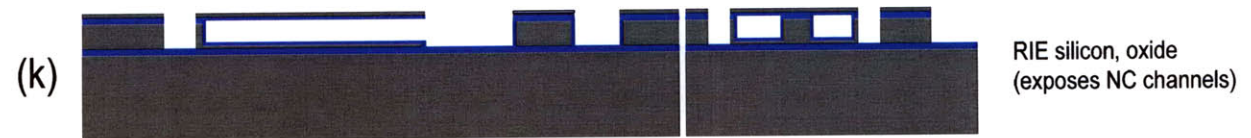
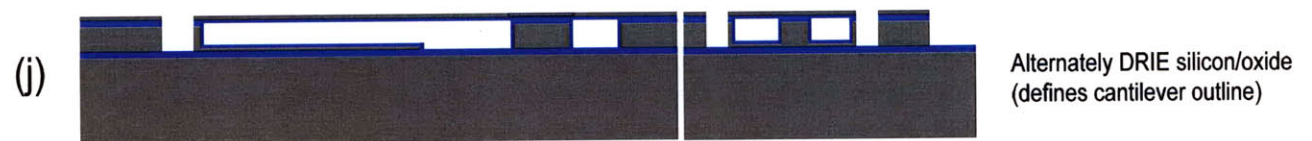
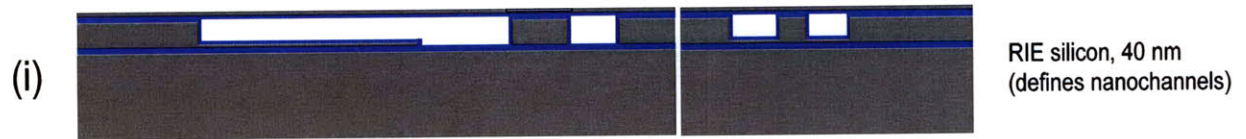
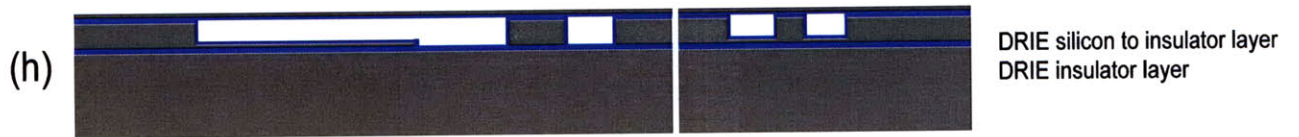
A.1.1 OSMR Process

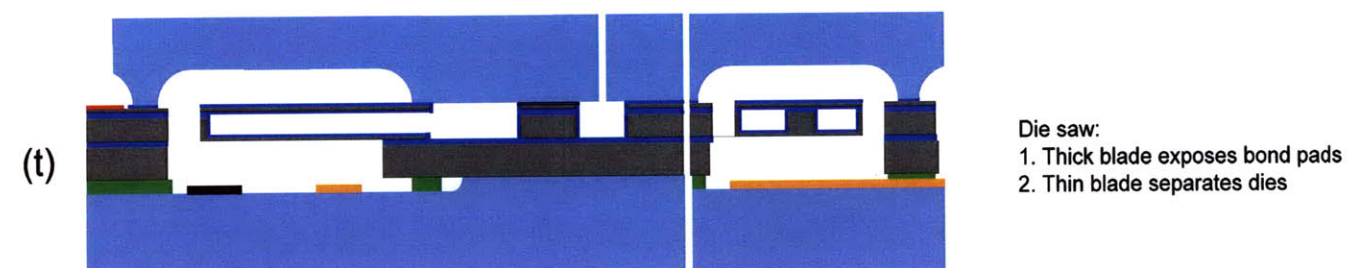
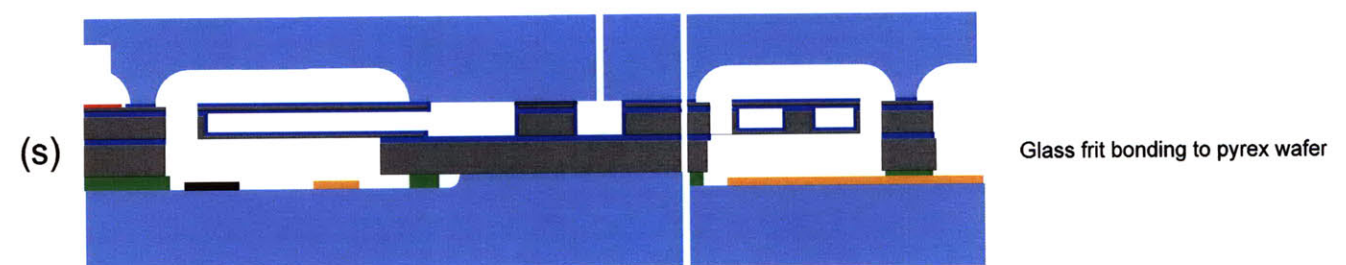
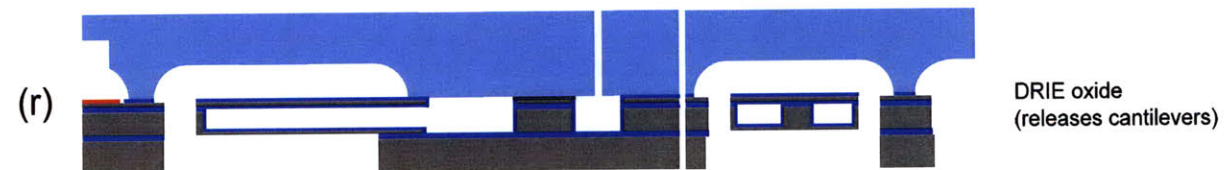
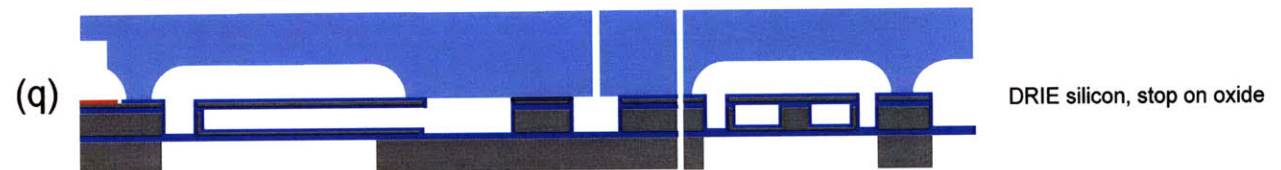
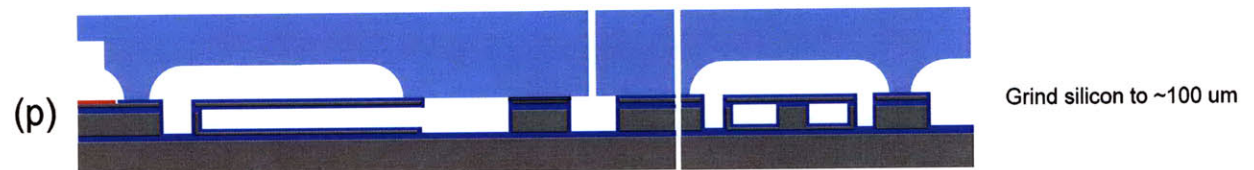
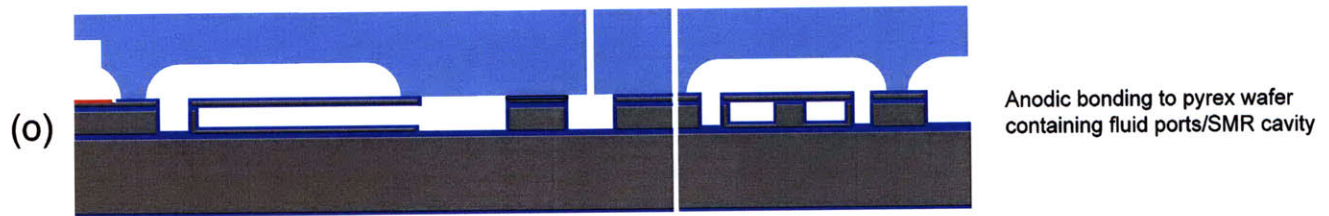




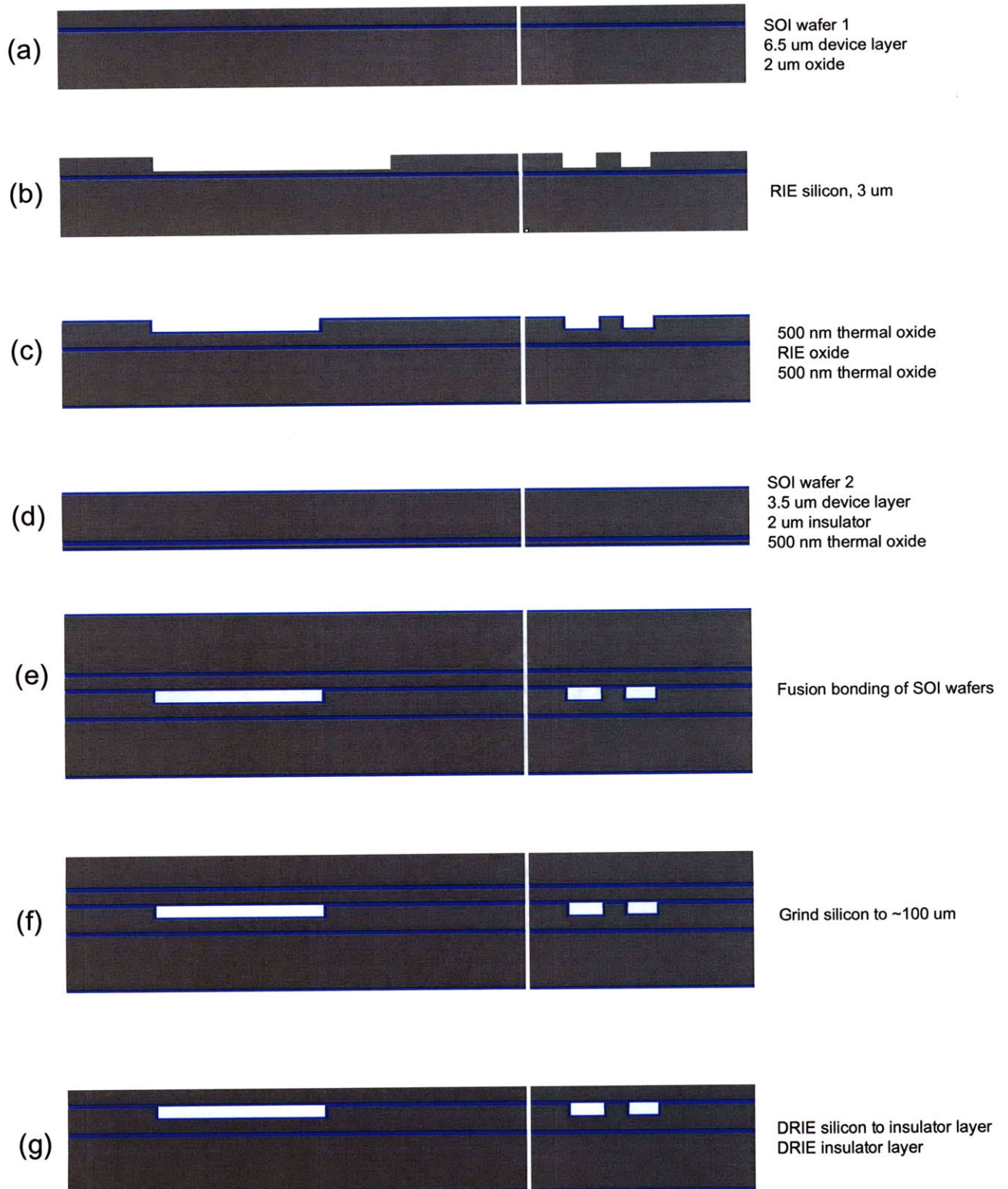
A.1.2 First Generation Integrated Device

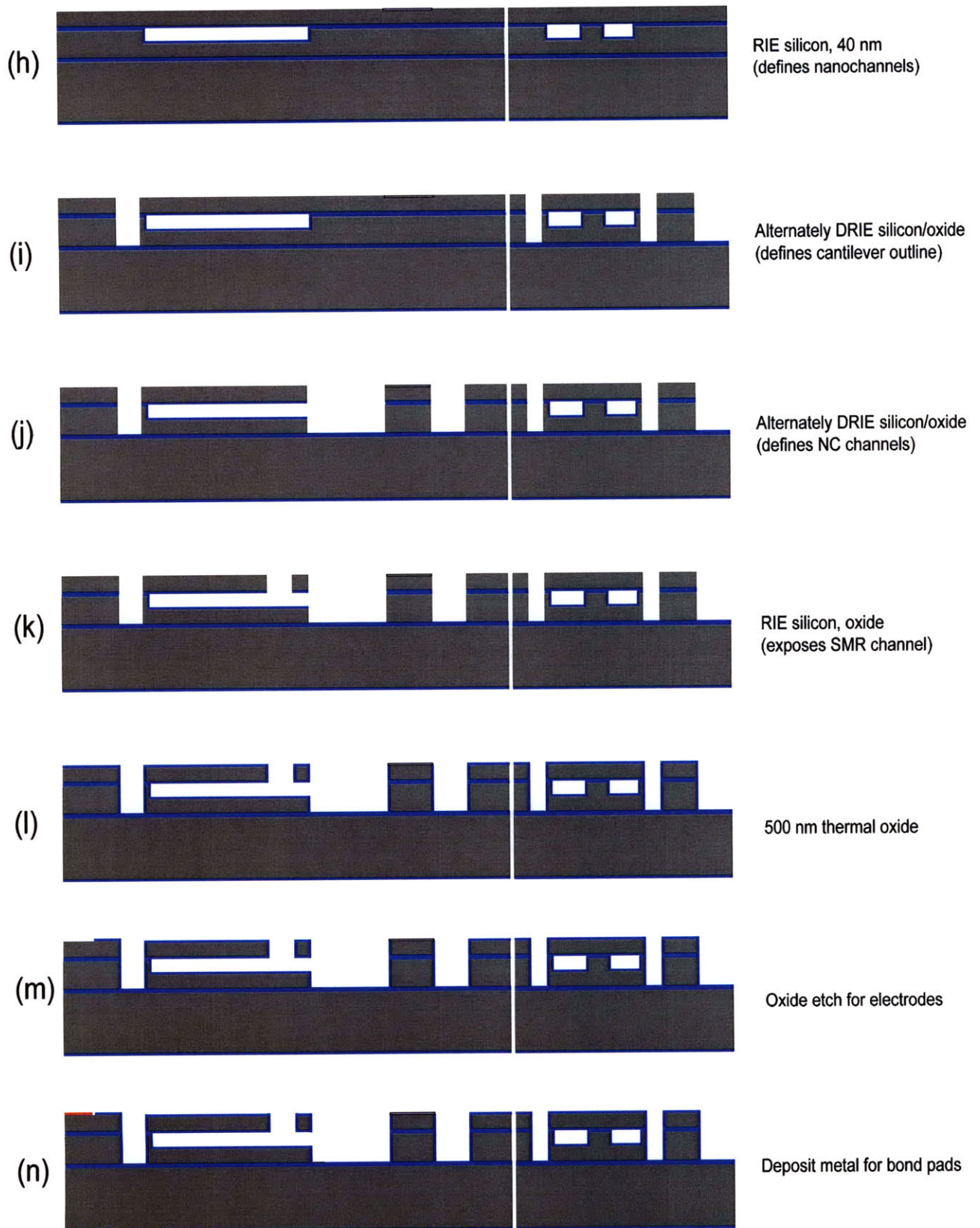


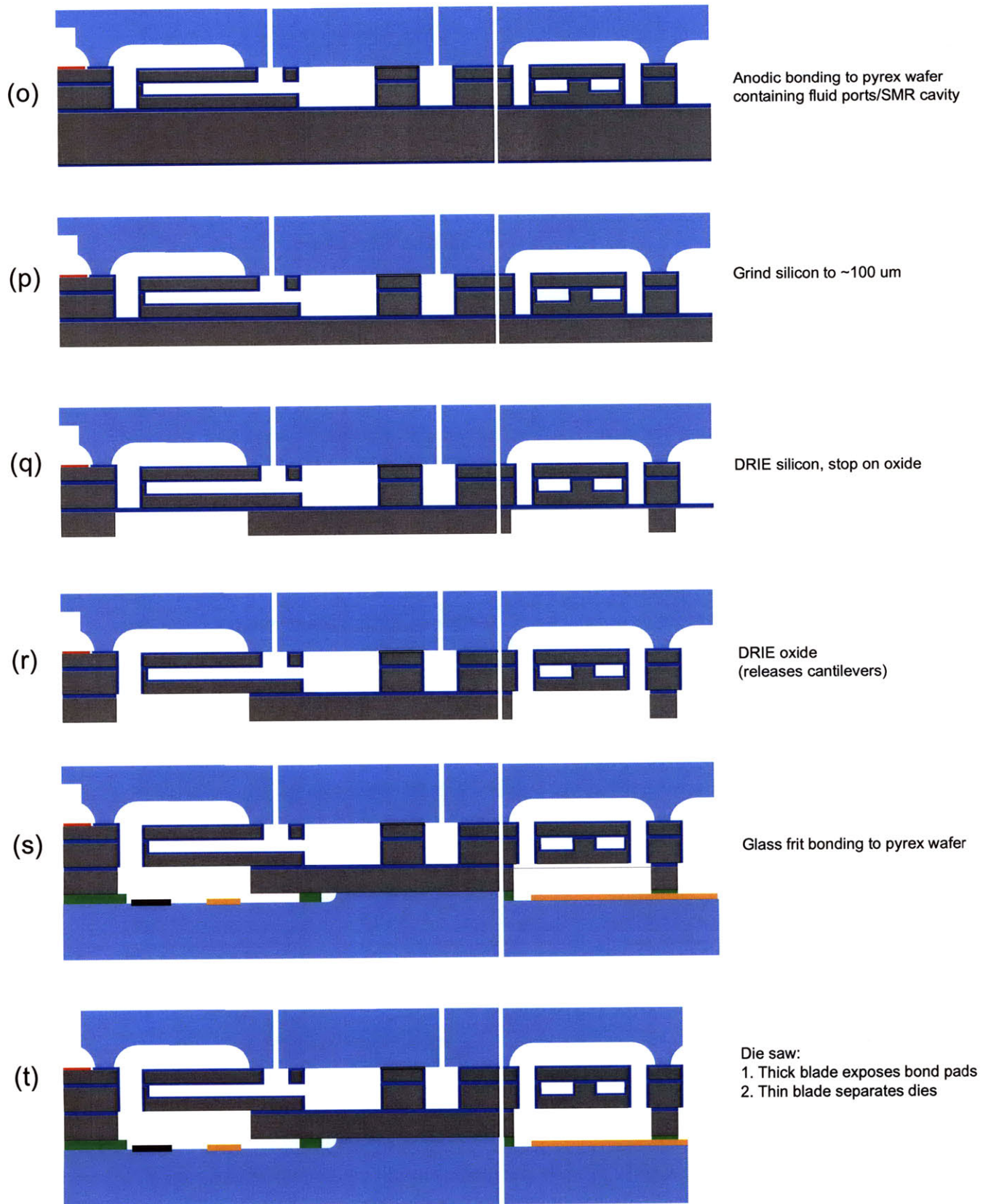




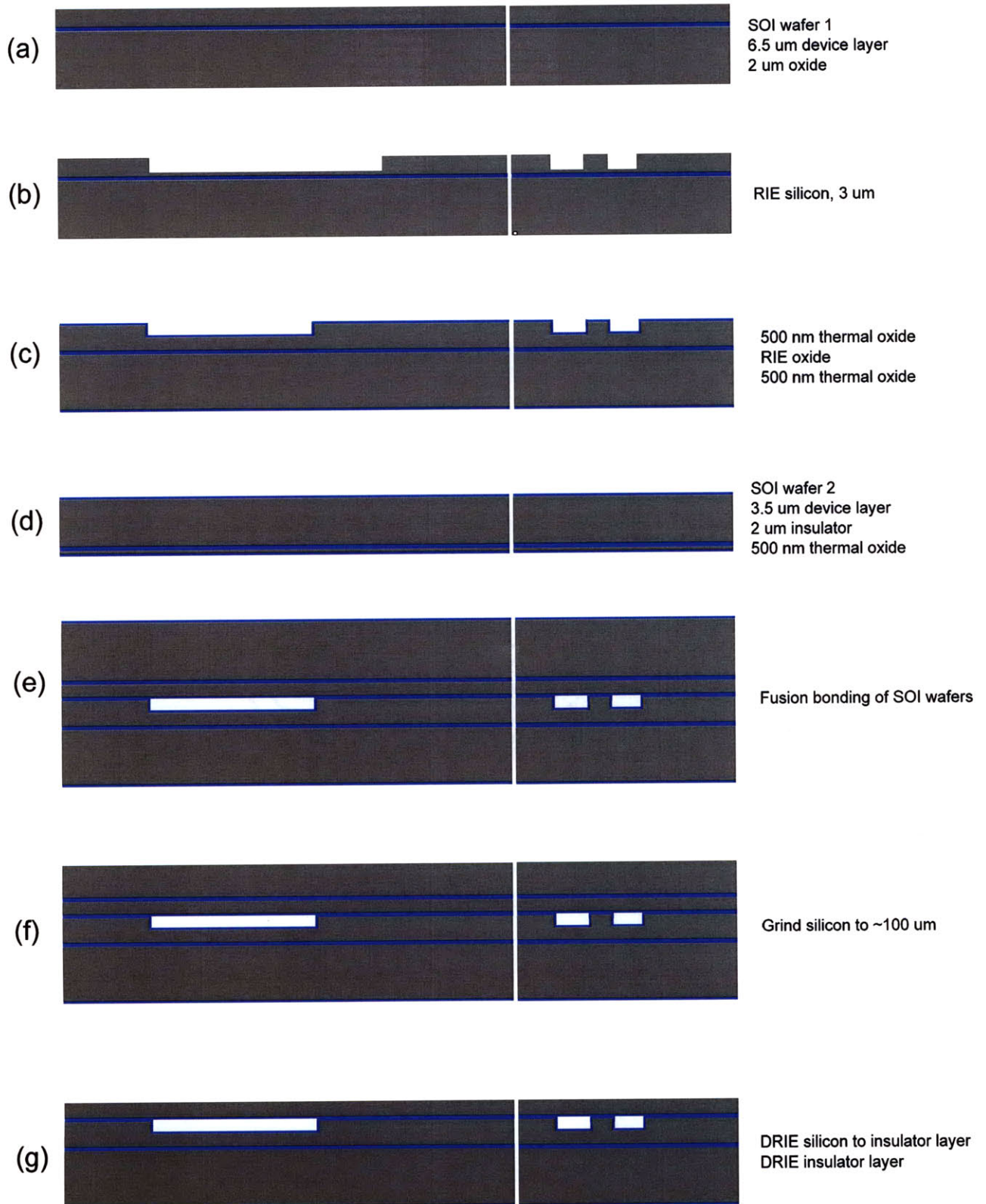
A.1.3 Second Generation Integrated Device

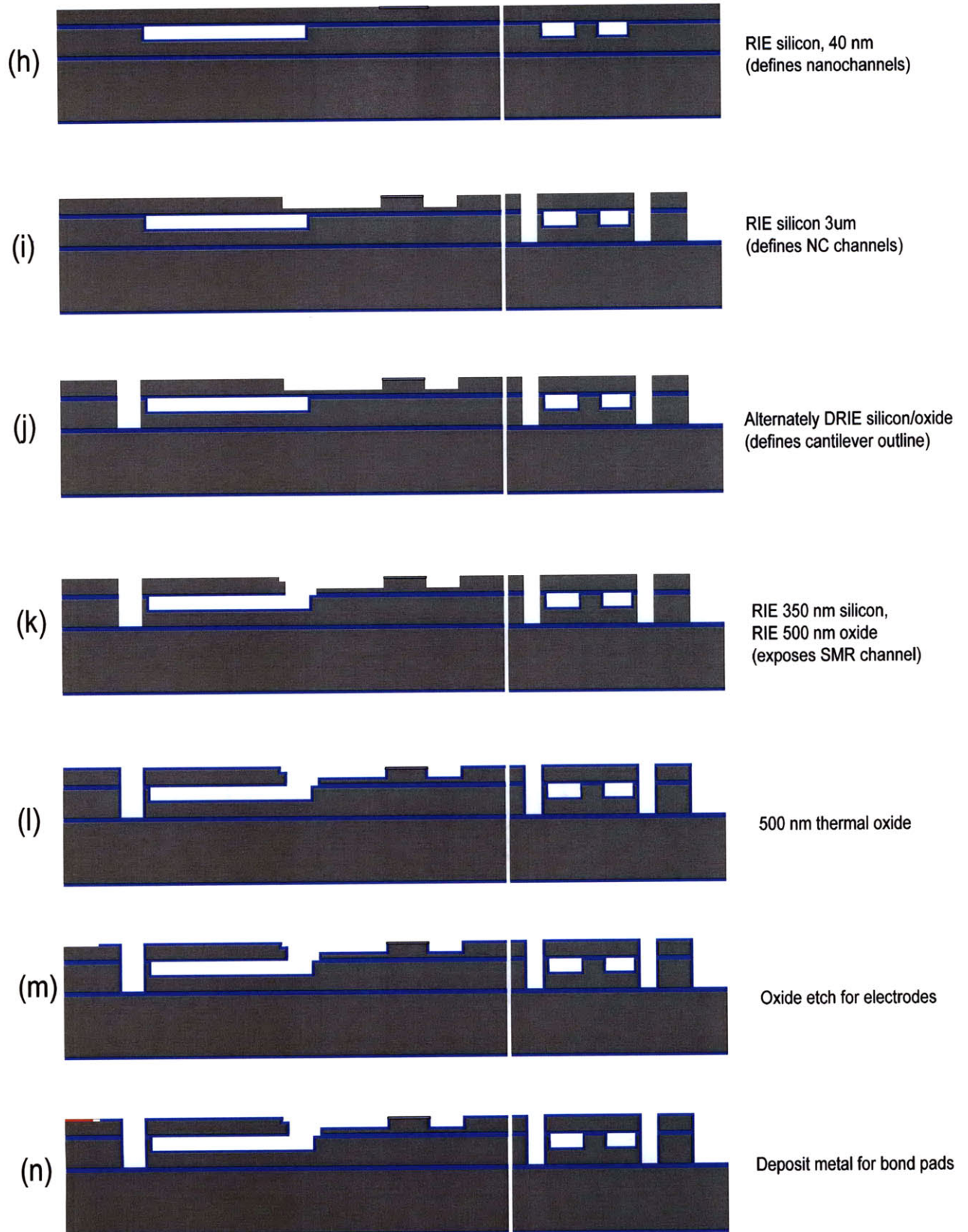


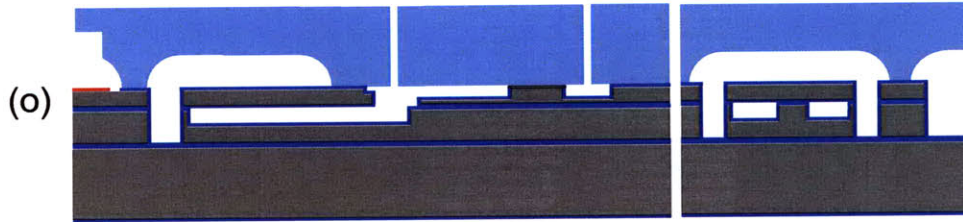




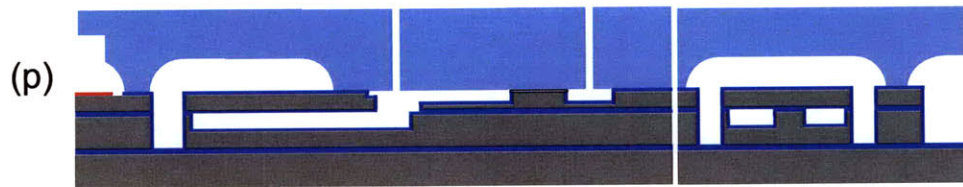
A.1.4 Third Generation Integrated Device



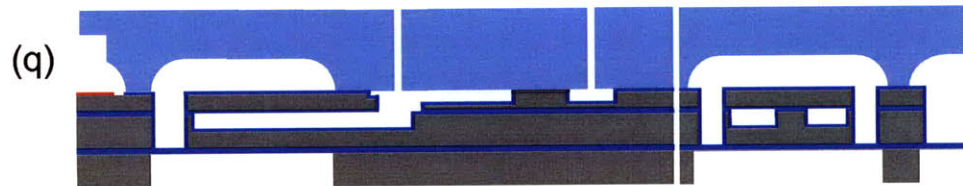




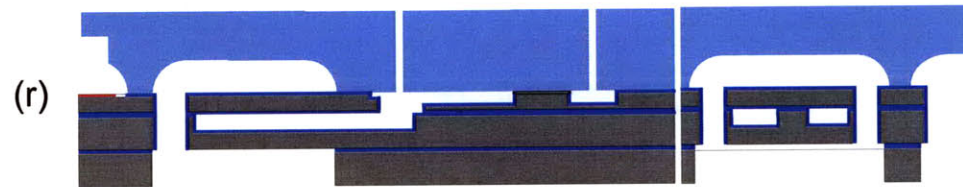
Anodic bonding to pyrex wafer
containing fluid ports/SMR cavity



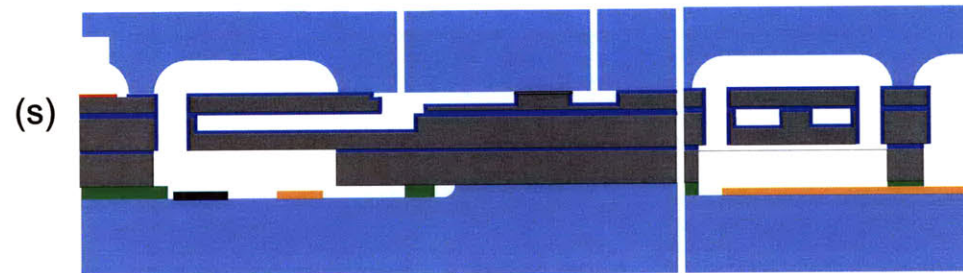
Grind silicon to ~100 um



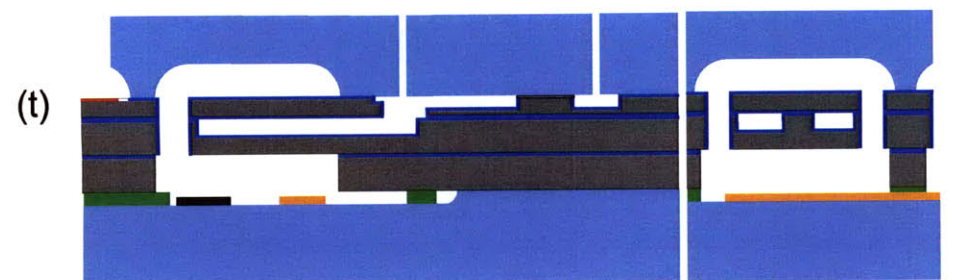
DRIE silicon, stop on oxide



DRIE oxide
(releases cantilevers)

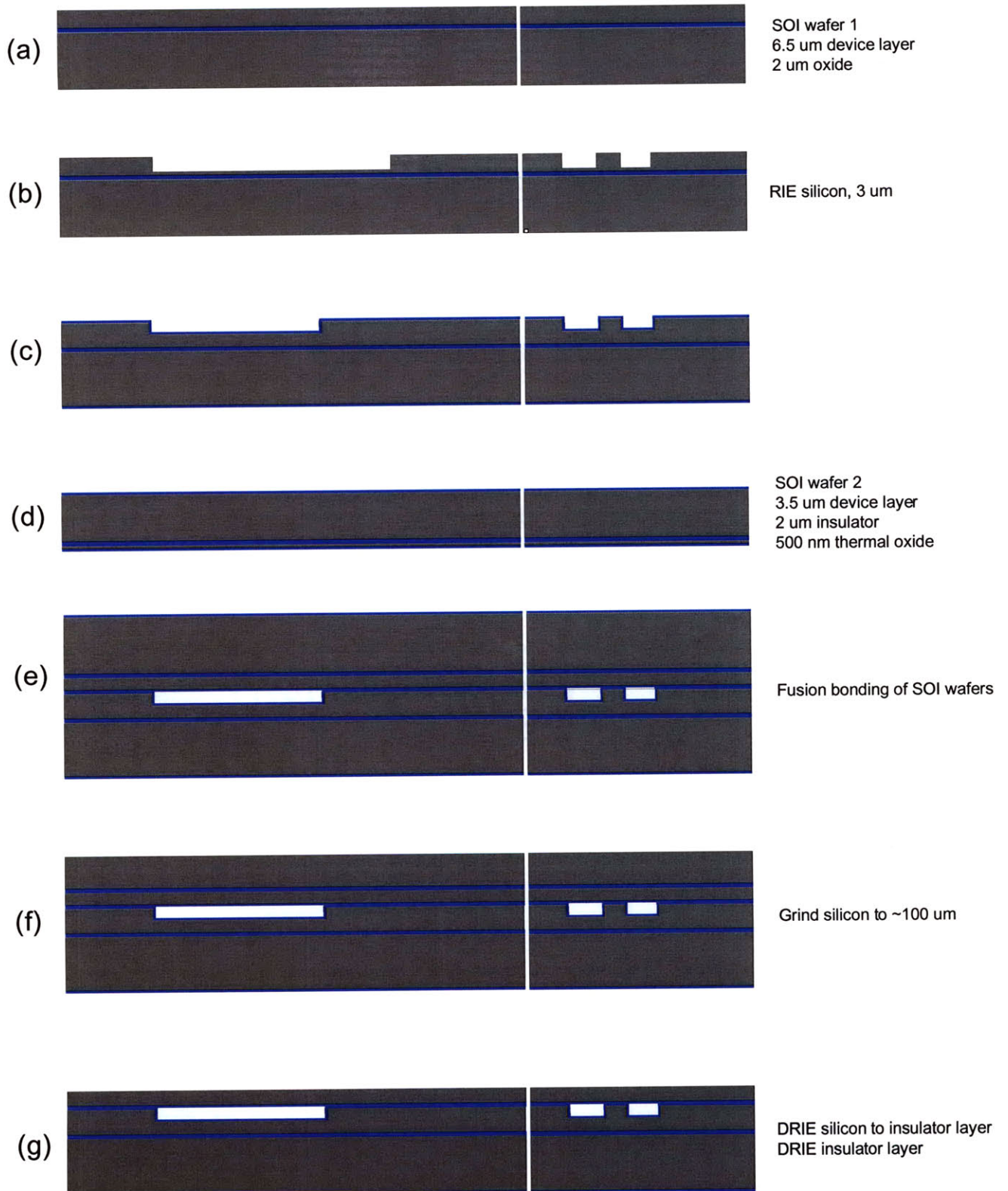


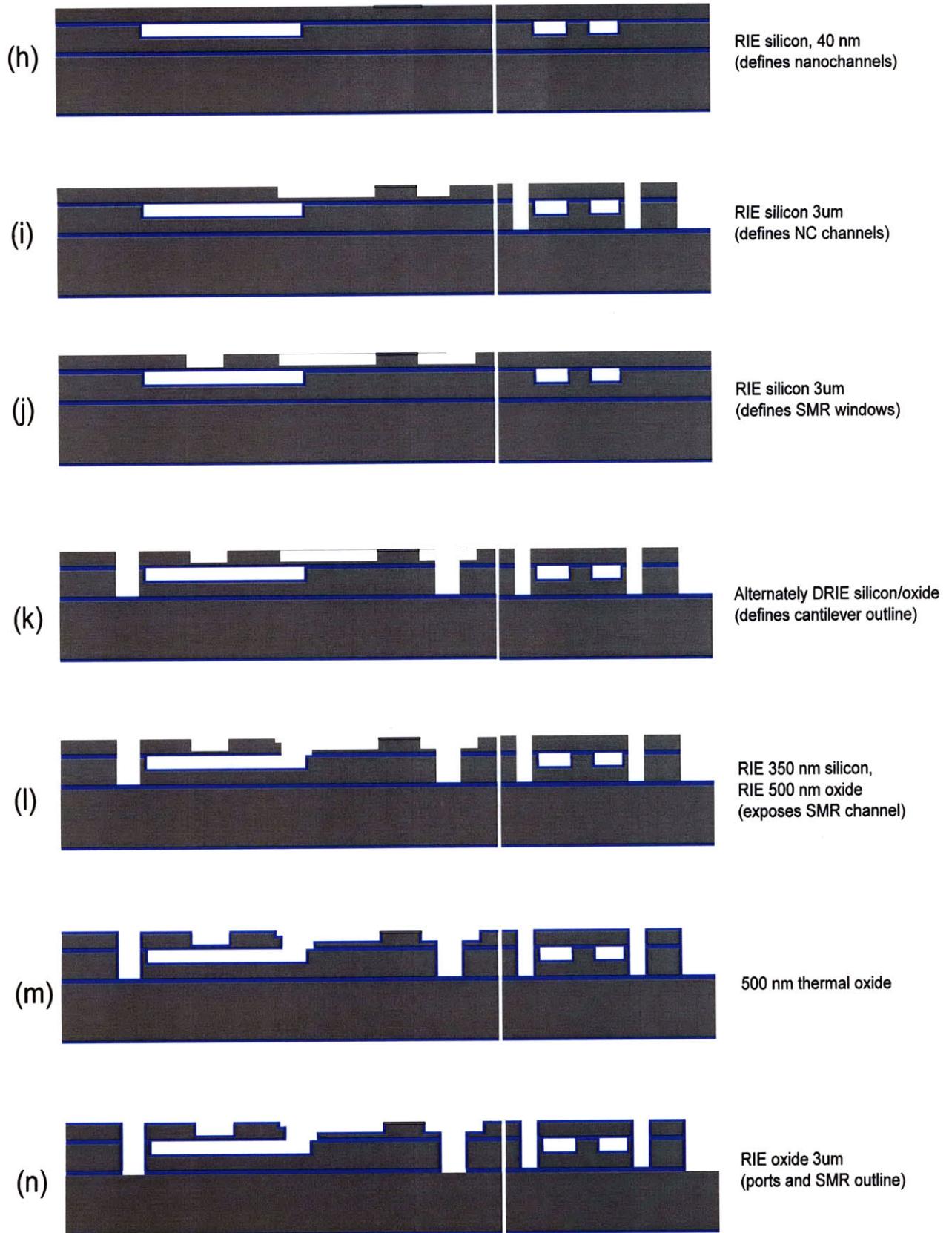
Glass frit bonding to pyrex wafer

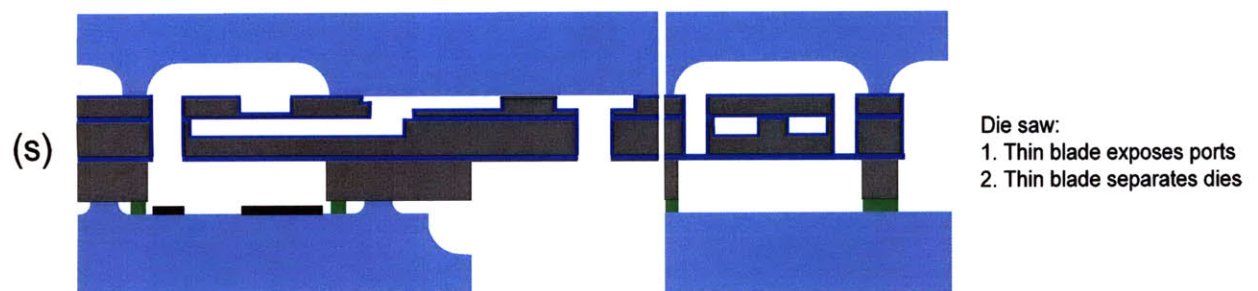
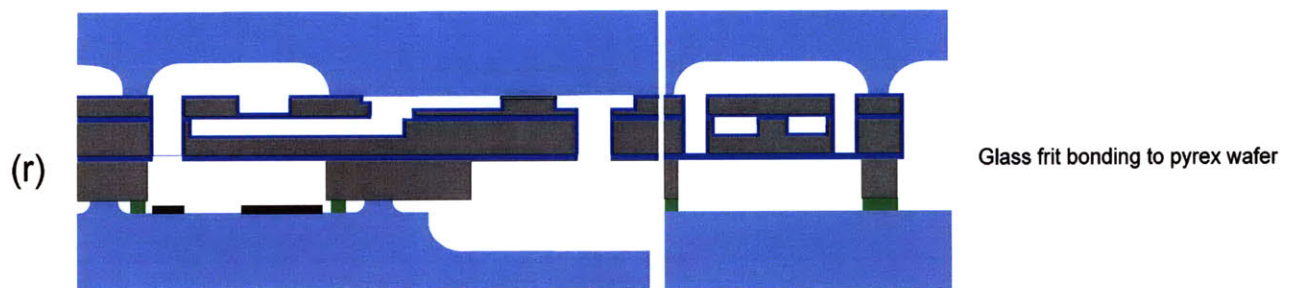
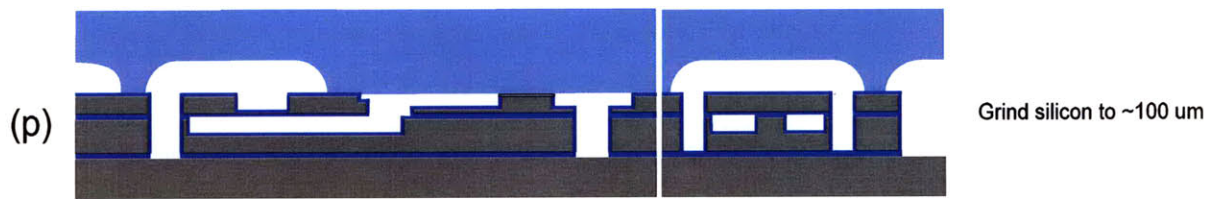
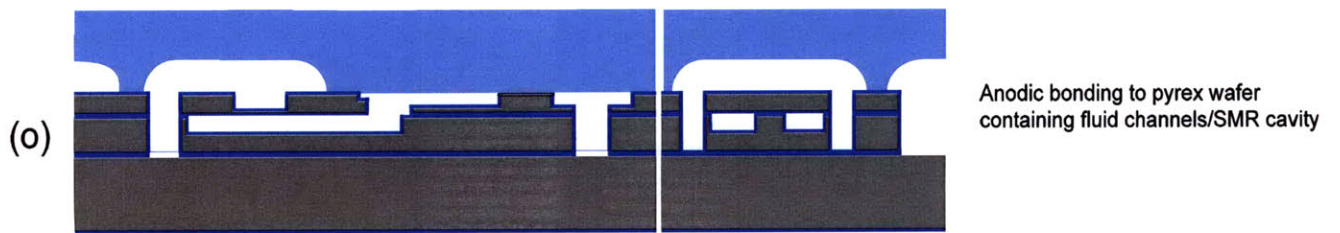


Die saw:
1. Thick blade exposes bond pads
2. Thin blade separates dies

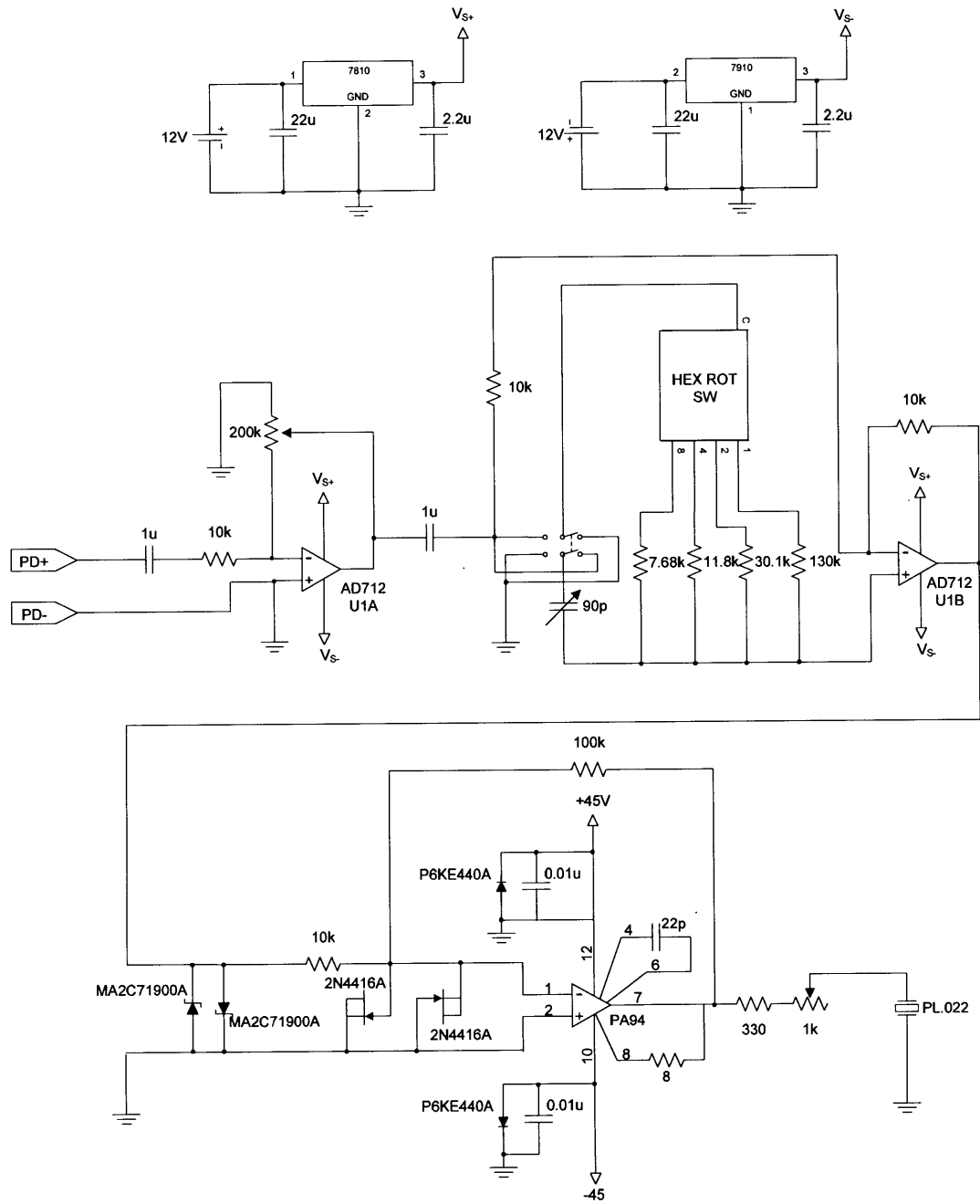
A.1.5 Fourth Generation Integrated Device





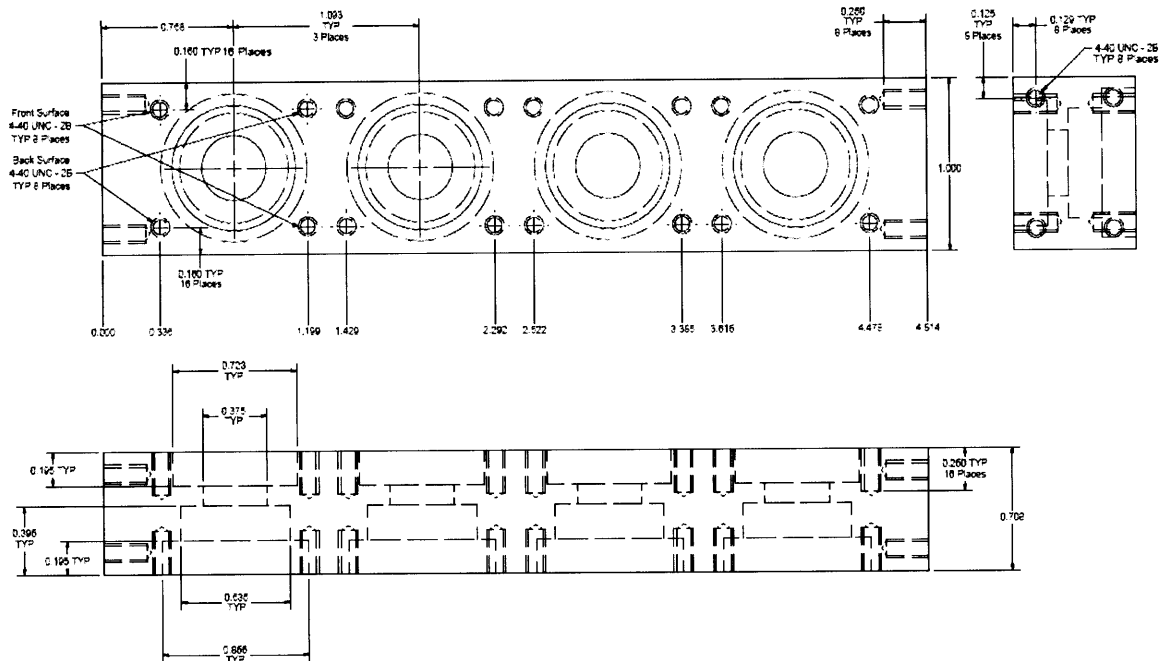


A.2 Circuit Schematics

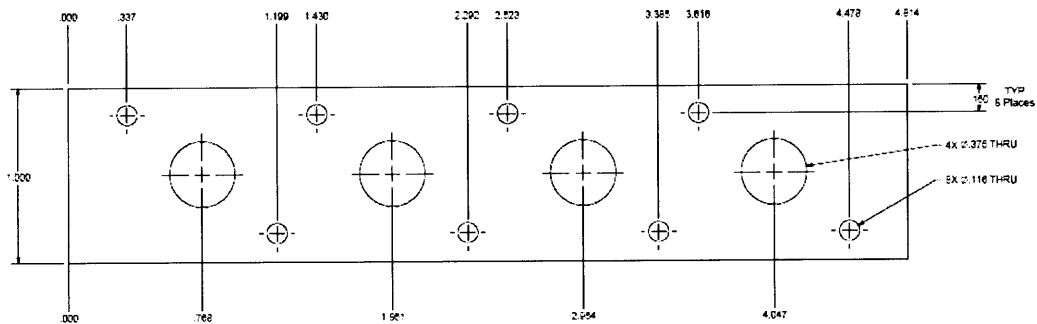


A.3 Fluidic Manifold Drawings

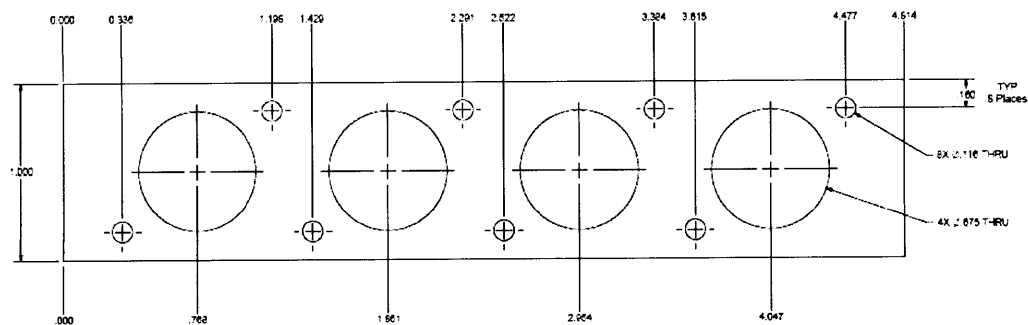
Manifold Body: Acrylic



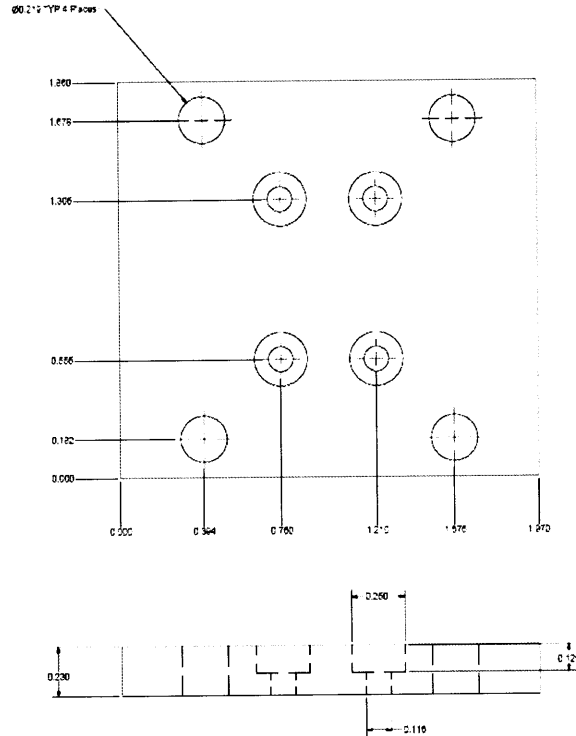
Upper Retaining Sheet: 1/16" Acrylic



Lower Retaining Sheet: 1/16" Acrylic



Adapter Brackets (2): Acrylic



Assembly

- Populate each 0.856" groove with a #208 EPDM o-ring, and add the lower retaining sheet.
- Populate each 0.723" groove with a #206 EPDM o-ring. Using a vise, compress a 0.5" dia. x 0.2" thick PTFE disc into each of the #206 o-rings, and add the upper retaining sheet.
- Mount the adapter brackets to the ends of the manifold body. The opposite side of each bracket mounts directly to a lockable PTFE-lined guide blocks (McMaster P/N 3249K2).

Bibliography

1. Comiskey, B., Albert, J.D., Yoshizawa, H., Jacobson, J., *An electrophoretic ink for all-printed reflective electronic displays*. Nature, 1998. 394: p. 253-255.
2. Howe, A.M., *Some aspects of colloids in photography*. Curr. Opin. Colloid Interface Sci. , 2000. 5: p. 288-300.
3. Malmsten, M., Lindstrom, A., Warnheim, T. , *Electrostatic Effects on Interfacial Film Formation in Emulsion Systems*. J. Colloid Interface Sci., 1996. 179: p. 537-543.
4. Xia, Y., Gates, B., Yin, Y., Lu, Y., *Monodispersed Colloidal Spheres: Old Materials with New Applications*. Advanced Materials, 2000. 12: p. 693-713.
5. Zhao, H., Bhattacharjee, S., Chow, R., Wallace, D., Masliyah, J. H., Xu, Z., *Probing Surface Charge Potentials of Clay Basal Planes and Edges by Direct Force Measurements*. Langmuir, 2008. 24: p. 12899-12910
6. Miller, J.F., Schätzel, K., Vincent, B. J., *The Determination of Very Small Electrophoretic Mobilities in Polar and Nonpolar Colloidal Dispersions Using Phase Analysis Light Scattering*. J. Colloid Interface Sci., 1991. 143: p. 532-554.
7. Ito, T., Sun, L., Bevan, M. A., Crooks, R. M., *Comparison of Nanoparticle Size and Electrophoretic Mobility Measurements Using a Carbon-Nanotube-Based Coulter Counter, Dynamic Light Scattering, Transmission Electron Microscopy, and Phase Analysis Light Scattering*. Langmuir, 2004. 20(16): p. 6940-5.
8. Peng, W.P., Lin, H. C., Chu, M. L., Chang, H. C., Lin, H. H., Yu, A. L., Chen, C. H., *Charge Monitoring Cell Mass Spectrometry*. Anal Chem, 2008. 80(7): p. 2524-30.
9. Bauer, J., *Cell Electrophoresis*. 1994, Boca Raton: CRC Press.
10. Mehrishi, J.N. and J. Bauer, *Electrophoresis of cells and the biological relevance of surface charge*. Electrophoresis, 2002. 23(13): p. 1984-94.

11. Schutt, W., Klinkmann, H., *Cell Electrophoresis*. 1985, Berlin: de Gruyter.
12. Graham, J.M., *Membrane Analysis*. 1997, Oxford: BIOS Scientific Publishers.
13. Papa, S., Tager, J.M., *Biochemistry of Cell Membranes*. 1995, Basel: Birkhaeuser.
14. Latorre, R., P. Labarca, and D. Naranjo, *Surface charge effects on ion conduction in ion channels*. *Methods Enzymol*, 1992. 207: p. 471-501.
15. Simionescu, M. and N. Simionescu, *Endothelial transport of macromolecules: transcytosis and endocytosis. A look from cell biology*. *Cell Biol Rev*, 1991. 25(1): p. 1-78.
16. Bongrand, P., Bell, G.I., *Cell-cell adhesion: parameters and possible mechanisms*, in *Cell Surface Dynamics*, A.S. Perelson, DeLisi, C., Frederik, W.W., Editor. 1984, Marcel Drekker Inc.: New York. p. 459-494.
17. van Oss, C.J., *Interaction forces between biological and other polar entities in water: how many different primary forces are there?* *J. Dispersion Sci. Technol.*, 1991. 12: p. 201-219.
18. Zhang, P.C., A.M. Keleshian, and F. Sachs, *Voltage-induced membrane movement*. *Nature*, 2001. 413(6854): p. 428-32.
19. Bos, R., H.C. van der Mei, and H.J. Busscher, *Physico-chemistry of initial microbial adhesive interactions--its mechanisms and methods for study*. *FEMS Microbiol Rev*, 1999. 23(2): p. 179-230.
20. Mozes, N., et al., *Immobilization of microorganisms by adhesion: Interplay of electrostatic and nonelectrostatic interactions*. *Biotechnol Bioeng*, 1987. 30(3): p. 439-50.
21. Donlan, R.M. and J.W. Costerton, *Biofilms: survival mechanisms of clinically relevant microorganisms*. *Clin Microbiol Rev*, 2002. 15(2): p. 167-93.
22. Gotz, F., *Staphylococcus and biofilms*. *Mol Microbiol*, 2002. 43(6): p. 1367-78.
23. Parsek, M.R. and P.K. Singh, *Bacterial biofilms: an emerging link to disease pathogenesis*. *Annu Rev Microbiol*, 2003. 57: p. 677-701.
24. Ferguson, A.S., et al., *Microbial analysis of soil and groundwater from a gasworks site and comparison with a sequenced biological reactive barrier remediation process*. *J Appl Microbiol*, 2007. 102(5): p. 1227-38.
25. Flemming, H.C., *Biofouling in water systems--cases, causes and countermeasures*. *Appl Microbiol Biotechnol*, 2002. 59(6): p. 629-40.

26. Singh, R., D. Paul, and R.K. Jain, *Biofilms: implications in bioremediation*. Trends Microbiol, 2006. 14(9): p. 389-97.
27. Murugan, A. and M.S. Ramasamy, *Biofouling deterrent activity of the natural product from ascidian, Distaplia nathensis [Chordata]*. Indian Journal of Marine Sciences, 2003. 32(2): p. 162-164.
28. Raichur, A.M., Misra, M., Bukka, K., Smith, R.W., *Flocculation and flotation of coal by adhesion of hydrophobic Mycobacterium phlei*. Colloids and Surfaces B: Biointerfaces, 1996. 8: p. 13-24.
29. Wong, A.C., *Biofilms in food processing environments*. J Dairy Sci, 1998. 81(10): p. 2765-70.
30. Hannig, K., *New aspects in preparative and analytical continuous free-flow cell electrophoresis*. Electrophoresis, 1982. 3: p. 235.
31. Hansen, E., Hannig, K., *Electrophoretic separation of lymphoid cells*. Methods Enzymol., 1984. 108: p. 180.
32. Hansen, E., *Preparative free-flow electrophoresis of lymphoid cells: a review*, in *Cell Electrophoresis*, W. Schutt, Kinkmann, H., Editor. 1985, de Gruyter: Berlin. p. 287.
33. Hymer, W.C., Barlow, G.H., Blaisdell, S.J., Cleveland, C., Farrington, M.A., Feldmeier, M., Grindeland, R., Hatfield, J.M., Lanham, J.W., Lewis, M.L., Morrison, D.R., Olack, B.J., Richman, D.W., Rose, J., Scharp, D.W., Snyder, R.S., Swanson, C.A., Todd, P., Wilfinger, W., *Continuous free-flow electrophoretic separation of proteins and cells from mammalian tissues*. Cell Biophys., 1987. 10: p. 61.
34. Lewis, M.L., Barlow, G.H., Morrison, D.R., Nachtwey, D.S., Fessler, D.L., *Plasminogen activator production in human kidney cells separated by continuous flow electrophoresis*, in *Progress in Fibrinolysis*, J.F. Davidson, Bachmann, F., Bouvier, C.A., Kruithof, E.K.O., Editor. 1983, Churchill Livingstone: Edinburgh. p. 143.
35. Morrison, D.R., et al., *Electrophoretic separation of kidney and pituitary cells on STS-8*. Adv Space Res, 1984. 4(5): p. 67-76.
36. Morrison, D.R., et al., *Properties of electrophoretic fractions of human embryonic kidney cells separated on Space Shuttle flight STS-8*. Adv Space Res, 1984. 4(5): p. 77-79.
37. Todd, P., Plank, L.D., Kunze, M.E., Lewis, M.L., Morrison, D.R., Barlow, G.H., Lanham, J.W., Cleveland, C., *Electrophoretic separation and analysis of living cells from solid tissues by several methods. Human embryonic kidney cells as a model*. J. Chromatogr., 1986. 364: p. 11-24.

38. Akagi, T., Suzuki, M., Ichiki, T., *Application of On-Chip Electrophoresis of Cell to Evaluation of Cell Cycle Stages of HL-60 Cells*. Japanese Journal of Applied Physics, 2006. 45(41): p. L1106-L1109.
39. Brent, T.P., Forrester, J.A., *Changes in surface charge of HeLa cells during the cell cycle*. Nature, 1967. 215: p. 92-93.
40. Mayhew, E., O'Grady, E.A., *Electrophoretic mobilities of tissue culture cells in exponential and parasynchronous growth*. Nature, 1965. 207: p. 86-87.
41. Battler, A., Leor, J., *Stem cell and gene-based therapy: frontiers and in regenerative medicine*. 2007, Berlin: Springer.
42. Templeton, N., *Gene and cell therapy: therapeutic mechanisms and strategies*. 2003, New York: Marcel Dekker.
43. van der Mei, H.C. and H.J. Busscher, *Electrophoretic mobility distributions of single-strain microbial populations*. Appl Environ Microbiol, 2001. 67(2): p. 491-4.
44. Goetz, P.J., *System 3000 automated electrokinetics analyzer for biomedical applications*, in *Cell Electrophoresis*, W. Schutt, Kinkmann, H., Editor. 1985, de Gruyter: Berlin. p. 41-53.
45. Noordmans, J., Kempen, J., Busscher, H.J., *Automated Image Analysis to Determine Zeta Potential Distributions in Particulate Microelectrophoresis*. J. Colloid Interface Sci., 1992. 156: p. 394-399.
46. Moyer, L.S., *A Suggested Standard Method for the Investigation of Electrophoresis*. J Bacteriol, 1936. 31(5): p. 531-46.
47. Machin, M., et al., *Single particle tracking across sequences of microscopical images: Application to platelet adhesion under flow*. Annals of Biomedical Engineering, 2006. 34(5): p. 833-846.
48. Wit, P.J., Noordmans, J., Busscher, H.J., *Tracking of colloidal particles using microscopic image sequence analysis Application to particulate microelectrophoresis and particle deposition*. Colloids Surf. A, 1997. 125: p. 85-92.
49. Slivinsky, G.G., *Simultaneous two-parameter measurements of the electrophoretic features of cell subpopulations and their different sedimentation characteristics*, in *Cell Electrophoresis*, J. Bauer, Editor. 1994, CRC Press: Boca Raton. p. 199-217.

50. Burg, T.P., Mirza, A.R., Milovic, N., Tsau, C.H., Popescu, G.A., Foster, J.S., Manalis, S.R., *Vacuum-Packaged Suspended Microchannel Resonant Mass Sensor for Biomolecular Detection*. IEEE Journal of Microelectromechanical Systems, 2006. 15(6): p. 1466 - 1476.
51. Cleland, A.N., *Foundations of Nanomechanics*. 2003, Springer-Verlag: Berlin. p. 233-239.
52. Dohn, S., et al., *Mass and position determination of attached particles on cantilever based mass sensors*. Rev Sci Instrum, 2007. 78(10): p. 103303.
53. von Smoluchowski, M., *Handbuch der Elektrizität und des Magnetismus*, ed. L. Greatz. Vol. 2. 1921, Leipzig: Barth. 366.
54. Hunter, R.J., *Zeta Potential in Colloid Science: Principles and Applications*. 1981, Academic Press Inc.: New York. p. 49.
55. Godin, M., Bryan, A.K., Burg, T. P., Babcock, K., Manalis, S.R. , *Measuring the mass, density and size of particles and cells using a suspended microchannel resonator*. Appl Phys Lett, 2007. 91(12): p. 123121.
56. Sharma, S., et al., *Silicon-on-insulator microfluidic device with monolithic sensor integration for mu TAS applications*. Journal of Microelectromechanical Systems, 2006. 15(2): p. 308-313.
57. Hall-Stoodley, L., J.W. Costerton, and P. Stoodley, *Bacterial biofilms: from the natural environment to infectious diseases*. Nat Rev Microbiol, 2004. 2(2): p. 95-108.
58. Ohshima, H., *Electrophoretic Mobility of Soft Particles*. Journal of Colloid and Interface Science, 1994. 163(2): p. 474-483.
59. Ohshima, H. and T. Kondo, *Approximate Analytic-Expression for the Electrophoretic Mobility of Colloidal Particles with Surface-Charge Layers*. Journal of Colloid and Interface Science, 1989. 130(1): p. 281-282.
60. de Kerchove, A.J. and M. Elimelech, *Relevance of electrokinetic theory for "soft" particles to bacterial cells: implications for bacterial adhesion*. Langmuir, 2005. 21(14): p. 6462-72.
61. Duval, K.F.L. and H. Ohshima, *Electrophoresis of diffuse soft particles*. Langmuir, 2006. 22(8): p. 3533-3546.
62. Hoffmann, J.A., *Innate Immunity of Insects*. Current Opinion in Immunology, 1995. 7(1): p. 4-10.

63. Holak, T.A., et al., *The Solution Conformation of the Antibacterial Peptide Cecropin-a - a Nuclear Magnetic-Resonance and Dynamical Simulated Annealing Study*. Biochemistry, 1988. 27(20): p. 7620-7629.
64. Steiner, H., *Secondary Structure of the Cecropins - Antibacterial Peptides from the Moth Hyalophora-Cecropia*. Febs Letters, 1982. 137(2): p. 283-287.
65. Steiner, H., et al., *Sequence and Specificity of 2 Anti-Bacterial Proteins Involved in Insect Immunity*. Nature, 1981. 292(5820): p. 246-248.
66. Gazit, E., et al., *Interaction of the Mammalian Antibacterial Peptide Cecropin PI with Phospholipid-Vesicles*. Biochemistry, 1995. 34(36): p. 11479-11488.
67. Steiner, H., D. Andreu, and R.B. Merrifield, *Binding and Action of Cecropin and Cecropin Analogs - Antibacterial Peptides from Insects*. Biochimica Et Biophysica Acta, 1988. 939(2): p. 260-266.
68. Christensen, B., et al., *Channel-Forming Properties of Cecropins and Related Model Compounds Incorporated into Planar Lipid-Membranes*. Proceedings of the National Academy of Sciences of the United States of America, 1988. 85(14): p. 5072-5076.
69. Mchaourab, H.S., J.S. Hyde, and J.B. Feix, *Binding and State of Aggregation of Spin-Labeled Cecropin Ad in Phospholipid-Bilayers - Effects of Surface-Charge and Fatty Acyl-Chain Length*. Biochemistry, 1994. 33(21): p. 6691-6699.
70. Silvestro, L., et al., *The concentration-dependent membrane activity of cecropin A*. Biochemistry, 1997. 36(38): p. 11452-11460.
71. Arcidiacono, S., et al., *Membrane permeability and antimicrobial kinetics of cecropin PI against Escherichia coli*. Journal of Peptide Science, 2009. 15(6): p. 398-403.
72. Eboigbodin, K.E., et al., *Bacterial quorum sensing and cell surface electrokinetic properties*. Applied Microbiology and Biotechnology, 2006. 73(3): p. 669-675.
73. Soni, K.A., et al., *Zeta potential of selected bacteria in drinking water when dead, starved, or exposed to minimal and rich culture media*. Current Microbiology, 2008. 56(1): p. 93-97.
74. Tazehkand, S.S., et al., *Cell Preparation Methods Influence Escherichia Coli D21g Surface Chemistry and Transport in Saturated Sand*. Journal of Environmental Quality, 2008. 37(6): p. 2108-2115.
75. Xiao, L., X.L. Qu, and D.Q. Zhu, *Biosorption of nonpolar hydrophobic organic compounds to Escherichia coli facilitated by metal and proton surface binding*. Environmental Science & Technology, 2007. 41(8): p. 2750-2755.

76. Georganopoulou, D.G., et al., *Nanoparticle-based detection in cerebral spinal fluid of a soluble pathogenic biomarker for Alzheimer's disease*. Proc Natl Acad Sci U S A, 2005. 102(7): p. 2273-6.
77. Mairal, T., et al., *Aptamers: molecular tools for analytical applications*. Anal Bioanal Chem, 2008. 390(4): p. 989-1007.
78. Thaxton, C.S., et al., *Nanoparticle-based bio-barcode assay redefines "undetectable" PSA and biochemical recurrence after radical prostatectomy*. Proc Natl Acad Sci U S A, 2009. 106(44): p. 18437-42.
79. Wang, Y.C. and J.Y. Han, *Pre-binding dynamic range and sensitivity enhancement for immuno-sensors using nanofluidic preconcentrator*. Lab on a Chip, 2008. 8(3): p. 392-394.
80. Wang, Y.C., A.L. Stevens, and J.Y. Han, *Million-fold preconcentration of proteins and peptides by nanofluidic filter*. Analytical Chemistry, 2005. 77(14): p. 4293-4299.
81. Probstein, R.F., *Physicochemical Hydrodynamics: An Introduction*. 1994: Wiley-Interscience.
82. Dukhin, S.S., *Electrokinetic Phenomena Of The 2nd Kind And Their Applications*. Advances in Colloid and Interface Science, 1991. 35: p. 173-196.
83. Mishchuk, N.A. and P.V. Takhistov, *Electroosmosis Of The 2nd Kind*. Colloids and Surfaces a-Physicochemical and Engineering Aspects, 1995. 95(2-3): p. 119-131.
84. Kim, S.J., L.D. Li, and J. Han, *Amplified Electrokinetic Response by Concentration Polarization near Nanofluidic Channel*. Langmuir, 2009. 25(13): p. 7759-7765.
85. Kim, S.J., et al., *Concentration polarization and nonlinear electrokinetic flow near a nanofluidic channel*. Physical Review Letters, 2007. 99(4): p. 044501-1.
86. Leinweber, F.C. and U. Tallarek, *Nonequilibrium electrokinetic effects in beds of ion-permselective particles*. Langmuir, 2004. 20(26): p. 11637-48.
87. Burgi, D.S. and R.L. Chien, *Optimization in Sample Stacking for High-performance Capillary Electrophoresis*. Analytical Chemistry, 1991. 63(18): p. 2042-2047.
88. Chien, R.L. and D.S. Burgi, *Sample Stacking Of An Extremely Large Injection Volume In High-Performance Capillary Electrophoresis*. Analytical Chemistry, 1992. 64(9): p. 1046-1050.

89. Lichtenberg, J., E. Verpoorte, and N.F. de Rooij, Sample preconcentration by field amplification stacking for microchip-based capillary electrophoresis. *Electrophoresis*, 2001. 22(2): p. 258-271.
90. Zhang, C.X. and W. Thormann, Head-column field-amplified sample stacking in binary system capillary electrophoresis: A robust approach providing over 1000-fold sensitivity enhancement. *Analytical Chemistry*, 1996. 68(15): p. 2523-2532.
91. Gebauer, P. and P. Bocek, Recent progress in capillary isotachopheresis. *Electrophoresis*, 2002. 23(22-23): p. 3858-3864.
92. Molina, M. and M. Silva, Micellar electrokinetic chromatography: Current developments and future. *Electrophoresis*, 2002. 23(22-23): p. 3907-3921.
93. Quirino, J.P. and S. Terabe, Exceeding 5000-fold concentration of dilute analytes in micellar electrokinetic chromatography. *Science*, 1998. 282(5388): p. 465-468.
94. Quirino, J.P. and S. Terabe, Approaching a million-fold sensitivity increase in capillary electrophoresis with direct ultraviolet detection: Cation-selective exhaustive injection and sweeping. *Analytical Chemistry*, 2000. 72(5): p. 1023-1030.
95. Astorga-Wells, J., T. Bergman, and H. Jornvall, Multistep microreactions with proteins using electrocapture technology. *Analytical Chemistry*, 2004. 76(9): p. 2425-2429.
96. Astorga-Wells, J. and H. Swerdlow, Fluidic preconcentrator device for capillary electrophoresis of proteins. *Analytical Chemistry*, 2003. 75(19): p. 5207-5212.
97. Wang, Q.G., B.F. Yue, and M.L. Lee. Mobility-based selective on-line preconcentration of proteins in capillary electrophoresis by controlling electroosmotic flow. in 5th International Symposium on Advances in Extraction Technologies. 2003. St Pete Beach, Florida.
98. Broyles, B.S., S.C. Jacobson, and J.M. Ramsey, Sample filtration, concentration, and separation integrated on microfluidic devices. *Analytical Chemistry*, 2003. 75(11): p. 2761-2767.
99. Huber, D.L., et al., Programmed adsorption and release of proteins in a microfluidic device. *Science*, 2003. 301(5631): p. 352-354.
100. Ro, K.W., et al. Capillary electrochromatography and preconcentration of neutral compounds on poly(dimethylsiloxane) microchips. in 4th Asian-Pacific International Symposium on Microscale Separations and Analysis (ACPE 2002). 2002. Shanghai, Peoples R China.

101. Yu, C., et al., Monolithic porous polymer for on-chip solid-phase extraction and preconcentration prepared by photoinitiated in situ polymerization within a microfluidic device. *Analytical Chemistry*, 2001. 73(21): p. 5088-5096.
102. Khandurina, J., et al., Microfabricated porous membrane structure for sample concentration and electrophoretic analysis. *Analytical Chemistry*, 1999. 71(9): p. 1815-1819.
103. Song, S., A.K. Singh, and B.J. Kirby, Electrophoretic concentration of proteins at laser-patterned nanoporous membranes in microchips. *Analytical Chemistry*, 2004. 76(15): p. 4589-4592.